This is to certify that the
thesis entitled

ORIGIN AND EVOLUTION OF THE NICARAGUAN SILICIC ASH-FLOW SHEETS

presented by

ELA LITA ESTRADA VIRAY

has been accepted towards fulfillment
of the requirements for the

M.S. degree in GEOLOGY

Thomas A Vogel
Major Professor's Signature

7-28-03
Date

ORIGIN AND EVOLUTION OF THE NICARAGUAN SILICIC ASH-FLOW SHEETS

By

Ela Lita Estrada Viray

A THESIS

Submitted to
Michigan State University
in partial fulfillment of the requirements
for the degree of

MASTERS OF SCIENCE

Department of Geological Sciences

2003

ABSTRACT

ORIGIN AND EVOLUTION OF THE NICARAGUAN SILICIC ASH-FLOW SHEET

By

Ela Lita Estrada Viray

Abundant silicic ash-flow sheets occur in Nicaragua yet little is known about their geochemistry, volume, and age. Their origin is a matter of considerable interest because the generation of silicic magma is generally attributed to the assimilation and/or melting of an underlying continental crust. However, no continental crust occurs in this area. Two models on the generation of these ignimbrites are evaluated: (1) fractional crystallization of basalt or andesitic melt, and (2) partial melting of previously emplaced arc-related igneous rocks. Chemical and mineralogical variations within and among the seven recognized silicic ash-flow sheets cannot be explained by fractional crystallization alone but rather by partial melting of previously emplaced arc-related igneous rock. This arc-related igneous rock was partially melted by the injection of new mafic magma from the metasomatized mantle wedge. Continued production and ascent of both the silicic and mafic magmas into the magma chamber allowed mingling between the two magmas, and before even reaching compositional and thermal equilibrium, were erupted as ash-flow sheets with distinct chemical variations. REE patterns of the silicic ash-flow sheets mimic the REE trends of the modern arc lavas in Nicaragua indicating a genetic relationship.

ACKNOWLEDGEMENT

I would like to express my gratitude to all those who gave me the possibility to complete this thesis and my Master's degree at Michigan State University. There is not enough space on this page to *properly* thank even one of the following people for their enormous help, understanding, and support. I can only hope each of you will realize how important you were, and you are, to me…

I am deeply indebted to my advisor, Dr. Thomas A. Vogel, for giving me the chance to be his student, and whose guidance and encouragement helped me in all the time of research for and writing of this thesis. I would like to thank my co-advisor, Dr. Lina C. Patino, who kept an eye on the progress of my work and was always available when I needed her advises regarding my project and my stay at MSU. I would also like to thank, Dr. Bill Cambray, who did not hesitate to be a part of my committee and for providing me with valuable comments on this thesis.

I am grateful to all of my colleagues in the Department of Geological Sciences. I am sincerely thankful to Karen Tefend for being my "big sister" and for all the support. Many thanks to Melissa Wilmot, Dave Szymanski, the petrology group, and my fellow graduate students for giving me the feeling of being at home away from home.

Special thanks are due to my former professors who have encouraged me to go to graduate school: Dr. Caloy Arcilla, Dr. Ed Listanco, and Dr. Kelvin Rodolfo.

I have to thank my roommate Catherine who had been extremely tolerant and understanding of whatever I'm doing or up to. My utmost thanks to my friends Dan, Pam, Monina, Winchelle, Ma-an, Chris, Amy, Kate, and Eric for always being there for me when I needed a friend to talk to.

Last but certainly not the least, I am forever grateful to the love and care of my family, *wala ako sa kinalalagyan ko ngayon kung wala sila*.

TABLE OF CONTENTS

LIST OF TABLES

LIST OF FIGURES

Figure 1. Map of study area: Circles represent sampling location of the 7 different ash-flow sheets; red triangles represent Quaternary volcanoes along the Central American Volcanic arc; numbers in mm/yr represent subduction rate of Cocos Plate under Nicaragua. Map modified from Roger et al. (2002).

Figure 2. Sampling location of the seven different ash-flow sheets in red circles. APOYO: Apoyo, MONTE-: Monte Galan, LAS-SI: Las Sierras, SAN-RA: San Rafael, OSTOCA, Ostocal, COYOL: Coyol, LAS-MA: Las Maderas.

Figure 3. (A) Active quarry site for ignimbrite (Ostocal unit). (B) Typical pumice fragments of various sizes embedded in fine-ash matrix.

Figure 4. Photomicrograph of typical glomeroporphyritic texture in the pumice fragments. (A) Under plane polarized light and (B) under crossed polars. (Apoyo unit, sample # 020617-1o).

Figure 5. (A) Typical oscillatory zoning in plagioclase crystal (Apoyo unit, 020617-2c). (B) Typical sieve/resorved texture in plagioclase suggesting chemical dissolution (Las Sierras unit; 020620-6b).

Figure 6. (A) Corroded plagioclase cores observed in Las Maderas unit (020622-5). (B) Melt inclusions found in plagioclase phenocryst San Rafael unit (020619-1f).

Figure 7. Phenocrysts of clinopyroxene and orthopyroxene (Apoyo unit, 020617-2c). Distinction between these 2 pyroxenes is difficult from petrography alone.

Figure 8. Banded pumice fragment observed under the microscope (Apoyo unit, 020618-5a).

Figure 9. Mafic enclave within a silicic pumice fragment (Las Maderas 020622-5). (A) under plane polarized light and (B) under crossed polars. The phenocrysts content of the enclave are the same as the host pumice but are smaller in size.

Figure 10. Intrusive-like feature of Fe-Ti oxide within an enclave into the silicic glass host (Ostocal unit, 0206 24-2c).

Figure 11. Dove-tail texture observed in plagioclase crystals within the enclave indicating quenched crystallization (Ostocal unit, 020624-2c).

Figure 12. TAS classification diagram of LeBas et al. (19866) of pumice fragment from the seven recognized ash-flow sheets in southern Nicaragua: Apoyo○, Monte Galan ✖, Las Sierras△, San Rafael ✰, Ostocal ◇, Coyol ✢, Las Maderas □. All samples plottled have been normalized to 100% volatile free.

Figure 13. Major element variation against SiO2 (wt. %) among ash-flow units in Nicaragua. Apoyo○, Monte Galan ✖, Las Sierras△, San Rafael ✰, Ostocal ◇, Coyol ✙, Las Maderas □. Filled area represents trend for low TiO2 Quaternary Nicaraguan lavas.

Figure 14. SiO2 histogram of the seven silicic ash-flow sheets. Mean and standard deviation are for the high silica pumice fragments only.

Figure 15. Trace element concentration of the silicic ash-flow sheets versus SiO2 content. Apoyo○, Monte Galan ✖, Las Sierras△, San Rafael ✰, Ostocal ◇, Coyol ✙, Las Maderas □. Filled area same as Figure 13. No Ta data for Nicaraguan lavas.

Figure 16. Cumulative frequency curves (CFC) of trace element ratios of the seven ash-flow units. CFC's of most of the ash-flow sheets show little variation in the trace element ratios, but are distinct from each other. Others show distinct breaks, e.g. Ostocal, Las Sierras (HF/Th). Apoyo○, Monte Galan ✖, Las Sierras△, San Rafael ✰, Ostocal ◇, Coyol ✙, Las Maderas □.

Figure 17. Trace element ratios plotted against distance along the Central American Volcanic Arc (CAVA) (starts in Mexico-Guatemala border, 0km and ends in central Costa Rica, ~1100 km). Red line represent all CAVA lavas and filled area represent Nicaraguan lavas. Apoyo○, Monte Galan ✖, Las Sierras △, San Rafael ✰, Ostocal ◇, Coyol ✙, Las Maderas □.

Figure 18. REE trend for the seven ash-flow units are similar and define a slight MREE depletion pattern (Dy and neighboring elements; normalization values from Sun & McDonough, 1989). Filled area same as Figure 13.

Figure 19. Dy/Lu <1 in some of the silicic ash-flow sheets suggest amphibole in the source melt. Apoyo○, Monte Galan✖, Las Sierras△, San Rafael✰, Ostocal◇, Coyol✙, Las Maderas□.

Figure 20. Calculated Eu anomaly for the seven silicic ash-flow sheets versus SiO2 contents. Apoyo○, Monte Galan ✖, Las Sierras △, San Rafael ✰, Ostocal ◇, Coyol ✙, Las Maderas □.

Figure 21. Primitive mantle-normalized trace element pattern of the seven ash-flow sheets showing distinct island-arc signature (normalization values from Sun & McDonough, 1989). Filled area same as Figure 13.

Figure 22. Relative ages of the seven silcic ash-flow sheets in Nicaragua compared to U/Th ratio. Older units Las Maderas and Coyol have low U/Th ratio similar to Plank et al.'s (2003) observation in the Miocene Nicaraguan lavas. The youngest unit, Apoyo, has high U/Th ratio similar to the Quaternary Nicaraguan lavas (Data from http://www.rci.rutgers.edu/~carr/cageochem080800.txt). Apoyo○, Monte Galan ✖, Las Sierras △, San Rafael ✩, Ostocal ◇, Coyol ✙, Las Maderas □, Nicaraguan Quaternary lavas ··, Nicaraguan Miocene lavas+.

Figure 23. Plagioclase composition for all analyses with respect to distance from the core for each crystal in the pumice fragments of the seven ash-flow sheets. Each symbol represent one plagioclase crystal analyzed within the given ash-flow unit.

Figure 24. Anorthite content of plagioclase rims versus SiO2 content of whole pumice fragment. Apoyo○, Monte Galan ✖, Las Sierras △, San Rafael ✩, Ostocal ◇, Coyol ✙, Las Maderas □.

Figure 25. Analyzed pyroxenes of the silicic ash-flow sheets have a wide range of Mg#. Apoyo ○, Monte Galan ✖, Las Sierras△, San Rafael ✩, Ostocal ◇, Coyol ✙, Las Maderas □.

Figure 26. Calculated temperatures of Las Sierras, Las Maderas, Ostocal and Apoyo units using the 2-pyroxene program QUILF version 6 (Andersen et al., 1993). Other units do not have opx or were not analyzed. Apoyo ○, Las Sierras △, Ostocal ◇, Las Maderas □.

Figure 27. Whole pumice fragment and matrix glass (encircled areas) composition of the ash-flow sheets showing distinct large compositional gap. Gray area represents mafic matrix glass, stippled area represents silicic matrix glass, vertical pattern represents mafic enclaves and horizontal pattern represents melt inclusion in plagioclase.

Figure 28. MgO vs SiO2 of the whole pumice fragment and matrix glass (encircled areas) of the ash-flow sheets. Symbols same as Figure 25.

Figure 29. Model for the genesis of the silicic ash-flow sheets in Nicaragua. Cross-section is not to scale. See text for explanation.

Figure 30. Cartoon depicting 4 possible scenarios during stage 3 in Figure 27. See text for explanation.

Figure 31. DyN/LuN vs LaN/LuN for Nicaraguan ash-flow sheets in comparison with some Costa Rican ash-flow sheets (SiO2 >65 wt%). Costa Rican data from Hannah et al. (2000) and Szymanski et al. (2002).

Introduction

Abundant silicic ash-flow sheets occur in Nicaragua yet little is known about their geochemistry, volume, and age. Studies of volcanism in this area have been concerned primarily with the basaltic and basaltic andesite lavas, and these voluminous silicic ignimbrites have been neglected. Their origin is a matter of considerable interest because generally, the generation of silicic magma is attributed to the assimilation and/or melting of an underlying continental crust. However, no continental crust occurs in this part of Nicaragua.

There are two widely accepted but contrasting models for the origin of silicic magmas in arcs that have been proposed by several workers. The first model is fractional crystallization of basaltic or andesitic melts (Sisson and Grove, 1993; Feely and Davidson, 1994; Grove et al., 1997; Brophy et al., 1999; Hildreth and Fierstein, 2000). This model requires a high percentage of fractional crystallization (as high as 68%) to generate high-silica magma, and in the process would produce cumulate rocks. If this model were to apply to the silicic magmas in Nicaragua, the cumulate rocks would have been produced at depth and have not yet been exposed at the surface since no cumulate rocks are observed in the region. Alternatively, the second model is partial melting of previously emplaced arc-related igneous rocks to explain the origin of silicic magmas in an evolved arc setting (e.g. Beard and Lofgren, 1991; Roberts and Clemens, 1993; Tamura and Tatsumi, 2002; Smith et al., 2003). Dehydration melting experiments on basaltic rocks and their metamorphosed equivalents, amphibolite and eclogite, at various pressures yield partial melts with composition similar to island-arc tonalities and dacites (Beard and Lofgren, 1991; Rapp et al., 1991; Wolf and Wyllie, 1994; Sen and Dunn, 1994; Rapp and Watson, 1995). Tamura and Tatsumi (2002) considered a calc-alkaline andesitic magma to be a source. Influxes of hot basaltic magmas from the mantle wedge would reheat, partially melt and remobilize the still hot and ponded andesitic magma to produce silicic rocks (Tamura and Tatsumi, 2002).

The silicic ash-flow sheets in Nicaragua, like any other ignimbrites, each represent an instantaneous partial evacuation of the magma chamber. Any chemical heterogeneity in the original magma bodies would then be preserved in the ash-flow sheets and therefore, their evolution can be inferred. Two major processes have been attributed as to why chemical heterogeneities occur in silicic ash-flow sheets: (1) involves large-scale differentiation of an originally homogeneous magma body (i.e. Mittlefehltd and Miller, 1983; Baker and McBirney, 1985; McBirney and Nielson, 1986; de Silva and Wolff, 1995); and (2) effects of discrete magma batches emplaced in a magma chamber that were generated by partial melting and melt extraction with distinct compositional groups unrelated to crystal fractionation (i.e. Marsh, 1984; Bergantz, 1989; Sawyer, 1994; Eichelberger and Izbekov, 2000; Eichelberger et al., 2000). However, these discrete magma batches may subsequently be modified by magma mixing, magma mingling, assimilation, and/or crystal fractionation as they ascend to a high-level chamber and/or to the conduit, and possibly even during eruption. Furthermore, Eichelberger et al. (2000) pointed out that the heterogeneity in erupted materials may be a result of chamber recharge either by: (1) mafic magma intruding a more silicic magma, characterized by effusive eruption (i.e. Pinatubo, Karymsky, Ruapehu, New Zealand; Pallister et al., 1992; Nakagawa et al., 1999; Eichelberger and Izbekov, 2000); and (2) silicic magma intrudes a mafic magma body, commonly associated with pyroclastic eruption (i.e. Katmai, Alaska; Eichelberger and Izbekov, 2000).

The purpose of this study is to: (1) document the chemical and mineralogical variations among and within the silicic ash-flow sheets in Nicaragua; and (2) to evaluate these data with respect to the models proposed above for their origin and evolution. Major and trace element whole-rock analyses, petrography, mineral chemistry and analyses of matrix glass, enclaves, and melt inclusions in plagioclases are used to evaluate the models for the genesis of these silicic magmas.

Regional geology and extent of silicic volcanism in Nicaragua

Nicaragua is located along the western margin of the Caribbean plate in Central America (Figure 1). The Caribbean plate is composed of various blocks and microplates and Central America is divided into two main tectonic regions, the Chortis and the Chorotega blocks (Dengo, 1969; Escalante, 1990). The Chortis block has a pre-Mesozoic continental-type crust and encompasses southern Guatemala, Honduras, Northern Nicaragua and the western Nicaraguan Highlands (e.g. Dengo, 1969; Pindell and Barrett, 1990). This block serves as the basement for the northern part of the Central American Volcanic Arc (CAVA). The Chorotega Block on the other hand, is underlain by a thickened basaltic crust, which many workers believe is part of over-thickened oceanic plateau on the western edge of the Caribbean Plate emplaced during the Late Cretaceous-Paleocene and constitute most of the southern CAVA (Pindell and Barrett, 1990; Di Marco et al., 1995; Kerr et al., 1997, Meschede and Frisch, 1998). It was not until the Eocene-Oligocene that the CAVA began to form in the western part of the Caribbean plate as a result of the amalgamation of the Chortis and the Chorotega blocks (Cigolini and Chaves, 1986; Meschede and Frisch, 1998).

The boundary between the Chortis and the Chorotega Blocks is still a matter of controversy. South of Nicaragua, the Santa Elena-Hess Escarpment lineament is believed to mark the boundary between the two tectonic terranes (Bourgois et al., 1984). Hauff et al. (2000) however suggested that the structural boundary may lie south of the escarpment based on the remarkable similarities on trace elements and isotopic contents of the alkaline and picritic rocks from Tortugal and the alkali basalts from Santa Elena, both located in northern Costa Rica. Moreover, ophiolitic rocks studied in detail by Weinberg (1992), which are commonly observed offshore of Panama and Costa Rica but are not found in onshore outcrops, indicate that the suture between the two terranes is located in central Costa Rica. On the contrary, major and trace element data from front arc Tertiary-Recent volcanic rocks in Nicaragua, along with Sr, Nd, and Pb isotope data suggest that the boundary passes through Bluefields in the Caribbean side of Nicaragua and through the Nicaraguan Depression on a NW-SE trending direction (see Figure 1 in Nystrom et al., 1993). Recent geophysical studies using modeling of seismic wide-angle measurements across the Pacific convergent margin of Nicaragua, gravity, earthquake and borehole data, as well as coincident seismic reflection profile, also argue that the suture between these two tectonic blocks is located at the northeastern border of the SE-NW-trending Nicaraguan Depression (Walther et al., 2000). Their argument was based on their reconstructed tectonic evolution of the Nicaraguan margin. They suggested that the collision of an oceanic plateau (i.e. Galapagos hotspot plume or Mid-Cretaceous superplume) in the Upper Cretaceous time left the former trench and margin area in deep water. This is followed by the subsequent trench jumping by about 70km to the SW, which left a portion of ophiolitic crust and upper oceanic mantle underneath the Nicaraguan Depression (Figure 13 in Walther et al, 2000). If this is the case, then most of the observed silicic volcanism in Nicaragua is associated with the oceanic Chorotega block.

The Tertiary-Recent volcanism in Nicaragua is attributed to the present day subduction of the Cocos Plate at 91 mm yr^{-1} (DeMets et al., 1990) in a northeasterly direction beneath the Caribbean Plate. Seismic data define a steeply dipping Benioff zone in Nicaragua with a dip increasing from 25° in the seismogenic zone to 84° between 100 and 220 km depth (Burbach et al., 1984; Wilson, 1996). The associated chain of volcanoes is located in the western edge of the Nicaraguan Depression, which is a 50-km wide extensional structure formed in the Plio-Pleistocene and has been defined as a half-graben parallel to the trench that hosts Lake Nicaragua and Lake Managua (McBirney and Williams, 1965; Weinberg, 1992; Elming et al., 2001). There are 21 Quaternary volcanic centers in Nicaragua, which are closely spaced with an average of 25 km between central craters (Van Wyk de Vries, 1993). As compared with the other eruptive centers in CAVA, the volcano summits in Nicaragua are relatively lower with smaller volumes of erupted materials (Van Wyk de Vries, 1993). The volcanic deposits in Nicaragua are chemically bimodal, dominated by basaltic to basaltic andesite flows, and dacitic to rhyolitic ash-flow sheets and air-fall deposits (Ehrenborg, 1996). Slab signature is strongest in the Nicaraguan lavas as compared with the other CAVA lavas. This signature is manifested by the high Ba/Th and Ba/La ratios as well as the abundance of ^{10}Be (Carr et al., 1990; Patino et al., 2000; Morris et al., 1990). An interesting characteristic of the Nicaraguan lavas is the high U/Th ratio of the younger flow units (<7Ma) relative to the older lavas and to the rest of the CAVA lavas (Plank et al., 2002). This has been interpreted as a result of the closure of the Panama gateway, which led to the "carbonate crash" at 10 Ma followed by high organic carbon burial in the sediments (Lyle et al., 1995; Plank et al., 2002).

The silicic ash-flow sheets for this study cover an area of approximately 6,400 km^2 (Figure 1 and 2). The oldest pyroclastic flow unit is represented by the Coyol Group, which is believed to have originated from El Limon caldera, a >30km diameter structure formed between 12 and 16 Ma (Ehrenborg, 1996). K-Ar dates of the Coyol Group ranged from 4.3 to 24.7 Ma (Ehrenborg, 1996), whereas deep sea tephra stratigraphy combined with Ar-Ar dating obtained an age of 12.3 to 18.4 Ma (Sigurdsson et al., 2000). The youngest ignimbrite is dated at 23,000 yrs BP by radiocarbon dating and found along the periphery of the Apoyo caldera (Sussman, 1985). Sussman (1985) estimated that the volume of the last erupted materials from the Apoyo caldera is 10.7 km^3 dense-rock equivalent (DRE). The stratigraphy of the Tertiary volcanic rocks in Nicaragua is described by Ehrenborg (1996). He noted three major volcanic events: (1) rhyolitic shield volcanism in the Oligocene, which produced the Highland ignimbrites; (2) extrusion of basaltic to andesitic magmas along the Pacific coast and the construction of the Coyol volcanic arc during the Miocene; and (3) creation of the modern volcanic arc during the Pliocene-Pleistocene after the southwestward shift of arc volcanism.

The silicic ash-flow sheets in Nicaragua

Formatting note

The images in this thesis are presented in color.

Sampling Methods

More than 300 whole pumice fragments and air fall deposits were collected during 2 field seasons, July 2001 and June 2002. Table 1 lists the sampling locations for all the samples collected. The majority of these samples were taken from active quarries (Figure 3A) and road cuts, which are easily accessible. The samples represent the variation among glassy pumice fragments present within an outcrop (Figure 3B). Sampling was based on color, size, degree of welding (if present), and the types and amount of phenocrysts in the observed hand samples.

Sample preparation

One hundred seventeen pumice fragments were selected and analyzed for mineral and element composition for this project. The basis for sample selection process for the analyses is the same as the sampling methods done in the field – to sample the variation present. Whole pumice fragment major element and selected trace element compositions were analyzed by X-ray fluorescence spectrometry (XRF) for the all selected samples. Additional whole pumice fragment trace and rare-earth element compositions were analyzed using Laser Ablation Inductively Coupled Plasma Mass Spectrometer (LA ICP-MS). Based on the variation in chemical composition of these analyzed samples, a small number of pumice fragments were selected and analyzed for phenocrysts major element contents using the Electron Probe Micro Analyzer (EPMA) at University of Michigan.

Fused glass disks were used for both XRF and LA ICP-MS analyses. The disks were made from whole pumice fragments that were powdered using an aluminum flat plate grinder after passing them through a chipmunk. Three grams of finely ground pumice fragment powder were diluted by adding 9.0g of lithium tetraborate ($Li_2B_4O_7$) and 0.5g of ammonium nitrate (NH_4NO_3) as an oxidizer. These were then mixed and melted in platinum crucibles at 1000 °C of oxidizing flame for >20 minutes while being stirred with an orbital mixing stage. The melt was poured into platinum molds making the glass disk for analyses. The fused disks were analyzed using a Rigaku S/Max X-ray fluorescent spectrograph. XRF major element analyses were reduced by a fundamental parameter data reduction method (Criss, 1980) using XRFWIN software (Omni Instruments), while XRF trace element data were calculated using standard linear regression techniques. For LA ICP-MS trace element data, a Cetac LSX200+ laser ablation system was used coupled with a Micromass Platform ICP-MS and using strontium, determined by XRF, as an internal standard. Trace element data reduction was done using MassLynx software. Prior to any calculations, the background signal was subtracted from the standards and samples. Element concentration in the samples were calculated based in a linear regression method using NIST-612, BHVO, W-2, JB-1, JB-2, JB-3, JA-2, JA-3, BIR, STM1, and RGM1 standards.

For electron microprobe analyses, select pumice fragment thin sections were used based on a wide range of chemical compositions. The minerals analyzed were plagioclase, clinopyroxene, orthopyroxene and in addition, the matrix glass, enclaves and melt inclusions present in the plagioclases. Analyses were performed on a Cameca SX 100 EPMA equipped with five wavelength spectrometers using an accelerating potential of 15kV, a 6μm beam spot size, counting time of 3min/mineral, and a 10nA beam current.

Petrography and mineralogy

Petrograhic analyses were done on thirty selected thin sections of pumice fragments. They represent a wide range of chemical compositions and color (e.g. white, gray, and black). The lighter colored pumice fragments are typically more silicic than the darker pumice fragments. They contain varying amounts of plagioclase, clinopyroxene, orthopyroxene and Fe-Ti oxide phenocrysts, either in clots or as isolated crystals. Crystals larger than 0.5mm were considered phenocrysts and smaller crystals were considered part of the groundmass.

Petrographically, there is no visible distinction among the ash-flow sheets except for the abundance of phenocrysts content. Generally, the amount of phenocrysts present in the pumice fragments decrease with increasing silica content. Crystal-rich and black pumice fragments are usually basaltic to andesitic in composition. They contain 10- 55% glass, 25-50% plagioclase, 5-10% orthopyroxene, 10-20% clinopyroxene, and 5-10% Fe-Ti oxides. Crystal-poor samples, which are dacitic to rhyolitic, have the same phase assemblages but in considerably fewer amount. They contain 70-90% glass, 5-10% plagioclase, 1-5% orthopyroxene, 2-10% clinopyroxene, and 1-5% Fe-Ti oxides. The nearly aphyric samples are usually the white pumice fragments and the phenocrysts occur within glomerophyric clots (Figure 4).

Plagioclase crystals, which are the most abundant phenocrysts, occur as medium- to coarse-grained, euhedral to subhedral crystals, and most exhibit albite twinning and oscillatory zoning (Figure 5A). Often, these crystals have embayed-, sieved-, or resorbed-textures (Figure 5B) while some plagioclases have corroded cores (Figure 6A). These textures indicate disequilibrium between the crystal and the melt. A few plagioclases contain melt inclusion (6B) and some of these inclusions are devitrified.

Phenocrysts of pyroxene are less abundant than the plagioclase and occur mostly as medium-grained subhedral crystals. Usually, clinopyroxene and orthopyroxene either occur together as clots or in aggregates with the plagioclase. It is difficult to distinguish a clinopyroxene from an orthopyroxene based on optical properties alone (Figure 7) and can only determined through microprobe analyses. Generally, the clinopyroxenes are more abundant than the orthopyroxene in any given pumice fragment in the ash-flow sheets.

The Fe-Ti oxides (e.g. ilmenite, magnetite) occur as minor phases, either in aggregates with other phenocrysts or as euhedral and isolated crystals. Prismatic apatite crystals occur as an accessory mineral found within the plagioclase.

A few banded pumice fragments have been observed within the silicic ash-flow sheets (e.g. Apoyo unit; Figure 8). They usually have gray color and their composition is transitional between the silicic and the mafic pumice fragments. These banded pumice clasts are interpreted to be the result of mingling between the silicic and mafic magmas. Incomplete mixing was probably due to viscosity contrast between the two magmas as manifested by the flow banding present.

Mafic enclaves occur within some of the pumice fragment units (i.e. Las Maderas, Ostocal; Figure 9). These enclaves are mostly >2mm in size and contain the same mineralogy as the host pumice but are more crystal-rich and the phenocrysts sizes are relatively smaller. Some enclaves show an intrusion-like feature of Fe-Ti oxide into the host pumice fragment (Figure 10) These features are indicative of mingling between the silicic and mafic magmas. Within these enclaves are dove-tail textured plagioclases (Figure 11), which suggest quenched crystallization process after the two magmas came in contact.

Geochemistry

Whole Rock Geochemistry

Major element variations

Whole pumice fragment major and trace element data are listed in Table 2. All major element values used in the discussion and plots have been normalized to 100% volatile free because of secondary hydration of glassy pumice. Total iron is calculated as $Fe_2O_{3(T)}$.

The compositions of the pumice fragments in the ash-flow sheets from Nicaragua vary from basalt to rhyolite, with SiO_2 ranging from 50.92 to 71.47 wt% (Figure 12). The concentrations of the major element oxides, except the alkalies, decrease with silica content and define distinct chemical trends for these ignimbrites (Figure 13). Most of these ignimbrites are enriched in potassium and fall within the medium- to high-K calc-alkaline field, with K_2O range from 0.5 to 5.71 wt. % (Figure 12). Based on these chemical variations and stratigraphic location, seven distinct ash-flow sheets were recognized. These ash-flow sheets are Apoyo, Las Sierras, and 5 informally named units referred here as Coyol and Las Maderas of the Coyol Group (Ehrenborg, 1996), Ostocal, Monte Galan, and San Rafael. The pumice fragments with lower Si_2O content in any given ash-flow units occur within a trend similar to the Quaternary Nicaraguan lavas (Figure 13).

Considering all units, the Apoyo ash-fow sheet has the widest range in SiO_2 content from 50.9 to 69.1 wt %. It is however dominated by high-SiO_2 pumices (mean of the high SiO_2: 67.78 wt. %; Figure 14) with distinctly low TiO_2 and K_2O trend than the other ash-flow units (Figure 12). The Las Maderas unit, like Apoyo, has low-SiO_2 pumice fragments and is dominated by dacitic pumices (mean of the high SiO_2: 64.03; Figure 14). This unit has a distinct high Al_2O_3 and K_2O content relative to the other units (Figure 13). The Coyol ash-flow sheet, like Apoyo and Las Maderas, contain both low- and high-SiO_2 pumice fragments (Figure 14) but samples are mostly trachydacites (Figure 12). This unit has the highest K_2O content for all the ash-flow sheets with a distinguishing trend, which range from 2.04 to 5.71 wt. % (Figure 13). The Las Sierras ash-flow sheet has the highest SiO_2 content for all the units sampled, and range from dacitic to rhyolitic composition, 66.95 to 71.47 SiO_2 wt. % with a mean composition of 70.16 wt. % (Figure 12, 13, 14). The Monte Galan unit is mostly of rhyolitic composition (average: 70.18 wt. % SiO_2; Figure 14) and in many aspects resembles the major oxide content of the Las Sierras ash-flow sheet (Figure 13). Ostocal and San Rafael units both are dominated by dacitic tuffs with an average composition of 67.15 and 64.28 wt. % SiO_2, respectively (Figure 13) but each have a distinctive TiO_2 and $Fe_2O_{3(T)}$ content (Figure 13).

Trace element variations

Trace element abundances for all the seven ash-flow sheets in Nicaragua are listed in Table 2. Within an ash-flow sheet, the pumice fragments show little variation in trace element abundances. However, a weak linear relationship of some trace elements with silica content occurs in some units (Figure 15).

Cumulative frequency distribution curves (CFCs) of incompatible trace element ratios among the seven the ash flow sheets show small but distinct variation (Figure 16). Such distinctions among these ignimbrites further demonstrate the occurrence of seven compositionally different ash-flow sheets in the region. Las Sierras and Monte Galan have similar La/Yb ratio but they show distinction in their Hf/Th ratio. All other ash-flow units fall on a distinct CFC and this is consistent with each unit having a separate source. Distinct "breaks" or "gaps" in incompatible trace element ratios (i.e. Hf/Th; Ba/Nb) on the CFC plots are also observed within some of the ash-flow units (i.e. Las Sierras, Ostocal; Apoyo, Las Maderas). These "breaks" or "gaps" imply that fractional crystallization is not a dominant process but rather played a minor role in the chemical heterogeneity of these ignimbrites. If fractional crystallization were the dominant mechanism, then the trend for any of these ash-flow sheets would fall along a single continuous curve. The "breaks" or "gaps" suggest that another process (i.e. different source area) may have contributed for such incompatible trace element trend.

Trace element ratios of the seven ash-flow sheets mimic the trace element ratios of the low TiO_2 Quaternary front arc lavas in Nicaragua (Figure 17). The Ba/La and La/Yb ratios of the ignimbrites are consistent with the modern arc lavas (Carr et al., 1990) along with Ba/Rb and Hf/Th ratios (Figure 17). Rare earth element (REE) trends for these silicic rocks are similar and define a slight middle rare earth element (MREE) depletion (Figure 18). A Dy_N/Lu_N ratio <1 further supports this observation particularly in the younger ash-flow sheets (Figure 19). REE ratios of the older ash-flow sheets (i.e.

Coyol and Las Maderas) show an increasing La_N/Lu_N with increasing Dy_N/Lu_N ratio, while younger ignimbrites (i.e. Las Sierras, Monte Galan) have relatively constant La_N/Lu_N with increasing Dy_N/Lu_N ratio (Figure 19). This difference could be a function of the degrees of melting that each unit has undergone.

Some ash-flow sheets like Ostocal, Las Maderas, and Las Sierras units contain a small negative Eu anomaly (0.67 to 0.90). Eu anomaly is a measure of Eu/Eu*, which is calculated from the linear equation of the line connecting Sm and Tb on a REE chondrite normalized plot (for equations, refer to Hannah, 2000). Such negative Eu anomaly in these units may result from plagioclase fractionation. However the Apoyo unit contains a slight positive Eu anomaly (1.09 to 1.13) (Figure 20), which may reflect plagioclase accumulation. Spider diagrams normalized to primitive mantle concentration (Sun and McDonough, 1989) show enrichment in the large-ion lithophile elements (LILEs) and depletion in the high field strength elements (HFSEs) (Figure 21) for all units, which is consistent with the composition of melts associated with subduction zone environment.

Relatively young ash-flow sheets correspond to high U/Th ratio while older units tend to have lower U/Th ratio. This is similar to the observation made by Plank et al. (2002). They related this change from low to high U/Th ratio resulting from the "carbonate crash" at 10 Ma, where the istmus of Panama changed the circulation patterns in the eastern Pacific Ocean (Lyle et al., 1995). This is supported by the fact the youngest ash-flow sheet in this study is the Apoyo unit, with an age of 23,000 yrs BP (Sussman, 1985) and has a high U/Th ratio of 0.45 to 1.30. The oldest units are from the Coyol Group, the Coyol and Las Maderas ash-flow sheets, with an age of Early Miocene (Ehrenborg, 1996) and have a low U/Th ratio of 0.35 to 0.52 and 0.29 to 1.09, respectively. From here, it is inferred that the other units, Monte Galan, Las Sierras, San Rafael, and Ostocal correspond to an age younger than the Coyol Group since they have a higher U/Th ratio (Figure 22).

Mineral Chemistry

Electron microprobe analyses of phenocrysts from select pumice fragments are listed in Table 3. The plagioclase analyses were obtained from the core, middle and rim. Analyses in the middle of the plagioclase were usually halfway between the core and the rim of the crystal. Representative clinopyroxene and orthopyroxene grains were analyzed and at least 2 glass analyses from each pumice fragment and from the mafic enclave (if present) were obtained. A number of melt inclusions present in the plagioclase were also analyzed.

The range of plagioclase compositions for all the seven ash-flow sheets is from An_{25} to An_{91} (Figure 23). Some plagioclases show a more calcic rim and a sodic core (e.g. Monte Galan, Ostocal) while others shows calcic core with very low sodic rim (e.g. Apoyo) (Figure 23). Both normal and reverse zoning in these plagioclases were observed in any given ash-flow unit. The composition of the plagioclase rims would be expected to be in equilibrium with the last liquid. Except for Ostocal, all ash-flow sheets have plagioclase grains with rims that display a wide range of composition (Figure 24). They vary from as low as 20% to as high as 70% An content within a single pumice fragment (i.e. Monte Galan and Apoyo). This large variation indicates that the plagioclases were not in equilibrium with the last crystallizing liquid/s prior to the eruption of these ignimbrites. Neither the coexistence of both normal and reverse zonations of the plagioclase phenocrysts nor the large variations in An content in the plagioclase rims within a pumice fragment can be explained by simple closed-system crystallization. It would imply that at least 2 different magma bodies, a high-silica and a low-silica magma, are in contact and did not reach compositional equilibrium. Another indicator of these compositional disequilibrium is the high An content (up to 91% An) of some of the plagioclase cores, particularly in Apoyo and Las Sierras units (Figure 23) because silicic rocks typically have plagioclases with An content less than 50%.

For clinopyroxene phenocrysts, the composition range from $Wo_{44.6-32.4}$ $En_{48.4-32.5}$ $Fs_{29.0-13.2}$ while orthopyroxene composition range from $Wo_{9.6-2.0}$ $En_{67.1-40.7}$ $Fs_{50.5-30.1}$. Orthopyroxenes were not observed in some ash-flow sheets (i.e. San Rafael, Monte Galan and Coyol). It is possible that they are present but not analyzed due to inability to recognize an orthopyroxene from a clinopyroxene through optical properties. The Mg# for both clinopyroxene and orthopyroxene among the seven ash-flow sheets show a wide range of variation as shown in Figure 25. The Ostocal and the San Rafael units have a distinctive Fe-rich orthopyroxene and clinopyroxene respectively, while Las Maderas and Apoyo ash-flow sheets have Mg-rich clinopyroxene. This indicates that each unit has distinct source composition unrelated to the other units. Figure 26 shows the calculated temperature at which the phases of the last crystallizing liquid were last in equilibrium using the program QUILF version 6 (Andersen et al., 1993). The temperature was calculated using two pyroxene thermometer in clinopyroxene + orthopyroxene bearing pumice fragments. Each ash-flow unit has a distinct temperature, and even within a single flow unit, 2 different temperatures have been calculated. The calculated temperature are: Apoyo: 910± 19 and 925± 39; Las Maderas: 941 ±71 and 1012 ±73; Las Sierras: 959 ± 69 and 969±144; and Ostocal: 1214 ±139 and 1086 ± 274. Even though the uncertainty of the calculated temperatures is high for some ignimbrites (i.e. Ostocal), they still indicate thermal distinction of the source magma among the ash-flow sheets.

Matrix glass composition for the pumice fragments, including the mafic enclaves and melt inclusions in plagioclases vary with the SiO_2 of the whole pumice fragment and range from 47.0 to 76.6 wt %. Figure 27 and 28 show the plots of MgO and K_2O versus SiO_2 for the matrix glass, mafic enclave, and melt inclusion compositions together with the whole pumice fragment content for each ash-flow unit. The matrix glass in the mafic enclaves found in Las Maderas and Ostocal units have lower SiO_2 and K_2O contents than the matrix glass of their respective host pumice fragment. The MgO content of the Ostocal mafic enclaves is higher than the host pumice fragment but Las Maderas mafic enclaves contain both high and low MgO contents. Melt inclusions in plagioclase phenocrsyt have lower SiO_2, K_2O and MgO content than the host pumice fragment. The SiO_2 and K_2O contents of the matrix glass overlap the composition of the whole pumice fragment for Coyol, Monte Galan and San Rafael units (Figure 27 and 28). A large compositional gap occurs in the whole pumice fragment and in the matrix glass data for any of the ash-flow sheets, including the mafic enclave in Las Maderas and Ostocal units and the melt inclusions in San Rafael ash-flow sheet (Figure 27 and 28). This compositional gap represents at least two evolving magma batches that did not attain thermal equilibration and were not stored in prolonged contact before eruption. This scenario is similar to what occurred in the Aniakchak Caldera and the enclave-bearing Mount Dutton eruptions, both in Alaska, where a large difference in the whole rock and melt compositions are observed (Eichelberger et al., 2000).

The generation of the silicic ash-flow sheets of southern Nicaragua

Abundant silicic magmas are typically rare in island arc environment because they are generally thought to be generated by assimilation and/or melting of underlying continental crust. The seven silicic ash-flow sheets observed in Nicaragua may therefore provide excellent means to infer their origin in this island arc environment. Distinct mineralogical and chemical heterogeneities occur among and within the silicic ash-flow units and these can be used to determine magmatic processes that occur in the magma chamber prior to eruption since ash-flow tuffs represent instantaneous evacuation from the magma chamber. Two models have been proposed to generate these silicic ash-flow sheets: (1) fractional crystallization of basalt or basaltic andesite and (2) partial melting of previously emplaced arc-related magma. Subsequent magma mixing, magma mingling, and/or crystal fractionation may modify the produced melt. Each of these models will be evaluated individually.

Fractional Crystallization

The evolution of silicic magmas by fractional crystallization of basaltic or basaltic andesite melts was proposed by several workers (Sisson and Grove, 1993; Feely and Davidson, 1994; Grove et al., 1997; Brophy et al., 1999). In order to attain high-silica magmas, a large amount of fractionation is involved (~68%; e.g. Grove et al., 1997). For this to be produced, cumulate rocks such as anorthosite would have to be generated as well. However, no cumulate rocks have been reported in Nicaragua. Even in areas where the roots of silicic volcanic rocks are thought to be exposed, such as in the Cordillera de Talamanca in southeastern Costa Rica, cumulate rocks are rare (Alvarado and Carr, 1993). Brophy et al. (1999) proposed that silicic calc-alkaline rocks might originate by fractionation near the crust-mantle boundary, which would explain the scarcity of exposed cumulate rocks. The base of a thickened crustal province, like the CLIP, might serve as an ideal density trap for magmas to pond (e.g. Hauff et al., 1997, Sinton et al., 1997, Hauff et al., 2000).

Each ash-flow sheet has a distinct CFC trace element ratio trend (Figure 16). Even within some ash-flow sheets such as Ostocal and Las Sierras, "breaks" or "gaps" in their trace element ratio CFC occur (e.g. Hf/Th) and these "breaks" or "gaps" suggest that another process such as a different source area for each trend, may have contributed to such distribution trend.

The seven silicic ash-flow sheets lack significant Eu anomaly (Figure 18). However, this does not necessarily mean that plagioclase fractionation did not occur. Most calc-alkaline rocks, such as the silicic ignimbrites of Nicaragua, are produced under an oxidizing environment where Eu behaves as Eu^{3+} and therefore Eu would behave like the other REEs and no Eu anomaly would be observed even if plagioclase fractionated. Nonetheless, Las Sierras and Las Maderas units contain slight negative Eu anomaly ($Eu/Eu^* < 1$) with increasing SiO_2 (Figure 20), and would imply that fractional crystallization may have played a minor role in their production and that an oxidizing state may not be truly the case. The Apoyo ash-flow sheet, the only unit with a small positive Eu anomaly ($Eu/Eu^* > 1$), suggests the effect of plagioclase accumulation. However, the Eu/Eu^* of the more mafic and more silicic pumice fragments fall into two distinct groups that can not be related by simple fractional crystallization (Figure 20). If the silicic tuffs fractionated from the more mafic ignimbrites, a continuous linear trend would be expected, but this is not the case for the Apoyo unit.

Oscillatory zoning in plagioclase is a widespread phenomenon observed in many volcanic rocks (e.g. Anderson, 1984; Kuritani, 1998; Ginibre et al., 2002, Halama, et al., 2002). The observed chemical zonations in plagioclase phenocrysts from the seven silicic ash-flow sheets can be used to elucidate magma-chamber and emplacement processes. Plagioclase phenocrysts in any of the ignimbrite units commonly display abrupt fluctuations in An content (up to 25% in Apoyo unit) (Figure 23). The abrupt shifts from a calcic core to a sodic rim (e.g. Apoyo) or the trend from a more sodic core into a calcic rim (e.g Monte Galan, Ostocal) could correspond to the well-developed dissolution surfaces in the plagioclase crystals (e.g. embayed, resorbed textures). The coexistence of both normal and reverse zonations of the plagioclase phenocrysts within the pumice fragments, the large variations in An content in the plagioclase rims from a given unit (Figure 24), and the very high An content of the core (>50 An%) for all the units except Ostocal imply that each ash-flow unit can not be generated by simple crystal fractionation (Figure 23). If fractional crystallization of the melt produced these plagioclases, then they should have normal uninterrupted zonation, little variation in the plagioclase rim composition since they should be in equilibrium with the last crystallizing liquid, and an An content of <50%, typical of silicic melts. The observed characteristics of the plagioclase phenocrysts however suggest compositional and thermal disequilibrium within the magma chamber contradicting the process of fractional crystallization.

The observed compositional discontinuity within both the pumice fragments and the matrix glass, including the mafic enclaves and melt inclusions in the plagioclases

(Figure 27 and 28) suggest chemical and thermal disequilibrium in the magma chamber (e.g. Eichelberger et al., 2000), in accordance with the plagioclase phenocrysts. If these silicic ash-flow sheets were related by progressive fractional crystallization and/or even by assimilation, it is impossible to have a discontinuity in melt composition without a corresponding discontinuity in temperature (Eichelberger et al., 2000). This large gap of unrepresented compositions can be accounted for by some special mechanism such as sidewall crystallization with efficient expulsion and collection of melt, producing a gravitationally stable silicic over mafic layering (McBirney, 1980; Turner and Gustafson, 1981; McBirney et al., 1987; Bacon and Druitt, 1988) or by incomplete mixing of a silicic and mafic magma in the chamber (e.g. Snyder and Tait, 1998; Eichelberger et al., 2000). Sidewall crystallization has been envisioned to be an effective mechanism to produce ryholitic magma such as those erupted during the 1912 Katmai eruption in Alaska (Hildreth and Fierstein, 2000). However, should fractional crystallization generate the trends within the seven high-silica rocks in Nicaragua, individual glass matrix analyses should show higher SiO_2 and K_2O with lower MgO when compared with the whole pumice fragment analyses. But most of the silicic ash-flow sheets contradict this except Apoyo, Las Maderas and Ostocal (Figure 27 and 28). Some of the matrix glasses are more mafic than the whole pumice fragment indicating that fractional crystallization did not generate these matrix glasses. Such variations in the matrix glass of the silicic ignimbrites are best explained by mingling of at least 2 different magma type, a silicic and a mafic magma and this will be discussed more in detail below.

The presence of crystal-rich mafic enclaves (Figure 9) within the silicic pumice fragments (eg. Las Maderas, Ostocal) is another indicator of disequilibrium in the magma chamber, a process unrelated to fractional crystallization. These mafic enclaves record the intrusion of a mostly liquid mafic magma into a mushy silicic magma (e.g. Eichelberger et al., 2000), supporting the process of magma mingling. Such interaction is shown in Figure 10, where an oxide mineral of the mafic enclave "invades" the matrix glass of the silicic host.

In summary, trace element variations among the ash-flow sheets, Eu/Eu*, plagioclase zonations, compositional gaps, and mafic enclaves can be used to reject the model of fractional crystallization from a low-silica magma to a high-silica magma as a dominant mechanism to produce any of the seven silicic ash-flow sheets in Nicaragua.

Partial melting of previously emplaced arc-related igneous rock

Partial melting of previously emplaced arc-related igneous rocks has been cited as a mechanism to generate high-silica rocks in an island arc setting (Beard and Lofgren, 1991; Roberts and Clemens, 1993; Wolf and Wyllie, 1994; Nakajima and Arima, 1998; Tamura and Tatsumi, 2002; Smith et al., 2003). Dehydration melting experiments of basaltic compositions carried out by Beard and Lofgren (1991) under low pressure have yielded rhyolitic melts coexisting with the anhydrous assemblage plagioclase + orthopyroxene + clinopyroxene + Fe-Ti oxides consistent with the phenocrsyt assemblage of the seven silicic ash-flow sheets in Nicaragua. Although the rhyolitic melts produced by Beard and Lofgren (1991) have the same decreasing TiO_2, CaO, MgO, and Fe_2O_3 with increasing K_2O and SiO_2, their melts are more silicic and have lower potassium than the Nicaraguan ash-flow sheets. Tamura and Tatsumi (2002) argued that 20-30% dehydration melting of solidified calc-alkaline andesite in the crust rather than basaltic magmas play an important role in producing high silica rocks (e.g. Izu-Bonin arc). They suggest that water-saturated andesites solidify at depth and never erupt to the surface and these andesites remelted to produce the high-silica deposits in Izu-Bonin. Major elements and phenocryst assemblage of the silicic ash-flow sheets in Nicaragua are similar to the rhyolitic rocks in Izu-Bonin arc (Tamura and Tatsumi, 2002) but the K_2O content is relatively enriched. This enrichment in K_2O may be attributed to either the role of amphibole in the source and/or the influence of sediment-derived fluids, which will be discussed in detail below.

As discussed above, each of the silicic units are not produced by fractional crystallization alone and are independently generated. The increasing Rb and Zr and decreasing Sr with SiO_2 (Figure 15) could therefore indicate that there has been an involvement of an older, altered oceanic crust. In most systems where plagioclase is fractionating, Sr is greatly reduced and the Sr value approaches zero. However, the Sr content of any of the ash-flow sheets is high (>100; Figure 15) indicating the involvement of an altered crust. Such crust must have a total crustal thickness of 15-20 km (~0.5 Gpa), where amphibole is a stable phase, in order to generate silicic magmas (i.e. Smith et al., 2003). The breakdown of amphibole at some temperature between the wet and dry solidi (~ 900° C) triggers dehydration melting of the lower crust (i.e. Beard and Lofgren, 1991; Smith et al., 2003). Smith et al. (2003) pointed out that once a fluid is present, heat can propagate relatively fast by convection to produce large batches of silicic magmas. The observed slight depletion in MREEs in the younger ash-flow units (Figure 18) indicates the stability of amphibole in the source magma, which has a strong affinity for the MREEs. This is apparent from the observed Dy_N/Lu_N ratios in the younger silicic ash-flow sheets, which are <1 suggesting that amphibole is in the source rock (Figure 19). Such dehydration melting of an amphibole-rich source also explains the enrichment in K_2O content of the ash-flow sheets as mentioned above. The relative low La_N/Lu_N ratios of the pumice fragments suggest a high degree of melting or from a source with low La_N/Lu_N ratio, while increasing La_N/Lu_N ratios with increasing Dy_N/Lu_N ratios imply crystal fractionation of a melt derived from an amphibole-rich source. If the subsequent differentiation did not occur, the Dy_N/Lu_N ratio would remain constant even under varying degrees of melting.

It is important to note that efficient partial melting of amphibole-bearing previously emplaced arc-related igneous rock to generate the silicic ash-flow sheets is governed by periodicity and multiplicity of basaltic intrusion from deep source into the lower crust (e.g. Petford and Gallagher, 2001; Annen and Sparks, 2002). Continuous and multiple production of basaltic magma from the melting of the mantle wedge due to the fluids coming off the dehydrating, subducted Cocos plate would ascend to the lower crust and effectively partially melt the previously emplaced arc-related magma. Segregation and ascent of partial melt would then produce the silicic ash-flow sheets.

Because the silicic ignimbrites contain high amounts of Ba/La ratio similar to the modern Nicaraguan lavas, which is interpreted to indicate high sediment influx (Carr et al., 1990; Patino et al., 2000), it implies that the source rock of the silicic ash-flow sheets were produced by the same manner. This is complimented by the high degrees of melting as shown by the low La_N/Lu_N ratio in the silicic ash-flow sheets. These sediment-derived fluids are often enriched in "fluid-mobile" elements such as Ba, Rb, K, and Sr (Tatsumi et al., 1986), which explains the K_2O enrichment in the silicic tuffs accompanied by the consumption of amphibole during partial melting.

Magma Mingling

Ash-flow sheets such as observed in Nicaragua, represent an instantaneous partial evacuation of the magma chamber and therefore any variation indicates heterogeneity in the pre-eruptive magma. Mafic enclaves and large compositional gaps in eruptive products in the ash-flow sheets are thought to indicate mafic-silicic magma interaction, and many workers have suggested that such magma mixing/mingling could trigger the eruption (Sparks et al., 1977; Eichelberger, 1978; Stimac et al., 1990; Pallister et al., 1992; Eichelberger et al., 2000; Eichelberger and Izbekov, 2000). Magma mixing/mingling can occur effectively during the injection of either a mafic or silicic magma into the chamber and/or during the ascent into the conduit (Feeley and Dungan, 1996; Eichelberger et al, 2000; Kuritani, 2001).

The occurrence of banded pumice within the silicic ash-flow sheets resulted from incomplete mixing of the coexisting magmas (Figure 8) as they ascend through the conduit. Crystal-rich mafic enclaves (Figure 9) present in the pumice fragments of Las Maderas and Ostocal units indicate mingling of the coexisting magmas. These mafic enclaves record the partial disintegration of the invading basaltic magma, strewing out blobs of basaltic debris as it came in contact with the rhyolitic magma (e.g. Eichelberger, 1978; Eichelberger et al, 2000). The quenched textures exhibited by the phenocrysts (e.g. dove-tail texture in plagioclase) in the enclaves (Figure 11) are the result of undercooled crystallization of the mafic magma. The interaction of these distinct magmas is also manifested by the "intrusive-like" feature of Fe-Ti oxide phenocrysts in the enclave into the glass matrix of the silicic host (Figure 10).

Chemical and thermal disequilibrium induced by the interaction of mafic and silicic magmas are recorded by textures and composition of the plagioclase phenocrysts in the silicic pumice fragments. Such disequilibrium resulted in: (1) embayed, resorbed and sieved crystal forms (Figure 5B) indicating incomplete dissolution, (2) compositional reverse zoning (Figure 23), (3) abrupt shifts of both sodic plagioclase into a more calcic composition, and calcic composition into a more sodic plagioclase (Figure 23), (4) remarkably anorthitic core (>An_{70}, e.g. Apoyo, Las Sierras; Figure 23), and the wide range in anorthite content of the plagioclase rims for a given pumice fragment (Figure 24).

A strong argument in favor of magma mingling in the silicic ash-flow sheets in Nicaragua is the remarkable large compositional discontinuity within the pumice fragments and their matrix glass, the mafic enclaves and the melt inclusion compositions (Figure 27 and 28). These large differences in melt compositions demonstrate the lack of thermal equilibration and require that the two mingling magmas were not stored in prolonged contact (Eichelberger et al., 2000). The similarity of the silicic matrix glass with the silicic host pumice fragment in terms of SiO_2 and K_2O for some of the ignimbrite units (i.e. San Rafael, Coyol, Monte Galan) and although no mafic host pumice fragment can be compared with the observed mafic matrix glass, mafic enclaves, and melt inclusion compositions, is a significant evidence that a silicic magma intruded a mafic magma. This is comparable to the erupted Aniakchak ignimbrites in Alaska, where the invading silicic magma interacted with the mafic magma in a limited way and weakly contaminated each other (Eichelberger et al., 2000). The silicic replenishment case is further supported by the nearly aphyric texture of the silicic pumice fragments. As Eichelberger et al. (2000) pointed out, these silicic ignimbrites are crystal-poor not because the parent magma was sitting at the roof of the chamber and heated from below by a more mafic magma, but because they had just arrived from the deep source, after they were produced from partial melting of a previously emplaced arc-related igneous rock. This silicic intrusion scenario is the reversal of the enclave-bearing ignimbrites where mafic recharge is envisioned (i.e. Las Maderas, Ostocal). Eichelberger et al. (2000) made a distinction that mafic recharge are enclave-bearing and the enclaves are enriched in silica and potassium relative to their host rocks and the contact between the magmas is prolonged because the mafic entrant is initially denser than the resident magma. However, even for the enclave-bearing units in Nicaragua, the silicic and mafic matrix glass, and the silicic and mafic host pumice respectively, are still similar in silica and potassium content indicating silicic recharge. Nonetheless, it is possible that the enclaves came from the roof or walls of the chamber and were just picked up by the intruding silicic magma as it ascend to the conduit. Further investigation on these cases needs to be done but is not within the scope of this study. For whatever case applies for the enclave-bearing units, either a mafic recharge or a silicic entrant, it is still conclusive to say that magma mingling occurred.

Overall, the preservation of mafic enclaves in the silicic host pumice fragments, the disequilibrium features of the plagioclase phenocrysts, and the large compositional gap in the matrix glass and the pumice fragments can be used as evidence that magma mingling played an important role in the evolution of the silicic ash-flow sheets in

Nicaragua. The mingling of the magmas induced chemical and thermal instability in the chamber and thereby possibly triggering the eruption of the ignimbrites.

Model for the evolution of the Nicaraguan silicic ash-flow sheets

Chemical and mineralogical compositions within the seven silicic ash-flow sheets in Nicaragua suggest that they are the product of partial melting of previously emplaced arc-related igneous rocks and are independently generated. Figure 29 is a cartoon of the evolution of the Nicaraguan silicic ash-flow sheets. During stage 1, calc-alkaline magmas are produced by melting of the mantle wedge due to the fluids from the dehydrating, subducted Cocos plate. These magmas were produced by the same process as the modern arc lavas being enriched in Ba/La ratios due to the high fluid influx, which induces higher degrees of melting of the mantle wedge (low La/Yb). These magmas were emplaced at the base of the crust, approximately 15-20 km where amphibole would be stable. At stage 2, rising mafic magmas partially melts the amphibole-bearing previously emplaced igneous rocks to produce the silicic melt. The metasomatic characteristics of the mantle melt (i.e. high in fluid-mobile elements) and the presence of amphibole in the source rock ($Dy_N/Lu_N < 1$) could explain the enrichment of potassium in the silicic ignimbrites. As these pockets or blebs of silicic magmas ascend, they mingle with other rising and/or ponded mafic magmas (stage 3) at the magma chamber and/or during the ascent to the conduit.

Four possible cases during stage 3 in Figure 29 have been conceptualized and are shown in Figure 30 (Table 4). In case A, both the produced silicic magma and the intruding mafic magma ascend into the potential magma chamber without mingling. This scenario produces both the silicic and mafic pumice fragments in a single flow unit. For case B, some silicic magma stays behind in the chamber, and had ample time to mingle with intruding mafic magma and immediately erupts as mingled ash-flow sheets. These pumices are characterized by the presence of mafic enclaves within the silicic pumice fragments, with calcic plagioclase rims, and with matrix glass more mafic than whole pumice fragment (low SiO_2 with low K_2O and high MgO wt %; e.g. Las Maderas, Ostocal). In case C, newly formed and ascending blebs of silicic magmas intrude pockets of ponded mafic magma, mingles and gets erupted. Case C is distinguished with abrupt shifts of plagioclase composition from a more calcic core to a sodic rim (e.g. Las Sierras), and the glass composition in terms of SiO_2 and K_2O content is similar to the whole pumice fragment with distinct compositional gap (i.e. San Rafael, Coyol, Monte Galan). The process for these three scenarios was fast enough such that chemical and thermal equilibrium between the two magmas was not attained. The mingling of the magmas might have triggered the eruption and the immediate evacuation of the magma chamber caused caldera collapse. The fourth scenario, case D, involves an evolving intermediate magma that is continuously replenished from the source. All four cases could simultaneously occur but not in the same magma body.

Comparison with Central American Volcanic Arc

The silicic ash-flow sheets in Nicaragua are clearly enriched in Si_2O and K_2O compared to the low TiO_2 modern Nicaraguan arc lavas (Figure 13). It is important to note that the trace element variations (e.g. Hf/Th, Ba/La) of the silicic ignimbrites mimic the trace element variations in the modern arc (Figure 17). LILE and HFSE concentrations of the silicic ash-flow sheets are relatively higher than the modern Nicaraguan lavas (Figure 21) but the REE patterns are similar (Figure 18). Compared with the rest of CAVA lavas, which represent Quaternary front arc volcanism from Mexico-Guatemalan border down south to central Costa Rica, the Nicaraguan ash-flow sheets and modern arc lavas also show higher Ba/La ratio (Figure 17) indicating higher sediment influx (Carr et al., 1990). The presence of amphibole in the source rock of the silicic ignimbrites of Nicaragua manifested by Dy_N/Lu_N ratio <1, is similar to the Costa Rican ignimbrites (Figure 31; Hannah, 2000; Szymanski et al, 2002) although the range for Nicaragua is smaller compared to Costa Rica. The increasing La_N/Lu_N ratio with increasing Dy_N/Lu_N ratio suggests differentiation after emplacement of the melt. The Dy_N/Lu_N ratio differences result from different source rocks of the melts while the lower La_N/Lu_N ratio in the Nicaraguan silicic ash-flow sheets may be due to higher degrees of melting or from a source with lower La_N/Lu_N ratio, followed by crystal fractionation.

Conclusion

Seven chemically distinct ash-flow sheets were sampled in Nicaragua. Chemical and mineralogical variations among and within these silicic ash-flow sheets indicate that they cannot be explained by fractional crystallization alone but rather were produced by partial melting of previously emplaced arc-related igneous rock at depths where amphibole is stable (15-20 km). This arc-related source was partially melted by the injection of new mafic magma from the metasomatized mantle wedge generated via melting induced by fluids released from the dehydrating, subducted Cocos slab. Segregation and ascent of the partial melts produced the silicic ash-flow sheets. Continued production and ascent of both the silicic and mafic magmas into the chamber allowed mingling between the two magmas, and before even reaching compositional and thermal equilibrium were erupted as silicic ash-flow sheets with distinct chemical variations. REE pattern of the silicic ash-flow sheets mimic the REE trend of the modern arc lavas in Nicaragua indicating a genetic relationship. The enrichment in K_2O in the ignimbrites can be explained by the presence of amphibole in the source rock as manifested by the behavior of the MREE, in particular the Dy_N/Lu_N ratio of <1, coupled with the influence of sediment-derived fluids (high Ba/La).

APPENDIX A

Tables

Table 1
Sample Location

Sample	**Map Name (1:50,000)**	**UTM Coordinates**	
0107161a-e	Las Banderas	613626	1362313
010716-2a-h	Las Maderas	602120	1381700
010716-3a-e	Malpaisillo	550798	1397432
010718-1a-o	Malpaisillo	538300	1371500
010719-1a-g	Masaya	600063	1317781
020617-1a-p	Masaya	602582	1314027
020617-2a-h	Masaya	601042	1316332
020617-3a-e	Masaya	600414	1318125
020617-4a-e	Masaya	601695	1319418
020617-5a	Masaya	601695	1319418
020617-6a-f	Masaya	601851	1319296
020618-1a-d	Masaya	603668	1320690
020618-2a-c	Masaya	603668	1320690
020618-3a-j	Masaya	603354	1320701
020618-4a-j	Masaya	604046	1321759
020618-5a-g	Masaya	603288	1324370
020619-1a-w	San Rafael Del Sur	568404	1316865
020620-1a-n	Malpaisillo	537726	1394134
020620-2a-e	Malpaisillo	538520	1394320
020620-3a-e	Malpaisillo	539786	1394607
020620-4a-c	Malpaisillo	539786	1394607
020620-5a-h	Malpaisillo	539786	1394607
020620-6a-e	Malpaisillo	539940	1394639
020620-7a-n	Malpaisillo	544295	1395855
020620-8a-b	La Paz Centro	538624	1373036
020620-9a-k	La Paz Centro	540470	1372277
020620-10a-h	La Paz Centro	536651	1370009
020620-11a-n	La Paz Centro	536496	1367451
020622-1a-k	Las Playitas	602970	1384427
020622-2a	Las Playitas	602988	1384055
020622-2b-d	Las Playitas	602870	1383797
020622-3a-b	Las Playitas	602764	1383579
020622-4a-f	Las Maderas	602613	1383207
020622-5	Las Maderas	602150	1381805
020622-6a-g	Las Maderas	602150	1381805
020623-1a-d	Las Maderas	605021	1369890
020623-2a-g	Las Banderas	605021	1369890
020624-1a-n	Las Banderas	613695	1362284
020624-2a-k	Las Banderas	612602	1362213

Table 2
Apoyo Ash-flow Sheet

Sample	010719-1B	010719-1c	010719-1d	010719-1e	010719-1f	010719-1g	020617-1b	020617-1d
SiO_2	66.90	65.78	65.88	64.86	64.12	65.44	49.96	65.67
TiO_2	0.52	0.51	0.55	0.56	0.52	0.57	0.80	0.57
Al_2O_3	15.10	15.45	15.39	15.62	15.59	15.56	18.89	15.60
$Fe_2O_{3(T)}$	4.20	4.08	4.35	4.54	4.50	4.74	10.57	4.47
MnO	0.13	0.13	0.14	0.14	0.13	0.14	0.15	0.14
MgO	1.12	1.10	1.22	1.37	1.11	1.32	4.12	1.21
CaO	3.76	3.87	3.92	4.07	3.68	4.21	10.30	3.96
Na_2O	4.34	5.49	3.98	3.88	4.23	3.98	2.70	3.95
K_2O	2.09	2.04	2.02	1.89	1.99	1.91	0.49	1.99
P_2O_5	0.14	0.14	0.15	0.15	0.14	0.15	0.13	0.14
Totals	98.30	98.59	97.60	97.08	96.01	98.02	98.11	97.70
Cr (XRF)	bd	bd	bd	bd	bd	bd	bd	bd
Ni (XRF)	bd	bd	bd	bd	bd	bd	bd	bd
Cu (XRF)	bd	bd	bd	bd	bd	bd	bd	bd
Zn (XRF)	bd	bd	bd	bd	bd	bd	bd	bd
Rb	38.40	37.70	44.20	41.40	37.00	38.50	44.70	41.90
Sr	354.80	351.10	326.40	320.50	350.60	316.60	270.80	278.40
Zr	155.60	155.30	173.90	154.30	140.30	151.00	189.30	185.60
Ba	1433.68	1408.55	1565.81	1483.25	1351.77	1530.04	1596.08	1660.37
La	13.34	13.44	14.12	12.95	12.04	13.89	17.20	16.62
Ce	30.19	29.53	31.68	27.98	25.68	29.36	34.27	35.60
Pr	3.94	3.89	4.09	3.54	3.39	3.82	5.46	5.36
Nd	15.26	15.53	16.46	13.75	13.40	14.68	24.92	23.95
Sm	3.64	4.00	4.26	3.36	3.18	3.42	6.33	6.05
Eu	1.28	1.27	1.25	1.08	1.15	1.15	1.82	1.78
Gd	3.58	3.82	3.64	3.19	3.02	3.38	6.79	6.56
Tb	0.61	0.62	0.65	0.50	0.49	0.55	1.18	1.12
Y	20.66	23.13	22.97	18.54	17.55	19.11	45.18	42.35
Dy	3.49	3.66	3.64	2.88	2.86	2.90	7.24	6.87
Ho	0.75	0.83	0.86	0.64	0.61	0.65	1.54	1.48
Er	1.94	2.24	2.25	1.89	1.77	1.75	4.64	4.47
Yb	2.56	2.64	2.67	2.40	2.24	2.43	4.84	4.56
Lu	0.39	0.43	0.43	0.34	0.34	0.36	0.79	0.74
V	69.49	74.59	63.26	93.33	86.17	76.34	18.96	28.69
Cr	3.71	4.14	4.45	3.98	3.09	4.05	3.43	4.29
Nb	7.25	8.12	8.99	6.64	5.23	5.83	5.44	5.82
Hf	3.56	3.66	3.87	3.36	3.13	3.41	5.55	5.13
Ta	0.45	0.45	0.52	0.40	0.36	0.42	0.37	0.39
Pb	5.38	5.12	6.49	5.92	4.88	5.78	7.97	9.08
Th	2.83	2.94	3.09	3.08	2.79	3.10	3.79	3.65
U	3.11	3.17	3.52	3.31	2.71	3.16	3.01	3.38
Eu/Eu*	1.12	1.04	0.97	1.07	1.19	1.09	0.89	0.91
Distance	754.80	754.80	754.80	754.80	754.80	754.80	754.80	754.80

Table 2 continued
Apoyo Ash-flow Sheet

Sample	020617-1f	020617-1n	020617-1o	020617-2b	020617-2c	020617-2h	020617-3d	020617-4a
SiO_2	66.70	67.31	66.30	65.96	55.67	65.89	66.37	65.61
TiO_2	0.50	0.52	0.50	0.51	0.81	0.56	0.51	0.57
Al_2O_3	15.19	14.95	15.16	15.63	17.01	15.02	15.33	15.38
$Fe_2O_{3(T)}$	3.81	3.98	3.76	4.15	9.12	4.37	3.95	4.57
MnO	0.12	0.13	0.12	0.13	0.19	0.13	0.12	0.14
MgO	0.97	1.10	0.97	1.08	3.20	1.14	1.00	1.20
CaO	3.45	3.56	3.47	4.02	7.79	3.66	3.58	3.96
Na_2O	4.00	3.93	3.99	3.98	3.23	3.99	3.97	3.91
K_2O	2.17	2.16	2.16	1.99	1.06	2.07	2.10	1.99
P_2O_5	0.12	0.13	0.13	0.14	0.17	0.14	0.12	0.15
Totals	97.03	97.77	96.56	97.59	98.25	96.97	97.05	97.48
Cr (XRF)	bd	bd	bd	bd	bd	bd	bd	bd
Ni (XRF)	bd	bd	bd	bd	bd	bd	bd	bd
Cu (XRF)	bd	bd	bd	bd	bd	bd	bd	bd
Zn (XRF)	bd	bd	bd	bd	bd	bd	bd	bd
Rb	39.20	44.80	52.40	58.20	57.60	55.50	61.10	62.10
Sr	301.40	273.40	286.80	222.00	201.10	221.00	214.00	220.50
Zr	168.10	190.40	194.10	208.10	211.70	206.70	211.90	210.00
Ba	1456.80	1666.62	1760.40	1967.93	1942.43	1999.46	1990.14	2003.82
La	16.07	18.46	16.27	16.63	16.65	17.38	16.88	17.31
Ce	31.20	35.37	36.86	38.50	39.35	38.23	38.85	39.11
Pr	5.13	5.75	5.31	5.38	5.51	5.70	5.55	5.74
Nd	23.28	26.62	22.85	23.07	23.08	24.76	23.78	24.67
Sm	6.04	6.81	5.99	5.92	5.80	6.51	6.15	6.25
Eu	1.75	1.95	1.66	1.65	1.56	1.72	1.63	1.65
Gd	6.54	7.45	6.09	6.18	6.15	6.95	6.30	6.26
Tb	1.09	1.23	1.04	1.06	1.05	1.12	1.04	1.07
Y	42.46	46.77	38.41	39.86	40.01	41.58	39.48	39.52
Dy	6.87	7.62	6.28	6.44	6.49	6.78	6.63	6.43
Ho	1.51	1.64	1.35	1.39	1.41	1.47	1.42	1.41
Er	4.53	4.92	4.10	4.28	4.36	4.66	4.33	4.49
Yb	4.58	5.08	4.45	4.46	4.60	4.95	4.76	4.80
Lu	0.75	0.83	0.71	0.75	0.73	0.82	0.77	0.77
V	75.91	13.59	31.28	32.38	28.44	28.20	22.26	35.93
Cr	2.88	4.00	9.00	16.38	5.97	5.19	5.21	6.00
Nb	4.67	5.69	7.34	7.33	7.49	7.59	7.25	7.29
Hf	5.04	5.92	5.26	5.84	5.80	5.93	5.89	5.99
Ta	0.31	0.38	0.57	0.70	0.70	0.80	0.76	0.68
Pb	6.94	8.47	12.65	14.13	15.23	14.59	15.36	14.38
Th	3.50	3.97	3.31	3.58	3.66	3.65	3.62	3.74
U	2.63	3.18	3.57	4.07	4.11	4.13	4.02	4.01
Eu/Eu*	0.90	0.89	0.87	0.87	0.84	0.84	0.84	0.84
Distance	754.80	754.80	683.30	683.30	683.30	683.30	683.30	683.30

Table 2 continued
Apoyo Ash-flow Sheet

Sample	020617-4d	020617-4e	020617-5a	020617-6a	020617-6b	020617-6e	020617-6f	020618-1c
SiO_2	65.75	66.40	65.24	50.84	67.41	65.48	55.08	65.86
TiO_2	0.55	0.52	0.54	0.80	0.50	0.54	0.82	0.57
Al_2O_3	15.37	15.36	15.50	17.62	15.23	15.33	17.11	15.45
$Fe_2O_{3(T)}$	4.42	3.94	4.32	10.32	3.95	4.21	9.19	4.57
MnO	0.13	0.12	0.13	0.19	0.12	0.13	0.19	0.14
MgO	1.13	1.03	1.13	4.84	1.03	1.13	3.25	1.20
CaO	4.06	3.80	3.84	9.75	3.74	3.74	7.75	4.11
Na_2O	3.94	4.01	3.89	2.79	3.92	4.01	3.45	3.96
K_2O	1.98	2.04	2.02	0.73	2.13	2.08	1.00	1.97
P_2O_5	0.14	0.13	0.14	0.13	0.13	0.14	0.19	0.14
Totals	97.47	97.35	96.75	98.01	98.16	96.79	98.03	97.97
Cr (XRF)	bd	bd	bd	bd	bd	bd	bd	bd
Ni (XRF)	bd	bd	bd	bd	bd	bd	bd	bd
Cu (XRF)	bd	bd	bd	bd	bd	bd	bd	bd
Zn (XRF)	bd	bd	bd	bd	bd	bd	bd	bd
Rb	32.40	50.80	53.40	49.70	51.70	49.30	65.50	64.30
Sr	345.70	248.90	252.40	245.50	248.80	251.60	209.90	195.20
Zr	146.90	190.80	191.40	190.20	189.50	192.80	216.90	221.20
Ba	1385.55	1817.29	1811.91	1837.73	1880.30	1830.66	1893.77	1882.10
La	13.62	14.98	14.85	15.11	14.61	14.71	14.66	14.91
Ce	29.16	34.62	33.52	34.11	34.60	34.12	32.45	32.73
Pr	3.78	4.90	4.81	4.93	4.93	4.90	4.55	4.47
Nd	15.46	20.59	20.29	20.79	21.23	20.26	18.46	18.25
Sm	3.73	5.19	5.19	5.44	5.38	5.28	4.57	4.58
Eu	1.19	1.40	1.42	1.44	1.45	1.45	1.03	1.01
Gd	3.72	5.26	5.36	5.44	5.37	5.35	4.44	4.65
Tb	0.61	0.90	0.90	0.93	0.94	0.90	0.75	0.81
Y	23.77	36.98	37.28	37.47	35.69	36.83	31.52	32.90
Dy	3.66	5.58	5.59	5.66	5.69	5.54	4.67	4.85
Ho	0.69	1.10	1.13	1.11	1.26	1.14	0.93	0.99
Er	2.20	3.41	3.51	3.56	3.79	3.51	3.00	3.11
Yb	2.68	4.00	4.08	4.27	4.23	4.17	3.68	3.80
Lu	0.42	0.62	0.64	0.65	0.65	0.64	0.57	0.58
V	80.80	26.17	23.25	21.72	22.61	23.11	54.17	58.14
Cr	3.77	4.50	4.17	4.23	5.12	5.00	5.41	4.79
Nb	7.54	6.80	6.68	6.89	6.78	7.19	6.59	6.85
Hf	3.67	4.76	4.84	5.03	5.04	4.96	5.59	6.00
Ta	0.48	0.48	0.51	0.56	0.68	0.53	0.57	0.58
Pb	5.98	11.16	11.01	11.82	14.72	13.47	13.62	13.66
Th	2.14	1.93	2.00	2.05	2.92	2.07	2.72	2.81
U	1.80	1.90	1.91	1.97	3.82	2.20	2.50	2.41
Eu/Eu*	1.03	0.85	0.86	0.84	0.85	0.87	0.72	0.69
Distance	656.00	656.00	656.00	656.00	656.00	656.00	656.00	656.00

Table 2 continued
Apoyo Ash-flow Sheet

Sample	020618-2b	020618-3a	020618-3f	020618-3g	020618-3h	020618-4c	020618-4e	020618-4i
SiO_2	65.49	65.67	66.35	65.89	66.42	66.69	66.33	66.51
TiO_2	0.44	0.59	0.57	0.55	0.56	0.53	0.57	0.51
Al_2O_3	15.74	14.97	15.10	15.48	15.20	15.42	15.27	15.05
$Fe_2O_{3(T)}$	4.29	4.47	4.37	4.42	4.44	4.33	4.71	3.89
MnO	0.12	0.14	0.13	0.14	0.14	0.13	0.14	0.13
MgO	1.33	1.23	1.09	1.24	1.13	1.10	1.31	1.05
CaO	4.30	3.62	3.68	3.90	3.69	4.01	4.01	3.45
Na_2O	3.70	3.92	3.90	3.91	3.89	3.95	3.96	3.99
K_2O	1.95	2.12	2.16	2.08	2.11	2.07	2.06	2.27
P_2O_5	0.11	0.14	0.14	0.15	0.14	0.14	0.15	0.14
Totals	97.47	96.87	97.49	97.76	97.72	98.37	98.51	96.99
Cr (XRF)	bd	bd	bd	bd	bd	bd	bd	bd
Ni (XRF)	bd	bd	bd	bd	bd	bd	bd	bd
Cu (XRF)	bd	bd	bd	bd	bd	bd	bd	bd
Zn (XRF)	bd	bd	bd	bd	bd	bd	bd	bd
Rb	46.80	46.70	47.10	47.70	45.40	48.70	48.00	48.20
Sr	284.40	256.10	254.10	281.30	263.50	261.10	263.80	258.30
Zr	176.90	183.80	187.80	182.80	183.40	184.40	180.50	183.40
Ba	1792.58	1837.76	1940.93	1921.95	1889.50	1881.42	1897.91	1857.60
La	14.79	14.92	15.48	15.79	14.98	15.30	15.23	15.21
Ce	32.10	34.42	37.21	34.97	34.29	34.66	35.17	35.11
Pr	4.80	4.93	5.09	5.30	4.87	4.92	5.02	4.87
Nd	20.43	20.99	21.51	22.68	20.78	21.28	21.52	21.22
Sm	5.36	5.34	5.52	5.77	5.37	5.43	5.31	5.15
Eu	1.47	1.50	1.50	1.64	1.44	1.50	1.60	1.51
Gd	5.49	5.45	5.57	5.98	5.44	5.60	5.63	5.48
Tb	0.90	0.92	0.92	0.98	0.95	0.96	0.94	0.96
Y	36.21	37.74	36.30	37.07	35.85	37.03	35.89	35.86
Dy	5.35	5.46	5.82	5.90	5.70	5.87	5.70	5.69
Ho	1.07	1.13	1.26	1.26	1.25	1.29	1.28	1.26
Er	3.46	3.43	3.82	3.93	3.85	4.06	3.88	3.85
Yb	3.97	4.10	4.20	4.20	4.24	4.29	4.38	4.21
Lu	0.62	0.64	0.65	0.68	0.67	0.70	0.70	0.69
V	26.64	29.11	22.84	40.65	24.67	25.43	24.75	21.25
Cr	4.47	4.85	4.73	5.64	3.94	4.38	3.38	4.68
Nb	5.95	6.63	6.87	6.62	6.76	6.67	6.87	6.64
Hf	4.68	4.87	5.03	4.83	4.96	4.99	5.16	4.91
Ta	0.46	0.53	0.63	0.57	0.61	0.62	0.63	0.62
Pb	9.90	11.22	14.86	12.88	13.55	13.65	14.29	14.70
Th	1.91	2.02	3.03	2.81	2.93	2.92	2.92	3.01
U	1.78	1.90	3.92	3.48	3.61	3.70	3.66	3.64
Eu/Eu*	0.87	0.89	0.87	0.90	0.84	0.87	0.94	0.90
Distance	656.00	656.00	656.00	656.00	656.00	656.00	656.00	656.00

Table 2 continued
Apoyo Ash-flow Sheet

Sample	020618-5a	020618-5b	020618-5f
SiO_2	66.53	65.59	66.95
TiO_2	0.46	0.47	0.42
Al_2O_3	14.86	15.16	14.78
$Fe_2O_{3(T)}$	4.22	4.62	3.94
MnO	0.13	0.14	0.12
MgO	1.15	1.32	1.06
CaO	3.79	4.26	3.68
Na_2O	3.79	3.62	3.60
K_2O	2.11	1.95	2.17
P_2O_5	0.12	0.12	0.11
Totals	97.16	97.25	96.83
Cr (XRF)	bd	bd	bd
Ni (XRF)	bd	bd	bd
Cu (XRF)	bd	bd	bd
Zn (XRF)	bd	bd	bd
Rb	49.20	49.20	48.40
Sr	243.30	250.50	259.90
Zr	192.70	189.20	185.50
Ba	1892.57	1883.81	1860.38
La	15.11	15.32	15.54
Ce	35.13	35.74	35.90
Pr	5.00	4.98	5.13
Nd	21.30	21.31	21.59
Sm	5.38	5.34	5.38
Eu	1.46	1.54	1.57
Gd	5.61	5.44	5.64
Tb	0.96	0.93	0.96
Y	36.96	35.91	36.70
Dy	5.83	5.90	5.80
Ho	1.28	1.28	1.30
Er	3.87	3.95	3.90
Yb	4.26	4.33	4.18
Lu	0.69	0.69	0.70
V	25.63	26.13	22.14
Cr	5.09	5.18	4.97
Nb	7.17	6.82	6.78
Hf	5.16	5.08	5.12
Ta	0.80	0.62	0.68
Pb	14.64	13.86	15.30
Th	3.10	3.03	3.04
U	4.22	3.79	3.81
Eu/Eu*	0.85	0.91	0.91
Distance	683.30	683.30	683.30

Table 2 continued
Monte Galan Ash-flow Sheet

Sample	020620-10c	020620-10g	020620-10h	020620-11c	020620-11f	020620-11m	020620-8a	020620-8b
SiO_2	65.32	66.91	68.11	68.23	68.25	67.33	67.30	67.65
TiO_2	0.59	0.46	0.44	0.44	0.42	0.45	0.50	0.51
Al_2O_3	14.79	14.34	14.24	14.29	14.18	14.37	14.29	14.38
$Fe_2O_{3(T)}$	4.47	3.97	3.86	3.83	3.66	3.93	3.73	3.78
MnO	0.16	0.14	0.15	0.15	0.14	0.14	0.14	0.14
MgO	0.88	0.60	0.55	0.57	0.53	0.59	0.56	0.64
CaO	2.86	2.23	2.05	2.12	2.02	2.19	2.29	2.38
Na_2O	3.89	3.44	3.70	3.19	3.76	3.55	3.23	3.87
K_2O	2.85	3.23	3.22	3.67	3.46	3.47	3.22	2.92
P_2O_5	0.16	0.10	0.09	0.09	0.09	0.10	0.11	0.11
Totals	95.97	95.42	96.41	96.58	96.51	96.12	95.37	96.38
Cr (XRF)	bd	bd	bd	bd	bd	bd	bd	bd
Ni (XRF)	bd	bd	bd	bd	bd	bd	bd	bd
Cu (XRF)	bd	bd	bd	bd	bd	bd	bd	bd
Zn (XRF)	bd	bd	bd	bd	bd	bd	bd	bd
Rb	47.20	43.20	58.10	30.30	28.50	33.00	31.40	27.00
Sr	496.60	527.10	473.10	304.60	301.90	307.00	302.90	318.50
Zr	123.80	118.10	145.70	123.60	125.20	128.00	129.50	121.50
Ba	1095.24	1076.86	1347.55	991.64	957.90	965.16	991.05	829.65
La	12.12	16.17	26.70	11.46	11.16	11.30	11.51	14.23
Ce	25.24	26.44	35.38	22.35	21.66	22.35	22.09	21.22
Pr	3.78	5.00	7.36	3.73	3.65	3.73	3.72	4.22
Nd	16.75	22.27	33.11	17.66	17.47	17.85	18.15	20.35
Sm	4.27	5.56	8.30	4.99	4.96	5.03	5.20	5.61
Eu	1.21	1.60	2.25	1.50	1.49	1.49	1.52	1.67
Gd	4.12	5.51	8.14	5.79	5.51	5.63	5.84	6.65
Tb	0.67	0.88	1.38	1.01	0.98	0.98	1.00	1.18
Y	24.59	34.76	56.48	36.94	36.01	36.68	37.44	58.62
Dy	4.00	5.49	8.61	6.23	6.19	6.19	6.41	7.76
Ho	0.88	1.21	1.99	1.39	1.33	1.34	1.39	1.81
Er	2.32	3.50	5.51	4.24	3.92	4.02	4.15	5.24
Yb	2.40	3.55	5.67	4.19	4.01	3.94	4.11	5.18
Lu	0.37	0.53	0.89	0.69	0.65	0.66	0.69	0.80
V	130.44	147.40	101.98	252.92	244.26	252.01	244.12	243.00
Cr	3.80	3.30	3.31	4.82	4.80	4.85	4.72	5.09
Nb	2.90	2.82	3.48	4.11	4.07	4.11	4.25	3.87
Hf	3.53	3.35	4.27	4.26	4.24	4.36	4.46	3.57
Ta	0.21	0.21	0.26	0.28	0.27	0.27	0.29	0.26
Pb	4.41	4.54	5.86	4.57	4.80	4.80	4.97	4.03
Th	2.97	2.86	3.76	2.44	2.47	2.50	2.51	1.87
U	1.10	1.30	4.10	1.72	1.69	1.69	1.77	3.38
Eu/Eu*	0.92	0.94	0.87	0.90	0.91	0.90	0.89	0.88
Distance	675.00	675.00	675.00	675.00	675.00	675.00	717.00	717.00

Table 2 continued
Monte Galan Ash-flow Sheet

Sample	020620-9c	020620-9d	020620-9g
SiO_2	67.90	66.73	68.39
TiO_2	0.49	0.50	0.46
Al_2O_3	14.47	14.34	14.31
$Fe_2O_{3(T)}$	3.64	3.74	3.48
MnO	0.14	0.14	0.13
MgO	0.61	0.62	0.57
CaO	2.45	2.29	2.22
Na_2O	3.87	3.99	3.99
K_2O	2.89	2.93	3.05
P_2O_5	0.11	0.11	0.11
Totals	96.57	95.39	96.71
Cr (XRF)	bd	bd	bd
Ni (XRF)	bd	bd	bd
Cu (XRF)	bd	bd	bd
Zn (XRF)	bd	bd	bd
Rb	34.90	37.80	37.10
Sr	257.70	235.90	242.30
Zr	216.70	234.50	228.50
Ba	1297.15	1455.25	1355.48
La	14.69	17.46	15.81
Ce	34.00	42.17	36.52
Pr	5.10	5.98	5.43
Nd	23.31	27.05	24.52
Sm	6.37	7.15	6.75
Eu	1.81	2.05	1.88
Gd	7.00	7.73	7.12
Tb	1.23	1.36	1.24
Y	47.75		49.66
Dy	7.43		7.79
Ho	1.69		1.78
Er	4.76		5.16
Yb	4.98		5.21
Lu	0.76		0.81
V	59.84	68.88	39.63
Cr	4.46	6.94	4.44
Nb	8.31	8.95	8.52
Hf	5.53	6.31	5.88
Ta	0.51	0.57	0.57
Pb	6.31	7.25	6.91
Th	2.76	3.15	3.00
U	2.01	2.07	2.11
Eu/Eu*	0.86	0.88	0.86
Distance	717.00	717.00	717.00

Table 2 continued
Las Sierras Ash-flow Sheet

Sample	**010716-3B**	**010716-3C**	**010716-3D**	**010716-3E**	**010718-1b**	**010718-1c**	**010718-1e**	**010718-1f**
SiO_2	66.72	67.79	67.71	64.75	66.86	68.42	67.15	67.15
TiO_2	0.54	0.50	0.52	0.58	0.51	0.48	0.49	0.53
Al_2O_3	15.06	14.68	14.61	15.40	14.52	14.29	14.44	14.73
$Fe_2O_{3(T)}$	4.07	3.67	3.84	5.15	3.98	3.65	3.69	4.08
MnO	0.14	0.14	0.14	0.15	0.14	0.14	0.14	0.15
MgO	0.70	0.60	0.65	1.18	0.67	0.53	0.56	0.62
CaO	2.70	2.44	2.58	3.61	2.57	2.29	2.34	2.39
Na_2O	2.99	3.25	3.59	3.34	3.45	3.42	3.58	3.03
K_2O	2.82	3.05	2.95	2.40	2.92	3.03	2.96	2.85
P_2O_5	0.12	0.11	0.11	0.15	0.12	0.10	0.10	0.11
Totals	95.86	96.23	96.70	96.71	95.74	96.35	95.45	95.64
Cr (XRF)	21.50	1153.70	20.90	27.50	bd	bd	bd	bd
Ni (XRF)	21.30	148.50	bd	bd	bd	bd	bd	bd
Cu (XRF)	bd	46.10	bd	42.40	bd	24.90	bd	bd
Zn (XRF)	104.70	88.90	104.50	93.60	95.40	104.00	124.00	95.30
Rb	41.30	30.00	38.40	32.30	58.40	65.80	67.80	46.80
Sr	244.70	209.60	233.90	227.20	390.60	394.80	376.20	419.90
Zr	225.60	226.10	227.30	232.40	209.00	212.40	218.20	208.10
Ba	1383.10	949.20	1314.10	1328.30	1580.00	1700.00	1570.00	1960.00
La	16.51	14.72	16.47	13.96	21.10	21.70	22.00	21.90
Ce	37.66	35.06	34.76	33.68	39.20	40.50	39.50	38.70
Pr	5.61	4.94	5.41	4.70	6.56	6.72	6.87	6.52
Nd	24.72	22.72	24.68	21.65	29.20	29.00	30.90	29.60
Sm	6.57	6.20	6.76	5.83	7.05	7.15	7.56	7.27
Eu	1.87	1.65	1.71	1.58	1.75	1.77	1.83	1.77
Gd	6.67	6.60	6.97	5.90	6.78	6.90	7.39	6.89
Tb	1.14	1.11	1.21	0.98	1.16	1.15	1.26	1.13
Y	46.48	43.22	48.56	38.48	48.40	47.50	57.50	45.30
Dy	7.20	6.77	7.61	6.02	7.01	6.74	7.84	6.52
Ho	1.53	1.40	1.59	1.26	1.52	1.46	1.74	1.40
Er	4.59	4.26	4.86	3.82	4.40	4.28	5.22	4.00
Yb	5.02	4.63	5.11	4.22	4.78	4.51	5.95	3.94
Lu	0.74	0.68	0.77	0.61	0.77	0.70	0.98	0.64
V	12.60	78.32	31.95	37.23	68.50	75.30	64.50	77.10
Cr	14.37	10.93	10.36	16.47	11.30	13.20	11.30	11.00
Nb	9.95	8.27	9.20	9.16	5.43	5.62	5.48	5.10
Hf	4.41	5.30	5.60	5.06	5.26	4.90	5.51	5.43
Ta	0.46	0.48	0.49	0.48	0.30	0.32	0.33	0.31
Pb	7.32	5.17	4.72	5.00	8.64	10.40	8.22	8.83
Th	2.70	2.99	3.20	2.94	4.65	4.66	5.10	5.00
U	3.07	2.06	2.27	2.21	2.02	2.31	2.03	1.46
Eu/Eu*	0.90	0.83	0.79	0.86	0.80	0.80	0.77	0.80
Distance	717.00	717.00	717.00	717.00	675.00	675.00	675.00	675.00

Table 2 continued
Las Sierras Ash-flow Sheet

Sample	010718-1i	010718-1j	010718-1L	010718-1m	010718-1o	020620-1d	020620-1h	020620-1l
SiO_2	64.07	67.68	69.32	69.25	68.34	65.83	66.99	67.85
TiO_2	0.52	0.49	0.43	0.42	0.44	0.58	0.50	0.50
Al_2O_3	14.65	14.38	14.23	14.15	14.56	15.04	14.36	14.41
$Fe_2O_{3(T)}$	3.78	3.82	3.33	3.27	3.54	4.64	3.82	3.74
MnO	0.14	0.14	0.08	0.07	0.08	0.14	0.14	0.14
MgO	0.59	0.62	0.64	0.66	0.75	1.24	0.68	0.60
CaO	2.27	2.34	2.18	2.19	2.52	3.96	2.38	2.39
Na_2O	3.44	3.35	2.96	2.92	3.19	3.78	3.83	3.78
K_2O	2.77	3.02	3.85	3.89	3.56	2.07	3.00	3.03
P_2O_5	0.10	0.11	0.08	0.07	0.06	0.15	0.12	0.12
Totals	92.33	95.95	97.10	96.89	97.04	97.43	95.82	96.56
Cr (XRF)	1179.90	23.60	22.30	21.70	bd	bd	29.10	bd
Ni (XRF)	133.00	19.50	bd	bd	bd	bd	bd	bd
Cu (XRF)	20.90	16.50	46.10	bd	bd	bd	36.70	bd
Zn (XRF)	98.20	74.00	90.30	67.50	64.00	67.70	70.50	-
Rb	59.40	41.40	39.30	44.80	51.80	48.50	43.10	50.90
Sr	340.50	447.30	436.90	284.60	258.00	265.30	311.60	263.50
Zr	252.30	176.40	151.90	179.80	186.10	182.10	158.10	185.00
Ba	2140.00	1720.00	1680.00	1564.20	1591.40	1581.20	1538.00	1813.31
La	20.30	27.10	19.50	14.24	15.72	13.69	13.15	14.49
Ce	46.80	36.90	35.90	31.60	31.37	32.23	29.24	33.78
Pr	6.29	7.93	6.20	4.71	4.89	4.65	4.56	4.70
Nd	26.90	36.30	28.70	20.45	21.76	19.64	19.99	19.68
Sm	6.31	9.20	7.27	5.19	5.39	4.93	5.24	5.10
Eu	1.62	2.09	1.73	1.41	1.33	1.37	1.43	1.32
Gd	5.44	8.84	6.64	5.10	5.54	4.78	5.12	5.19
Tb	0.92	1.45	1.05	0.84	0.94	0.78	0.82	0.89
Y	33.60	61.10	36.00	32.94	38.21	31.73	32.29	35.82
Dy	5.12	8.36	5.86	5.13	5.75	4.94	4.95	5.63
Ho	1.09	1.82	1.18	1.05	1.21	1.02	1.07	1.08
Er	3.08	5.15	3.25	3.25	3.72	3.21	3.34	3.37
Yb	3.07	5.10	2.95	3.77	4.27	3.60	3.55	3.84
Lu	0.46	0.83	0.46	0.55	0.64	0.51	0.55	0.62
V	42.20	87.10	117.00	32.50	17.05	27.21	83.75	36.83
Cr	14.80	10.20	10.90	13.49	10.84	15.48	16.40	9.35
Nb	7.42	4.36	3.87	6.52	5.99	6.86	5.51	6.45
Hf	6.19	4.92	4.29	3.66	4.45	3.71	3.12	4.74
Ta	0.42	0.28	0.25	0.35	0.38	0.36	0.30	0.56
Pb	13.40	6.99	6.43	10.16	7.64	11.84	8.95	11.95
Th	5.82	4.47	3.94	2.42	2.74	2.40	2.08	2.01
U	2.46	1.11	1.07	2.89	2.56	3.21	2.71	2.09
Eu/Eu*	0.86	0.74	0.80	0.88	0.78	0.90	0.89	0.81
Distance	675.00	675.00	675.00	656.00	656.00	656.00	656.00	683.30

Table 2 continued
Las Sierras Ash-flow Sheet

Sample	**020620-1m**	**020620-2d**	**020620-2e**	**020620-3a**	**020620-3d**	**020620-4a**	**020620-5a**	**020620-5f**
SiO_2	68.00	68.56	67.99	69.09	68.96	66.48	67.35	67.40
TiO_2	0.48	0.48	0.49	0.40	0.42	0.52	0.52	0.50
Al_2O_3	14.34	14.33	14.38	14.03	13.86	14.87	14.29	14.71
$Fe_2O_{3(T)}$	3.62	3.69	3.72	3.26	3.42	3.95	3.91	3.69
MnO	0.14	0.13	0.14	0.09	0.09	0.14	0.14	0.14
MgO	0.58	0.58	0.59	0.63	0.66	0.63	0.68	0.56
CaO	2.34	2.37	2.35	2.38	2.30	2.59	2.48	2.38
Na_2O	3.62	3.77	3.86	3.05	3.00	3.31	3.64	3.65
K_2O	3.14	3.02	3.02	3.65	3.71	2.86	2.93	2.89
P_2O_5	0.11	0.11	0.11	0.09	0.10	0.12	0.12	0.11
Totals	96.37	97.04	96.65	96.67	96.52	95.47	96.06	96.03
Cr (XRF)	bd	bd	bd	bd	bd	bd	bd	bd
Ni (XRF)	bd	bd	bd	bd	bd	bd	bd	bd
Cu (XRF)	bd	bd	bd	bd	bd	bd	bd	bd
Zn (XRF)	bd	bd	bd	bd	bd	bd	bd	bd
Rb	52.20	54.10	52.80	57.10	50.40	65.50	65.70	61.20
Sr	244.90	251.80	252.20	250.10	244.60	197.00	195.90	217.30
Zr	191.70	192.20	192.20	188.90	190.70	223.30	223.40	215.70
Ba	1839.60	1895.17	1839.78	1851.54	1814.38	1882.63	1848.94	1852.88
La	14.59	15.14	15.40	14.75	14.73	15.13	14.75	14.99
Ce	34.70	35.26	36.21	34.31	33.90	34.93	33.46	32.36
Pr	4.87	4.98	5.21	4.84	4.79	4.91	4.64	4.75
Nd	20.20	20.77	22.07	20.12	20.35	19.85	18.56	19.09
Sm	5.32	5.17	5.56	5.36	5.16	4.95	4.50	4.82
Eu	1.37	1.35	1.45	1.36	1.35	1.05	0.96	1.11
Gd	5.31	5.39	5.65	5.17	5.22	4.73	4.39	4.67
Tb	0.90	0.89	0.92	0.87	0.89	0.80	0.78	0.79
Y	36.22	37.26	38.50	36.70	36.60	32.99	32.25	32.72
Dy	5.77	5.77	5.93	5.61	5.53	4.90	4.76	4.84
Ho	1.10	1.11	1.17	1.11	1.11	0.96	0.93	0.96
Er	3.50	3.57	3.58	3.54	3.39	2.97	2.98	3.10
Yb	4.11	4.21	4.12	4.02	4.05	3.68	3.53	3.83
Lu	0.64	0.65	0.67	0.62	0.61	0.57	0.57	0.59
V	24.45	28.83	31.56	29.18	29.19	65.02	59.91	68.28
Cr	10.27	12.76	10.46	12.81	9.38	13.58	12.95	12.29
Nb	7.17	6.78	7.01	7.35	6.66	7.31	6.80	7.26
Hf	5.04	4.86	4.93	4.90	4.85	5.80	5.61	5.70
Ta	0.65	0.59	0.56	0.55	0.55	0.63	0.65	0.56
Pb	13.66	12.68	12.11	12.07	10.89	13.19	12.13	11.61
Th	2.17	2.02	2.11	2.08	2.08	2.72	2.58	2.75
U	2.30	2.16	2.15	2.10	2.09	2.65	2.48	2.41
Eu/Eu*	0.82	0.83	0.84		0.83	0.69	0.67	0.74
Distance	683.30	683.30	683.30	683.30	683.30	683.30	683.30	683.30

Table 2 continued
Las Sierras Ash-flow Sheet

Sample	020620-6a	020620-6b	020620-7b	020620-7g	020620-7i
SiO_2	66.27	66.97	67.67	67.03	68.38
TiO_2	0.56	0.51	0.51	0.50	0.48
Al_2O_3	14.89	14.44	14.43	14.45	14.42
$Fe_2O_{3(T)}$	4.35	3.80	3.81	3.77	3.66
MnO	0.15	0.14	0.14	0.14	0.14
MgO	0.73	0.64	0.61	0.63	0.59
CaO	2.69	2.47	2.43	2.46	2.44
Na_2O	2.86	3.13	3.64	3.88	3.87
K_2O	2.80	2.81	2.90	2.77	2.87
P_2O_5	0.12	0.11	0.12	0.12	0.11
Totals	95.42	95.02	96.26	95.75	96.96
Cr (XRF)	20.60	bd	bd	bd	bd
Ni (XRF)	bd	bd	bd	bd	bd
Cu (XRF)	bd	bd	bd	bd	bd
Zn (XRF)	57.60	58.60	57.10	59.50	57.00
Rb	35.50	37.80	37.20	36.30	37.80
Sr	346.80	366.50	363.30	374.70	369.80
Zr	162.10	161.60	162.30	156.90	165.80
Ba	1450.00	1490.00	1460.00	1410.00	1500.00
La	14.70	15.00	15.10	14.20	14.80
Ce	29.80	30.80	30.60	29.10	30.50
Pr	4.22	4.24	4.29	4.03	4.25
Nd	17.10	17.30	17.30	16.60	17.20
Sm	3.97	4.17	4.05	3.88	3.95
Eu	1.34	1.38	1.35	1.31	1.37
Gd	3.78	3.74	3.77	3.68	3.70
Tb	0.61	0.63	0.62	0.59	0.61
Y	24.90	25.40	25.00	24.20	25.00
Dy	3.63	3.71	3.61	3.53	3.53
Ho	0.79	0.80	0.77	0.75	0.77
Er	2.36	2.32	2.33	2.24	2.27
Yb	2.72	2.74	2.68	2.59	2.66
Lu	0.41	0.42	0.41	0.40	0.41
V	79.90	84.70	86.00	92.90	85.00
Cr	15.70	17.50	18.40	16.00	18.30
Nb	8.09	8.35	8.20	8.01	8.65
Hf	3.62	3.58	3.62	3.41	3.73
Ta	0.44	0.45	0.46	0.41	0.46
Pb	6.90	7.38	7.14	6.58	7.03
Th	3.01	3.01	2.87	2.77	2.94
U	2.88	2.99	2.81	2.67	3.00
Eu/Eu*	1.11	1.09	1.10	1.11	1.14
Distance	754.80	754.80	754.80	754.80	754.80

Table 2 continued
San Rafael Ash-flow Sheet

Sample	**020619-1a**	**020619-1f**	**020619-1h**	**020619-1o**
SiO_2	64.15	63.42	62.35	63.25
TiO_2	0.77	0.79	0.83	0.76
Al_2O_3	13.93	13.97	14.25	13.93
$Fe_2O_{3(T)}$	7.85	7.97	8.58	7.53
MnO	0.21	0.20	0.21	0.20
MgO	0.85	0.87	1.47	0.78
CaO	3.49	3.43	4.40	3.27
Na_2O	4.04	4.00	4.04	4.08
K_2O	2.35	2.30	2.06	2.33
P_2O_5	0.21	0.21	0.22	0.21
Totals	97.85	97.16	98.41	96.34
Cr (XRF)	bd	bd	bd	bd
Ni (XRF)	bd	bd	bd	bd
Cu (XRF)	bd	bd	bd	bd
Zn (XRF)	bd	bd	bd	bd
Rb	50.20	49.70	65.20	63.80
Sr	251.10	237.40	546.10	560.80
Zr	189.20	195.90	157.70	158.80
Ba	1835.41	1901.51	1278.29	1311.05
La	15.47	15.97	23.00	21.62
Ce	35.36	36.65	40.94	40.14
Pr	5.13	5.27	6.67	6.14
Nd	21.67	22.33	30.10	27.25
Sm	5.59	5.82	6.96	6.47
Eu	1.58	1.52	1.85	1.76
Gd	5.85	5.75	6.66	6.25
Tb	0.96	0.98	0.99	0.95
Y	37.63	37.41	37.24	34.78
Dy	6.06	6.12	5.79	5.56
Ho	1.30	1.31	1.27	1.19
Er	4.05	3.92	3.47	3.29
Yb	4.40	4.37	3.42	3.39
Lu	0.70	0.72	0.55	0.51
V	21.37	18.83	191.24	195.23
Cr	4.53	5.06	8.09	8.10
Nb	6.46	6.93	3.97	4.15
Hf	5.28	5.31	4.26	4.29
Ta	0.62	0.63	0.26	0.30
Pb	14.46	15.36	3.98	4.76
Th	3.16	3.14	5.23	5.30
U	3.54	3.83	2.18	2.74
Eu/Eu*	0.89	0.83	0.90	0.91
Distance	683.30	683.30	670.00	670.00

Table 2 continued
Ostocal Ash-flow Sheet

Sample	010716-1A	010716-1B	010716-1C	010716-1D	020624-1c	020624-1e	020624-1h	020624-1i
SiO_2	65.61	62.82	65.69	64.88	64.33	64.11	65.49	65.55
TiO_2	0.67	0.73	0.67	0.70	0.76	0.70	0.69	0.67
Al_2O_3	14.04	14.74	14.09	14.71	14.22	14.07	13.99	13.92
$Fe_2O_{3(T)}$	6.21	6.90	6.18	6.16	6.60	6.44	6.29	6.23
MnO	0.20	0.22	0.19	0.24	0.20	0.26	0.19	0.20
MgO	0.80	2.43	1.04	1.39	1.16	1.03	0.91	0.80
CaO	3.14	2.96	2.93	2.94	3.46	2.99	3.05	3.05
Na_2O	4.20	2.32	3.75	3.05	3.86	3.93	3.94	4.18
K_2O	2.23	1.81	2.19	2.08	1.98	2.01	2.10	2.16
P_2O_5	0.22	0.29	0.16	0.14	0.20	0.16	0.16	0.16
Totals	97.32	95.22	96.89	96.29	96.77	95.70	96.81	96.92
Cr (XRF)	bd	bd	bd	bd	bd	bd	bd	bd
Ni (XRF)	bd	bd	bd	bd	bd	bd	bd	bd
Cu (XRF)	bd	bd	bd	bd	bd	bd	bd	bd
Zn (XRF)	bd	bd	bd	bd	bd	bd	bd	bd
Rb	40.50	34.90	13.80	36.70	37.40	18.30	34.30	37.30
Sr	352.20	357.90	468.60	340.90	342.60	473.20	359.40	356.20
Zr	158.70	154.20	58.10	160.30	161.10	81.70	149.10	140.30
Ba	1532.43	1490.94	562.40	1499.61	1501.87	790.32	1359.87	1415.06
La	13.95	13.72	7.19	14.01	14.58	9.54	13.08	12.44
Ce	32.29	30.56	14.33	31.19	31.54	19.10	29.03	26.00
Pr	4.02	3.95	2.28	4.16	4.11	2.87	3.89	3.39
Nd	15.96	15.78	10.81	15.81	16.83	13.22	15.57	13.39
Sm	3.84	3.99	2.98	3.81	3.86	3.43	3.86	3.31
Eu	1.30	1.31	1.06	1.31	1.36	1.26	1.26	1.12
Gd	3.71	3.78	3.13	3.84	4.10	3.52	3.81	3.09
Tb	0.62	0.61	0.52	0.60	0.66	0.57	0.61	0.49
Y	20.78	21.70	18.45	21.91	22.52	20.16	22.31	18.56
Dy	3.38	3.55	3.11	3.45	3.67	3.36	3.59	3.08
Ho	0.70	0.79	0.68	0.77	0.83	0.73	0.82	0.66
Er	2.00	2.15	1.89	2.02	2.34	2.07	2.22	1.81
Yb	2.59	2.57	1.96	2.67	2.90	2.15	2.51	2.35
Lu	0.40	0.41	0.29	0.40	0.43	0.34	0.40	0.36
V	68.84	75.85	301.31	60.69	70.27	235.21	72.58	80.09
Cr	3.75	3.77	21.97	5.38	4.80	5.57	4.07	6.38
Nb	7.78	7.27	2.25	7.44	7.75	3.14	7.88	5.85
Hf	3.47	3.62	1.67	3.65	3.90	2.20	3.52	3.05
Ta	0.49	0.52	0.14	0.49	0.51	0.21	0.43	0.36
Pb	6.19	6.00	1.75	5.62	5.56	2.44	5.10	4.94
Th	2.98	3.03	1.16	2.93	3.22	1.65	2.72	2.94
U	3.86	3.15	0.81	3.16	3.16	1.22	2.62	2.79
Eu/Eu*	1.09	1.08	1.12	1.12	1.12	1.18	1.06	1.13
Distance	754.80	754.80	754.80	754.80	754.80	754.80	754.80	754.80

Table 2 continued
Ostocal Ash-flow Sheet

Sample	020624-2c	020624-2d	020624-2g	020624-2h
SiO_2	65.12	64.50	64.59	65.18
TiO_2	0.68	0.69	0.70	0.68
Al_2O_3	13.60	13.91	14.09	13.89
$Fe_2O_{3(T)}$	6.35	6.23	6.43	6.32
MnO	0.23	0.20	0.48	0.28
MgO	0.84	0.88	0.86	0.88
CaO	4.04	3.13	3.20	3.08
Na_2O	3.97	4.01	4.00	3.93
K_2O	2.16	2.11	2.10	2.13
P_2O_5	0.43	0.18	0.20	0.17
Totals	97.42	95.84	96.65	96.54
Cr (XRF)	bd	bd	bd	bd
Ni (XRF)	bd	bd	bd	bd
Cu (XRF)	bd	bd	bd	bd
Zn (XRF)	bd	bd	bd	bd
Rb	42.00	41.70	38.30	38.50
Sr	325.60	334.60	355.00	340.30
Zr	166.40	163.20	157.50	160.60
Ba	1501.03	1509.96	1432.04	1459.40
La	14.67	14.36	13.63	13.91
Ce	31.58	31.63	29.84	30.35
Pr	4.26	4.12	4.05	4.00
Nd	17.12	17.18	15.83	16.34
Sm	4.32	4.24	3.87	3.81
Eu	1.34	1.33	1.36	1.33
Gd	4.12	3.99	3.97	4.01
Tb	0.68	0.64	0.63	0.63
Y	24.41	23.10	22.49	23.30
Dy	3.82	3.60	3.53	3.74
Ho	0.84	0.80	0.80	0.82
Er	2.43	2.10	2.13	2.19
Yb	2.81	2.68	2.71	2.79
Lu	0.45	0.41	0.40	0.42
V	73.30	71.25	70.24	70.31
Cr	4.26	3.95	3.87	3.72
Nb	8.51	7.69	7.41	7.29
Hf	3.63	3.72	3.52	3.61
Ta	0.47	0.49	0.49	0.49
Pb	5.41	5.64	5.62	5.20
Th	3.08	3.10	2.94	3.01
U	3.00	3.06	2.92	2.96
Eu/Eu*	1.01	1.04	1.13	1.12
Distance	754.80	754.80	754.80	754.80

Table 2 continued
Coyol Ash-flow Sheet

Sample	020622-1b	020622-1e	020622-1k	020622-2c	020622-2d	020622-3a	020622-3b	020622-3d
SiO_2	54.34	54.24	64.31	66.51	67.33	64.65	62.94	65.29
TiO_2	0.86	0.86	0.64	0.64	0.61	0.68	0.73	0.64
Al_2O_3	16.39	16.38	15.33	15.29	15.14	16.00	15.59	15.42
$Fe_2O_{3(T)}$	9.62	9.56	3.96	3.89	3.61	4.35	5.45	3.98
MnO	0.17	0.17	0.12	0.13	0.12	0.09	0.18	0.11
MgO	3.00	2.83	0.98	0.50	0.31	0.77	0.66	0.41
CaO	7.24	7.45	1.74	1.88	1.63	2.12	3.22	1.95
Na_2O	3.38	3.43	2.48	4.01	4.01	3.62	3.72	4.15
K_2O	1.99	2.03	5.43	5.21	5.27	4.17	4.19	4.72
P_2O_5	0.62	0.82	0.16	0.18	0.15	0.12	0.36	0.19
Totals	97.61	97.77	95.15	98.24	98.18	96.57	97.04	96.86
Cr (XRF)	bd	bd	bd	bd	bd	bd	bd	bd
Ni (XRF)	bd	bd	bd	bd	bd	bd	bd	bd
Cu (XRF)	bd	bd	bd	bd	bd	bd	bd	bd
Zn (XRF)	bd	bd	bd	bd	bd	bd	bd	bd
Rb	148.40	142.90	147.80	94.40	104.40	106.00	90.90	65.90
Sr	265.30	289.10	258.40	330.20	426.40	312.30	564.00	374.60
Zr	354.60	346.00	358.10	333.20	239.30	339.20	216.70	189.80
Ba	2219.12	2504.21	2488.68	2604.57	2324.41	2687.50	1962.11	1979.85
La	30.28	31.03	30.07	22.45	29.48	31.71	24.84	22.00
Ce	69.35	68.96	67.19	49.40	63.14	64.01	45.70	45.86
Pr	8.56	8.96	8.64	5.96	8.62	8.94	7.23	7.00
Nd	33.85	35.36	34.00	24.16	35.41	35.16	30.74	30.77
Sm	7.14	7.86	7.56	5.40	7.81	8.08	6.98	7.24
Eu	1.69	1.94	1.81	1.84	2.02	1.90	1.65	1.90
Gd	6.68	7.13	6.82	5.20	7.01	7.16	6.78	6.70
Tb	1.04	1.14	1.09	0.81	1.05	1.11	1.07	1.06
Y	35.96	39.87	39.42	26.64	30.40	37.46	37.37	39.56
Dy	5.94	6.58	6.41	4.66	5.58	6.49	6.10	6.23
Ho	1.28	1.40	1.39	1.00	1.12	1.35	1.30	1.42
Er	3.74	3.87	3.94	2.74	2.96	3.70	3.76	3.99
Yb	4.23	4.56	4.29	3.01	2.97	4.08	3.75	4.13
Lu	0.64	0.66	0.72	0.42	0.38	0.61	0.57	0.62
V	23.65	36.55	39.55	43.81	78.14	39.84	83.57	97.11
Cr	3.73	3.60	3.19	4.43	3.80	4.06	5.12	4.35
Nb	10.45	10.33	10.52	9.41	8.11	10.12	6.38	4.81
Hf	8.55	8.35	8.37	7.98	6.20	8.13	5.52	4.85
Ta	0.86	0.86	0.94	0.80	0.55	0.91	0.39	0.38
Pb	21.88	14.95	12.52	20.67	9.65	37.18	10.69	10.21
Th	12.04	11.73	12.02	11.11	8.89	11.37	7.73	4.71
U	5.86	5.81	5.93	4.36	3.09	5.05	2.80	2.18
Eu/Eu*	0.79	0.83	0.80	1.13	0.89	0.80	0.78	0.88
Distance	670.00	670.00	670.00	670.00	670.00	670.00	675.00	675.00

Table 2 continued
Las Maderas Ash-Flow Sheet

Sample	010716-2a	010716-2b	010716-2c	010716-2d	010716-2f	010716-2g	010716-2h	020622-4e
SiO_2	62.97	61.46	61.43	62.24	64.59	62.98	61.60	60.37
TiO_2	0.77	0.77	0.78	0.80	0.68	0.80	0.79	0.85
Al_2O_3	15.39	15.16	15.68	15.72	15.29	15.69	16.03	16.04
$Fe_2O_{3(T)}$	6.26	6.05	6.09	6.40	5.12	6.87	6.96	7.61
MnO	0.15	0.15	0.14	0.14	0.14	0.10	0.16	0.15
MgO	1.86	1.76	2.20	1.13	0.93	0.88	1.17	1.46
CaO	4.19	4.01	4.04	3.90	2.68	4.05	3.98	4.16
Na_2O	2.74	2.72	1.97	4.00	3.58	3.65	3.47	3.65
K_2O	3.81	4.00	4.14	2.84	3.55	2.97	2.57	2.28
P_2O_5	0.36	0.36	0.35	0.37	0.17	0.47	0.36	0.57
Totals	98.50	96.44	96.82	97.54	96.73	98.46	97.09	97.14
Cr (XRF)	20.00	bd	bd	bd	bd	bd	bd	bd
Ni (XRF)	bd	bd	bd	bd	bd	bd	bd	bd
Cu (XRF)	bd	bd	bd	bd	bd	bd	bd	bd
Zn (XRF)	61.20	bd	bd	bd	bd	bd	bd	bd
Rb	34.50	11.60	36.60	41.30	39.60	43.60	38.50	24.70
Sr	382.20	544.80	360.00	328.10	321.10	329.90	362.10	454.40
Zr	150.00	64.30	152.60	163.20	162.80	164.60	149.10	81.40
Ba	1350.00	725.78	1455.56	1542.28	1522.58	1614.74	1444.39	776.70
La	13.90	9.40	13.88	14.36	14.38	14.62	13.40	9.36
Ce	27.80	16.05	30.48	31.88	32.12	33.05	29.73	18.46
Pr	3.87	3.13	4.02	4.07	4.24	4.15	3.90	2.73
Nd	15.90	14.66	16.18	17.01	16.77	16.28	15.48	12.20
Sm	3.68	3.82	4.06	4.24	4.03	3.98	3.82	3.16
Eu	1.27	1.25	1.33	1.27	1.35	1.32	1.28	1.12
Gd	3.45	3.81	3.80	4.07	3.92	3.88	3.57	3.37
Tb	0.57	0.63	0.64	0.67	0.63	0.64	0.58	0.57
Y	24.10	23.66	23.78	24.73	22.67	22.22	20.73	20.22
Dy	3.50	3.86	3.90	3.81	3.76	3.60	3.36	3.32
Ho	0.76	0.80	0.83	0.92	0.82	0.84	0.75	0.75
Er	2.16	2.26	2.44	2.72	2.27	2.12	1.93	1.98
Yb	2.46	2.22	2.74	2.78	2.91	2.69	2.47	2.15
Lu	0.39	0.34	0.42	0.45	0.42	0.41	0.38	0.33
V	90.70	253.27	65.70	53.95	62.04	61.73	65.21	212.51
Cr	14.60	21.70	3.37	3.04	4.85	4.89	3.89	5.93
Nb	7.44	2.30	6.80	7.53	8.40	8.33	7.03	3.33
Hf	3.39	1.93	3.57	3.83	3.89	3.59	3.52	2.22
Ta	0.42	0.16	0.54	0.59	0.53	0.58	0.47	0.22
Pb	5.33	2.70	5.52	6.62	6.23	6.51	5.39	2.57
Th	2.70	1.25	2.79	2.94	3.11	3.03	2.80	1.61
U	2.36	0.56	2.40	2.63	3.68	3.81	2.98	1.42
Eu/Eu*	1.13	1.05	1.07	0.97	1.09	1.07	1.11	1.10
Distance	754.80	754.80	754.80	754.80	754.80	754.80	754.80	754.80

Table 2 continued
Las Maderas Ash-Flow Sheet

Sample	020622-5	020622-6a	020622-6f	020622-6g
SiO_2	63.25	57.79	54.62	56.68
TiO_2	0.70	0.80	0.78	0.81
Al_2O_3	15.71	18.05	18.81	16.84
$Fe_2O_{3(T)}$	5.39	8.14	8.02	7.64
MnO	0.13	0.12	0.12	0.14
MgO	1.34	1.92	2.00	1.65
CaO	4.03	6.75	7.36	7.54
Na_2O	2.87	2.80	3.02	3.31
K_2O	3.63	1.86	1.61	1.95
P_2O_5	0.20	0.27	0.35	1.79
Totals	97.25	98.50	96.69	98.35
Cr (XRF)	bd	bd	bd	bd
Ni (XRF)	bd	bd	bd	bd
Cu (XRF)	bd	bd	bd	bd
Zn (XRF)	bd	bd	bd	bd
Rb	40.50	40.30	35.70	34.50
Sr	327.20	336.90	351.00	357.40
Zr	162.20	162.70	152.80	149.80
Ba	1524.84	1551.40	1449.88	1418.90
La	13.99	13.82	13.99	13.60
Ce	32.29	31.72	31.05	29.83
Pr	4.07	4.04	4.17	3.96
Nd	16.14	15.59	16.64	15.76
Sm	3.92	3.84	3.98	3.62
Eu	1.29	1.27	1.32	1.22
Gd	3.70	3.83	3.97	3.75
Tb	0.60	0.59	0.64	0.60
Y	21.31	22.08	22.22	21.80
Dy	3.38	3.57	3.66	3.73
Ho	0.77	0.78	0.79	0.80
Er	2.09	2.18	2.13	2.09
Yb	2.58	2.69	2.49	2.57
Lu	0.39	0.38	0.39	0.41
V	74.04	68.29	82.77	70.94
Cr	4.14	3.82	3.92	2.89
Nb	7.74	7.99	7.42	6.80
Hf	3.62	3.56	3.60	3.56
Ta	0.48	0.50	0.46	0.47
Pb	6.15	6.09	5.42	5.09
Th	2.94	2.95	2.83	2.87
U	3.36	3.59	3.13	2.86
Eu/Eu*	1.08	1.09	1.07	1.08
Distance	754.80	754.80	754.80	754.80

Table 3
Matrix Glass Analysis

Apoyo Ash-flow Sheet

Sample	SiO_2	Al_2O_3	TiO_2	Fe_2O_3	MnO	MgO	CaO	Na_2O	K2O	Cl	Total
020617-1o-c5-gl1	81.16	15.40	0.33	2.04	0.13	0.46	2.10	3.07	2.65	0.23	107.35
020617-1o-c5-gl2	66.74	21.90	0.13	1.00	0.03	0.15	5.79	5.81	0.99	0.05	102.54
020617-2c-c3-gl1	62.97	24.26	0.12	1.17	bd	0.15	7.72	5.93	0.73	0.04	103.06
020617-2c-c3-gl2	58.93	26.47	0.07	0.87	bd	0.07	9.16	5.94	0.34	0.01	101.86
020617-5a-c7-gl2	76.17	13.34	0.31	1.20	0.03	0.23	1.49	4.19	2.46	0.16	99.41
020617-5a-c7-gl3	74.97	13.36	0.30	1.47	0.08	0.24	1.63	4.10	2.28	0.18	98.43

Monte Galan Ash-flow Sheet

Sample	SiO_2	Al_2O_3	TiO_2	Fe_2O_3	MnO	MgO	CaO	Na_2O	K2O	Cl	Total
020623-2e-c2-gl1	57.69	16.14	0.78	7.49	0.18	2.44	6.27	3.90	2.12	0.18	97.01
020623-2e-c3-gl1	58.89	16.14	0.75	7.13	0.14	2.12	5.36	3.57	2.10	0.19	96.20

Las Sierras Ash-flow Sheet

Sample	SiO_2	Al_2O_3	TiO_2	Fe_2O_3	MnO	MgO	CaO	Na_2O	K2O	Cl	Total
020620-3a-c2-gl1	71.25	14.30	0.33	3.06	0.09	0.36	1.73	3.87	3.29	0.28	98.30
020620-3a-c2-gl2	70.20	14.12	0.33	3.05	0.14	0.41	1.87	1.97	3.14	0.30	95.24
020620-6b-c3-gl1	66.31	15.06	0.32	2.72	0.17	1.48	4.52	4.68	2.37	0.59	97.62
020620-6b-c3-gl2	66.52	15.10	0.33	2.65	0.15	1.53	4.76	3.29	2.39	0.62	96.71

San Rafael Ash-flow Sheet

Sample	SiO_2	Al_2O_3	TiO_2	Fe_2O_3	MnO	MgO	CaO	Na_2O	K2O	Cl	Total
020619-1F-c2-gl1	66.88	13.96	0.49	6.54	0.27	0.62	2.97	4.42	2.31	0.20	98.46
020619-1F-c2-gl2	66.37	13.99	0.44	6.50	0.23	0.68	3.11	4.83	2.47	0.20	98.61
020619-1h-c2-gl2	63.84	15.02	0.61	7.87	0.25	1.70	4.65	3.77	1.79	0.16	99.50
020619-1h-c3-gl1	66.99	14.44	0.60	6.06	0.13	0.92	3.27	4.35	2.24	0.17	98.99

Table 3 continued
Matrix Glass Analysis

San Rafael Ash-flow Sheet melt inclusion

Sample	SiO_2	Al_2O_3	TiO_2	Fe_2O_3	MnO	MgO	CaO	Na_2O	K2O	Cl	Total
020619-1F-c2-g1-inc1	58.61	25.79	0.00	0.56	0.00	0.03	8.70	6.73	0.47	0.16	100.89
020619-1F-c2-pl1-inc1	57.65	24.86	0.00	0.48	0.00	0.05	8.15	6.75	1.09	0.50	99.02
020619-1F-c2-pl1-inc2	58.86	25.79	0.00	0.43	0.00	0.04	8.39	6.55	0.38	0.11	100.44

Ostocal Ash-flow Sheet

Sample	SiO_2	Al_2O_3	TiO_2	Fe_2O_3	MnO	MgO	CaO	Na_2O	K2O	Cl	Total
020624-1c-c3-gl2	67.36	13.96	0.50	6.08	0.21	0.79	3.03	4.28	2.05	0.24	98.27
020624-1c-c4-gl1	67.38	14.00	0.60	6.31	0.18	0.90	3.15	4.42	1.98	0.23	98.92
020624-1i-c1-gl1	67.24	14.02	0.53	5.97	0.18	0.74	3.13	4.33	2.12	0.22	98.27
020624-1i-c2-gl2	68.61	13.82	0.52	5.70	0.19	0.62	2.84	4.52	2.14	0.20	98.97
020624-2c-c1-gl3	65.56	13.61	0.43	5.72	0.22	0.60	2.66	4.42	2.36	0.14	95.58
020624-2c-c1-gl4	65.09	13.70	0.50	5.65	0.19	0.70	2.81	4.38	2.23	0.18	95.25

Ostocal Ash-flow Sheet mafic enclaves

Sample	SiO_2	Al_2O_3	TiO_2	Fe_2O_3	MnO	MgO	CaO	Na_2O	K2O	Cl	Total
020624-2c-c1-gl1	45.37	5.74	1.52	15.27	0.61	13.00	14.41	0.39	0.04	0.02	96.35
020624-2c-c1-gl2	58.46	12.81	0.83	9.09	0.34	4.06	8.83	4.47	0.39	0.17	99.29

Coyol Ash-flow Sheet

Sample	SiO_2	Al_2O_3	TiO_2	Fe_2O_3	MnO	MgO	CaO	Na_2O	K2O	Cl	Total
020622-2c-c1-gl1	66.59	16.38	0.47	3.46	0.15	0.73	2.60	5.51	2.71	0.02	98.61
020622-2c-gl2	72.00	16.46	0.47	2.55	0.13	0.28	1.27	4.03	6.88	0.02	104.06
020620-10g-c2-gl1	67.74	20.29	0.20	2.69	0.12	0.40	5.51	3.96	2.18	0.20	103.10
020620-10g-c2-gl2	54.95	26.27	0.08	1.39	bd	0.15	10.06	4.83	0.49	0.07	98.22
020620-10g-c3-gl1	60.02	24.02	0.02	0.39	bd	0.02	7.00	7.00	0.39	0.03	98.84
020620-8a-c4-gl2	71.45	13.93	0.31	2.68	0.10	0.39	1.81	4.31	2.73	0.24	97.71
020620-8a-c4-gl4	71.13	14.00	0.26	2.74	0.08	0.40	1.82	4.49	2.69	0.28	97.61

Table 3 continued
Matrix Glass Analysis

Coyol Ash-flow Sheet melt inclusion

Sample	SiO_2	Al_2O_3	TiO_2	Fe_2O_3	MnO	MgO	CaO	Na_2O	K2O	Cl	Total
020622-1e-c4-gl1-dev	58.30	17.20	0.52	7.64	0.25	3.23	7.45	3.74	2.11	0.10	100.44
020620-8a-c1-pl1-inc1	59.86	25.85	0.03	0.52	bd	0.04	7.72	6.79	0.33	0.00	101.15

Las Maderas Ash-flow Sheet

Sample	SiO_2	Al_2O_3	TiO_2	Fe_2O_3	MnO	MgO	CaO	Na_2O	K2O	Cl	Total
020622-4e-c1-gl1	67.77	15.01	0.48	2.81	0.12	0.56	1.55	3.23	5.79	0.13	97.33
020622-5-c1-out-gl2	68.11	14.36	0.35	1.94	0.06	0.45	1.53	3.19	5.16	0.26	95.15
020622-5-c2-gl1	70.65	13.95	0.40	1.96	0.09	0.48	1.68	3.80	4.13	0.25	97.14
020622-5-c4-gl1	69.58	13.76	0.35	1.97	0.10	0.45	1.58	2.61	5.63	0.16	96.04
020622-5-c5-gl4	69.05	13.64	0.37	1.77	0.10	0.35	1.44	2.84	4.73	0.26	94.30

Las Maderas Ash-flow Sheet mafic enclaves

Sample	SiO_2	Al_2O_3	TiO_2	Fe_2O_3	MnO	MgO	CaO	Na_2O	K2O	Cl	Total
020622-5-c5-gl3	62.22	13.19	0.32	2.79	0.03	0.55	1.19	1.54	4.26	0.23	86.08
020622-4e-c2-gl2	64.90	15.31	0.56	4.24	0.12	1.11	2.48	3.70	4.78	0.14	97.21
020622-5-c1-e-gl1	62.35	20.60	0.08	1.26	0.01	0.05	4.60	5.96	1.93	0.01	96.84
020622-5-c5-gl1	50.78	8.73	0.83	24.24	0.22	3.93	2.85	2.10	0.43	0.02	94.12
020622-5-c5-gl2	54.29	27.87	0.07	1.60	bd	0.15	10.49	5.19	0.35	bd	100.01

Table 3 continued
Plagioclase Analysis

Apoyo Ash-flow Sheet

Sample	**SiO_2**	**Al_2O_3**	**Fe_2O_3**	**CaO**	**Na_2O**	**K_2O**	**Total**	**An %**
020617-1o-c1-p1-c	55.38	28.34	0.41	10.40	5.51	0.17	100.22	53.16
020617-1o-c1-p1-int	54.84	28.82	0.46	10.83	5.16	0.17	100.28	28.39
020617-1o-c1-p1-r	71.55	15.29	2.06	2.60	2.13	2.28	95.91	48.48
020617-1o-c2-p1-c	56.39	28.14	0.47	9.95	5.72	0.19	100.85	53.88
020617-1o-c2-p1-int	55.10	29.21	0.43	11.18	5.22	0.11	101.25	46.23
020617-1o-c2-p1-r2	56.19	27.48	0.39	9.57	6.03	0.19	99.84	47.24
020617-1o-c2-p1-r1	56.26	28.34	0.43	9.78	5.92	0.18	100.91	60.64
020617-1o-c3-p1-c	52.94	29.88	0.43	12.51	4.41	0.12	100.28	48.52
020617-1o-c3-p1-int	55.85	28.02	0.47	9.92	5.67	0.22	100.16	45.44
020617-1o-c3-p1-r	56.98	27.66	0.37	9.30	6.04	0.20	100.57	63.13
020617-1o-c5-p1-c	52.51	30.23	0.59	12.76	4.07	0.07	100.24	33.96
020617-1o-c5-p1-r	68.58	19.22	1.32	4.79	4.19	1.45	99.53	93.16
020617-2c-c2-p1-c	44.77	35.39	0.51	18.90	0.73	0.06	100.37	90.86
020617-2c-c2-p1-int	45.33	34.83	0.77	18.82	1.04	0.01	100.79	69.90
020617-2c-c2-p1-r	50.72	31.12	0.53	14.47	3.36	0.13	100.32	48.70
020617-2c-c3-p1-c	56.28	27.83	0.34	10.00	5.69	0.20	100.35	43.51
020617-2c-c3-p1-int	57.67	26.59	0.37	8.83	6.16	0.27	99.88	52.84
020617-2c-c3-p1-r	55.14	27.91	0.46	10.68	5.16	0.16	99.51	57.96
020617-2c-c3-p2-mp	52.45	28.14	0.79	11.35	4.42	0.19	97.33	52.17
020617-5a-c3-p1-c	54.26	27.97	0.41	10.55	5.24	0.16	98.59	42.44
020617-5a-c3-p1-int	56.57	26.52	0.37	8.48	6.21	0.21	98.36	34.51
020617-5a-c3-p1-r	65.82	19.98	1.19	5.31	4.79	1.19	98.28	46.20
020617-5a-c7-p1-c	55.84	27.18	0.46	9.38	5.90	0.20	98.96	50.38
020617-5a-c7-p1-int	53.18	28.15	0.41	10.15	5.44	0.13	97.46	53.41
020617-5a-c7-p1-r	53.55	28.66	0.38	10.98	5.19	0.15	98.92	87.36
020617-6a-c2-p1-c	45.61	33.89	0.82	17.59	1.41	0.00	99.31	87.89
020617-6a-c2-p1-int	45.31	33.88	0.75	17.71	1.33	0.03	99.02	67.16
020617-6a-c2-p1-r	50.53	30.20	1.03	13.39	3.56	0.09	98.80	79.05
020617-6a-c2-p2-c	46.86	32.33	0.92	16.00	2.34	0.00	98.44	66.60
020617-6a-c2-p2-int	50.02	30.10	0.79	13.46	3.66	0.11	98.14	39.43
020617-6a-c2-p2-r	55.43	25.13	0.54	7.75	6.43	0.22	95.50	61.00
020617-6a-c3-p1-c	51.92	29.98	0.59	12.35	4.30	0.10	99.23	57.21
020617-6a-c3-p1-int	53.47	28.95	0.45	11.77	4.78	0.13	99.55	65.74
020617-6a-c3-p1-r	50.93	30.32	0.84	13.41	3.80	0.09	99.40	54.22

Monte Galan Ash-flow Sheet

Sample	**SiO_2**	**Al_2O_3**	**Fe_2O_3**	**CaO**	**Na_2O**	**K_2O**	**Total**	**An %**
020620-10g-c1-p1-c	59.19	25.30	0.31	7.26	7.04	0.39	99.49	33.18
020620-10g-c1-p1-int	59.27	25.40	0.34	7.09	7.17	0.29	99.57	36.53
020620-10g-c1-p1-r	60.32	26.10	0.37	6.98	7.49	0.42	101.69	70.03
020620-10g-c2-mp1-c	61.39	18.41	3.63	5.34	3.49	2.49	94.76	30.50
020620-10g-c2-mp1-r	50.14	30.59	1.33	13.98	3.23	0.11	99.38	35.69
020620-10g-c3-p1-c	60.39	24.72	0.30	6.28	7.64	0.41	99.74	22.95
020620-10g-c3-p1-int	59.85	25.77	0.33	7.39	7.10	0.39	100.83	39.34
020620-10g-c3-p1-r	68.66	18.84	1.89	3.62	5.39	2.02	100.43	37.37
020620-8a-c1-p1-c	57.25	25.98	0.46	7.98	6.56	0.37	98.60	25.61

Table 3 continued
Plagioclase Analysis

Monte Galan Ash-flow Sheet

Sample	SiO_2	Al_2O_3	Fe_2O_3	CaO	Na_2O	K_2O	Total	An %
020620-8a-c1-p1-int	57.67	25.54	0.41	7.57	6.79	0.35	98.32	54.42
020620-8a-c1-p1-r	63.81	18.26	1.53	3.91	5.19	1.66	94.37	43.00
020620-8a-c4-p1-c	54.05	28.82	0.44	11.18	5.07	0.16	99.71	25.60
020620-8a-c4-p1-int	56.62	26.47	0.39	8.80	6.31	0.20	98.79	76.79
020620-8a-c4-p1-r	65.29	17.26	1.72	3.64	4.70	1.75	94.36	82.54

Las Sierras Ash-flow Sheett

Sample	SiO_2	Al_2O_3	Fe_2O_3	CaO	Na_2O	K_2O	Total	An %
020620-3a-c3-p1-c	61.26	23.98	0.31	5.72	7.98	0.55	99.81	27.48
020620-3a-c3-p1-r	60.47	24.83	0.36	6.45	7.55	0.49	100.15	31.16
020620-3a-c4-p2-c	57.26	27.00	0.36	8.94	6.16	0.35	100.07	43.61
020620-3a-c4-p2-r	59.59	25.49	0.33	7.40	7.00	0.43	100.24	35.97
020620-3a-p1-c	60.51	24.28	0.29	6.37	7.66	0.48	99.59	30.62
020620-3a-p1-int	61.09	24.17	0.29	5.97	7.74	0.53	99.79	28.99
020620-3a-p1-r	58.89	25.04	0.29	7.15	7.09	0.37	98.82	35.01
020620-6b-c1-p2-c	48.39	32.69	0.76	16.16	2.36	0.06	100.41	78.83
020620-6b-c1-p2-int	53.13	29.42	0.69	12.41	4.26	0.12	100.03	61.25
020620-6b-c1-p2-r	54.07	28.82	0.41	11.77	4.81	0.10	99.98	57.15
020620-6b-c2-p1-c	49.97	31.33	0.46	14.72	3.15	0.08	99.71	71.71
020620-6b-c2-p1-int	54.42	28.70	0.40	11.21	5.05	0.16	99.94	54.56
020620-6b-c2-p1-r	58.20	27.12	0.47	8.87	6.32	0.20	101.19	43.16

San Rafael Ash-flow Sheet

Sample	SiO_2	Al_2O_3	Fe_2O_3	CaO	Na_2O	K_2O	Total	An %
020619-1F-c1-p1-c	54.87	28.70	0.51	11.01	5.03	0.17	100.29	46.23
020619-1F-c1-p1-int	56.68	26.98	0.53	9.44	5.86	0.31	99.82	23.84
020619-1F-c1-p1-r	66.29	14.00	6.59	3.02	3.68	2.52	96.10	37.09
020619-1F-c2-p1-c	59.21	25.36	0.46	7.51	6.78	0.40	99.72	45.56
020619-1F-c2-p1-int	57.26	27.14	0.53	9.26	5.92	0.30	100.41	43.01
020619-1F-c2-g1-r	57.65	26.21	0.53	8.84	6.27	0.31	99.81	41.89
020619-1F-c3-p1-c	57.71	25.98	0.66	8.51	6.31	0.33	99.49	46.11
020619-1F-c3-p1-r	56.62	26.95	0.60	9.32	5.84	0.28	99.60	42.96
020619-1h-c1-p1-c	56.70	26.87	0.45	8.77	6.24	0.30	99.32	45.50
020619-1h-c1-p1-int	55.83	27.09	0.53	9.17	5.90	0.25	98.77	44.27
020619-1h-c1-p1-r	55.09	26.19	0.53	8.94	5.94	0.27	96.95	44.18
020619-1h-c2-p1-c	57.06	26.88	0.57	9.05	6.13	0.26	99.95	39.59
020619-1h-c2-p1-r	57.88	19.01	5.50	6.94	4.16	1.04	94.52	38.50

Ostocal Ash-flow Sheet

Sample	SiO_2	Al_2O_3	Fe_2O_3	CaO	Na_2O	K_2O	Total	An %
020624-1c-c1-p1-c	57.96	25.45	0.36	7.54	6.79	0.31	98.41	37.34
020624-1c-c1-p1-int	56.27	26.52	0.42	8.62	6.11	0.25	98.20	43.16
020624-1c-c1-p1-r	55.23	26.46	0.43	8.96	5.99	0.16	97.24	44.82
020624-1c-c3-p1-c	54.53	27.63	0.44	10.03	5.58	0.17	98.39	49.31
020624-1c-c3-p1-int	54.62	27.80	0.41	10.34	5.49	0.15	98.82	50.55
020624-1c-c3-p1-r	57.68	25.63	1.05	8.32	5.86	0.39	98.93	42.91

Table 3 continued
Plagioclase Analysis

Ostocal Ash-flow Sheet

Sample	SiO_2	Al_2O_3	Fe_2O_3	CaO	Na_2O	K_2O	Total	An %
020624-1i-c1-mp1-c	56.53	24.89	2.07	8.54	5.38	0.37	97.77	45.61
020624-1i-c1-mp1-r	55.76	27.26	0.58	9.56	5.73	0.24	99.13	47.30
020624-1i-c1-p1-c	55.40	27.92	0.41	10.10	5.51	0.17	99.51	49.83
020624-1i-c1-p1-int	57.28	26.71	0.36	8.61	6.24	0.25	99.44	42.63
020624-1i-c1-p1-r	56.73	27.25	0.40	9.11	6.26	0.28	100.02	43.86
020624-1i-c3-p1-c	55.09	27.77	0.42	9.83	5.42	0.18	98.72	49.50
020624-1i-c3-p1-int	57.23	26.27	0.39	8.33	6.29	0.29	98.80	41.55
020624-1i-c3-p1-r	56.37	26.97	0.55	9.22	5.91	0.21	99.23	45.72
020624-2c-c1-p1-c	56.39	25.77	1.90	9.81	5.57	0.16	99.59	48.87
020624-2c-c1-p1-r	55.85	27.97	0.77	10.54	5.65	0.19	100.97	42.30
020624-2c-c1-p2-c	59.83	20.16	6.28	7.35	5.32	0.33	99.26	48.28
020624-2c-c1-p2-r	56.98	26.68	0.81	9.79	5.65	0.23	100.15	37.47
020624-2c-c3-p1-c	59.42	25.43	0.41	7.74	6.93	0.31	100.25	46.24
020624-2c-c3-p1-int	57.05	27.23	0.39	9.51	5.97	0.22	100.37	43.55
020624-2c-c3-p1-r	57.63	26.53	0.44	8.74	6.11	0.24	99.69	50.53

Coyol Ash-flow Sheet

Sample	SiO_2	Al_2O_3	Fe_2O_3	CaO	Na_2O	K_2O	Total	An %
020622-1e-c3-p1-c	57.32	25.93	0.47	8.01	6.23	0.80	98.77	38.93
020622-1e-c3-p1-int	57.50	25.98	0.42	7.69	6.32	0.71	98.62	61.60
020622-1e-c3-p1-r	57.20	26.19	0.41	7.88	6.33	0.76	98.76	59.81
020622-1e-c4-p1-c	52.16	28.77	1.14	12.48	4.01	0.44	99.01	61.50
020622-1e-c4-p1-int	52.37	28.89	1.19	11.85	4.11	0.44	98.85	44.34
020622-1e-c4-p1-r	51.98	29.31	1.08	12.54	4.08	0.40	99.38	44.73
020622-2c-c1-mp1-c	56.79	26.53	0.67	8.88	5.78	0.58	99.24	45.36
020622-2c-c1-mp1-int	56.56	26.59	0.70	9.05	5.77	0.63	99.29	43.70
020622-2c-c1-mp1-r	56.09	25.45	1.52	8.83	5.51	0.55	97.95	46.37
020622-2c-c2-p1-c	57.11	26.70	0.56	9.00	5.98	0.64	99.99	40.27
020622-2c-c2-p1-int	56.79	27.19	0.56	9.74	5.84	0.59	100.71	42.64
020622-2c-c2-p1-r	57.95	25.94	0.43	8.27	6.35	0.65	99.59	41.90
020622-2c-c4-p1-c	57.60	26.51	0.39	8.63	5.96	0.70	99.79	41.34
020622-2c-c4-p1-int	57.37	26.64	0.63	8.45	6.04	0.66	99.79	35.50
020622-2c-c4-p1-r	57.75	26.49	0.46	8.40	6.11	0.72	99.93	34.75

Table 3 continued
Plagioclase Analysis

Las Maderas Ash-flow Sheet

Sample	SiO_2	Al_2O_3	Fe_2O_3	CaO	Na_2O	K_2O	Total	An %
020622-4e-c1-p1-c	57.89	26.01	0.37	7.53	6.53	0.83	99.16	37.06
020622-4e-c1-p1-int	57.55	25.41	0.36	7.35	6.42	0.85	97.94	36.77
020622-4e-c1-p1-r	56.66	26.39	0.39	8.33	6.10	0.67	98.55	41.30
020622-4e-c2-p1-c	56.35	27.30	0.50	9.26	5.76	0.60	99.78	45.40
020622-4e-c2-p1-int	55.19	27.97	0.62	10.12	5.24	0.46	99.59	50.22
020622-4e-c2-p1-r	52.14	29.70	0.74	12.69	4.22	0.24	99.72	61.60
020622-5-c1-p1-c	54.59	28.44	0.77	11.00	4.91	0.34	100.04	54.23
020622-5-c1-p1-int	60.36	24.17	0.94	8.21	5.43	0.83	99.95	43.15
020622-5-c1-p1-r	63.44	22.45	0.84	5.89	6.50	0.94	100.06	31.39
020622-5-c2-p1-c	58.97	26.27	0.46	7.95	6.46	0.57	100.67	39.14
020622-5-c2-p1-r	57.39	26.83	0.59	9.16	5.94	0.40	100.32	44.94
020622-5-c3-p1-c	53.58	29.48	0.56	11.84	4.50	0.31	100.27	58.15
020622-5-c3-p1-int	53.07	30.03	0.71	12.41	4.21	0.23	100.66	61.16
020622-5-c3-p1-r	56.71	27.51	0.51	9.68	5.90	0.42	100.74	46.40
020622-5-c5-p1-c	54.48	28.33	1.27	11.42	4.91	0.25	100.66	55.43
020622-5-c5-p1-r	61.54	24.96	0.90	6.21	7.70	0.67	101.99	29.66
020622-5-c5-p2-c	52.73	29.52	1.04	12.86	4.11	0.18	100.44	62.68
020622-5-c5-p2-r	55.42	27.83	1.32	10.61	5.19	0.37	100.74	51.88
020622-5-c6-p1-c	56.81	27.29	0.54	9.37	5.77	0.46	100.24	46.05
020622-5-c6-p1-int	57.73	26.81	0.40	8.87	6.11	0.49	100.42	43.25
020622-5-c6-p1-r	56.71	27.44	0.51	9.56	5.65	0.47	100.33	46.99

Table 3 continued
Pyroxene Analysis

Ostocal Ash-flow Sheet

Sample	SiO_2	Al_2O3	TiO	Fe_2O_3	MnO	MgO	CaO	Na_2O	Total	Wo%	Mg#
020624-1c-c4-px1	51.70	2.36	0.38	9.41	0.61	15.29	21.17	0.38	101.30	9.60	46.08
020624-1i-c2-px 1	49.65	0.47	0.18	32.02	1.50	13.81	4.43	0.08	102.14	38.15	55.29
020624-2c-c1-px1	50.55	1.03	0.31	18.68	0.93	11.66	18.11	0.21	101.48	38.95	67.35
020624-2c-c1-px2	48.06	5.50	1.33	13.47	0.48	14.03	18.48	0.31	101.66	37.91	65.21
020624-2c-c2-px1	49.58	5.82	1.33	14.76	0.58	13.96	18.19	0.39	104.62	8.79	44.58
020624-2c-c3-px1	50.18	0.60	0.12	32.87	1.87	13.35	4.02	0.05	103.06	8.52	44.88

Coyol Ash-flow Sheet

Sample	SiO_2	Al_2O3	TiO	Fe_2O_3	MnO	MgO	CaO	Na_2O	Total	Wo%	Mg#
020622-1e-c1-px1-core	49.06	1.11	0.31	17.38	0.70	11.35	17.45	0.24	97.60	38.62	71.96
020622-1e-c1-px1-rim	50.18	2.55	0.38	11.97	0.37	15.50	18.86	0.33	100.14	39.88	74.02
020622-1e-c2-px2	50.49	1.58	0.44	13.65	0.93	14.13	17.95	0.37	99.53	38.03	67.23

Las Maderas Ash-flow Sheet

Sample	SiO_2	Al_2O3	TiO	Fe_2O_3	MnO	MgO	CaO	Na_2O	Total	Wo%	Mg#
020622-4e-c3-px1	49.86	3.09	0.46	10.83	0.25	15.58	19.42	0.32	99.80	3.28	63.82
020622-5-c4-px1	51.83	0.52	0.21	24.28	1.59	21.63	1.60	0.01	101.68	42.99	76.91
020622-5-c5-px 1	53.07	1.25	0.35	9.25	0.85	15.55	21.21	0.32	101.86	32.44	71.67
020622-5-c7-px1	52.32	1.61	0.38	13.41	0.44	17.13	15.96	0.23	101.48	43.16	76.30

Table 3 continued
Pyroxene Analysis

Apoyo Ash-flow Sheet

Sample	SiO_2	Al_2O3	TiO	Fe_2O_3	MnO	MgO	CaO	Na_2O	Total	Wo%	Mg#
020617-1o-c4-px1	50.40	0.47	0.23	32.80	1.79	13.48	3.89	0.05	103.12	42.91	75.12
020617-1o-c4-px2	52.98	1.34	0.28	9.87	0.62	15.04	20.93	0.30	101.36	42.53	75.96
020617-1o-c 5-px	51.98	1.46	0.22	9.55	0.70	15.24	20.65	0.31	100.10	2.39	66.30
020617-2c-c3-px-1	53.26	0.55	0.18	22.99	1.34	22.83	1.18	0.01	102.35	1.97	65.05
020617-2c-c3-px-2	52.90	1.13	0.15	23.96	1.98	22.52	0.97	0.04	103.64	42.35	70.36
020617-5a-c6-px1	48.19	5.73	1.03	11.61	0.36	13.91	20.20	0.30	101.34	42.85	74.63
020617-6a-c4-px1	51.40	1.20	0.25	9.99	0.61	14.84	20.74	0.30	99.33	43.75	74.67
020617-6a-c4-px2	51.25	1.26	0.28	9.93	0.54	14.77	21.40	0.32	99.76	40.73	77.44

Monte Galan Ash-flow Sheet

Sample	SiO_2	Al_2O3	TiO	Fe_2O_3	MnO	MgO	CaO	Na_2O	Total	Wo%	Mg#
020620-8a-c2-px1	51.45	0.90	0.25	13.92	0.87	13.23	19.72	0.34	100.69	41.17	65.32

Las Sierras Ash-flow Sheet

Sample	SiO_2	Al_2O3	TiO	Fe_2O_3	MnO	MgO	CaO	Na_2O	Total	Wo%	Mg#
020620-3a-c2-px2	45.30	7.99	1.25	15.30	0.27	11.57	18.83	0.38	100.90	41.23	59.98
020620-3a-c2-px3	45.05	8.43	1.68	13.83	0.25	11.81	19.94	0.40	101.38	43.28	62.84
020620-3a-c4-px1	51.76	1.47	0.40	27.19	1.52	20.21	1.67	0.03	104.26	3.41	59.55
020620-3a-c4-px3	51.87	0.47	0.22	28.68	1.76	19.35	1.53	0.03	103.90	3.14	57.20
020620-3a-px1	44.30	8.82	1.88	13.70	0.25	11.23	20.33	0.32	100.83	44.62	61.88
020620-6b-c1-px1	51.91	2.14	0.25	21.10	1.10	23.71	1.36	0.03	101.60	2.76	69.00
020620-6b-c3-px1	52.28	1.34	0.15	22.89	1.24	23.58	1.18	0.03	102.68	2.35	67.11
020620-6b-c4-px1	53.50	0.55	0.12	9.37	0.46	15.77	21.58	0.27	101.61	43.07	76.93
020620-6b-c4-px2	53.39	0.62	0.18	9.41	0.56	15.72	21.41	0.28	101.57	42.92	76.80

San Rafael Ash-flow Sheet

Sample	SiO_2	Al_2O3	TiO	Fe_2O_3	MnO	MgO	CaO	Na_2O	Total	Wo%	Mg#
020619-1h-c3-px1	50.14	2.76	0.29	9.39	0.21	16.27	20.09	0.17	99.31	38.50	52.78
020619-1h-c3-px2	49.99	1.24	0.33	19.43	0.82	10.97	18.10	0.21	101.08	38.40	56.39

Table 4: Four possible cases during stage 3 in Figure 27 (see Figure 28 for cartoon)

Possible Scenario at stage 3	Evidences	Representative Ash-flow Sheet
Case A: ascent of both silicic and mafic magma without mingling	- eruption of both silicic and mafic pumice fragments in a single ash-flow sheet	Apoyo Unit
Case B: mafic magma intrudes ponded silicic magma at the chamber and/or during ascent	- presence of mafic enclaves - calcic plagioclase rims - with matrix glass more mafic than whole pumice fragment (low SiO_2 with low K_2O and high MgO wt %).	Las Maderas and Ostocal Units
Case C: silicic magmas intrude pockets of ponded mafic magma	- abrupt shifts of plagioclase composition from a more calcic core to a sodic rim	Las Sierras Unit
	- glass composition in terms of SiO_2 and K_2O content is similar to the whole pumice fragment with distinct compositional gap	San Rafael, Coyol, Monte Galan
Case D: evolving intermediate magma that is continuously replenished from the source	- normal zonation in plagioclase - no mafic enclaves	Any unit

APPENDIX B

Figures

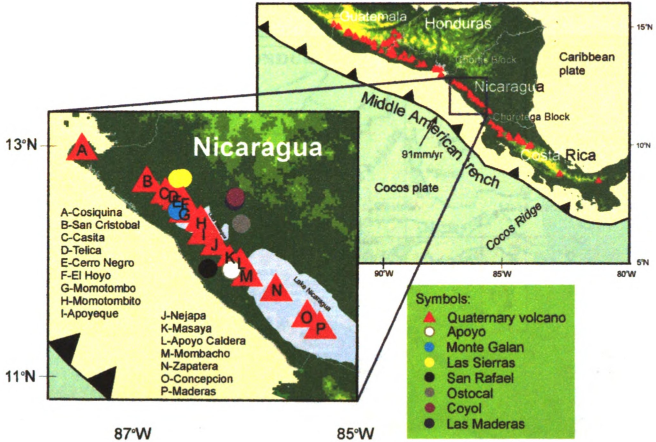

Figure 1. Map of study area: Circles represent sampling location of the 7 different ash-flow sheets; red triangles represent Quaternary volcanoes along the Central American Volcanic arc; numbers in mm/yr represent subduction rate of Cocos Plate under Nicaragua. Map modified from Roger et al. (2002).

Figure 2. Sampling location of the 7 different ash-flow sheets in red circles. APOYO: Apoyo, MONTE-:Monte Galan, LAS-SI: Las Sierras, SAN-RA:San Rafael, OSTOCA: Ostocal, COYOL: Coyol, LAS-MA: Las Maderas.

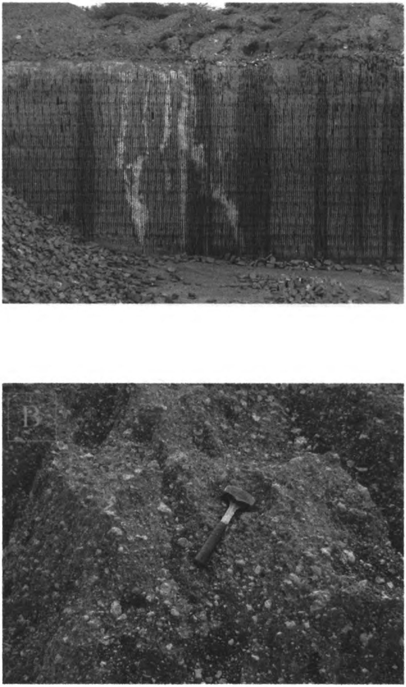

Figure 3. (A) Active quarry site for ignimbrite (Ostocal unit). (B) Typical pumice fragments of various sizes embedded in fine-ash matrix.


A


B

[illegible]

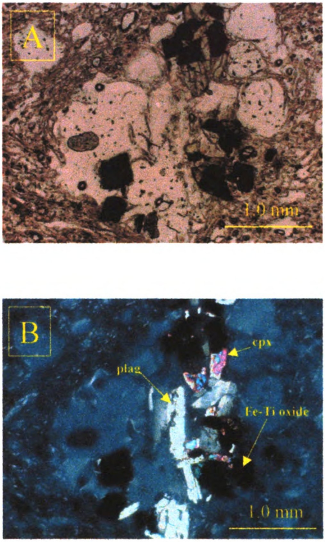

Figure 4. Photomicrograph of typical glomeroporphyritic texture in the pumice fragments. (A) Under plane polarized light and (B) under crossed polars. (Apoyo unit, sample # 020617-1o).

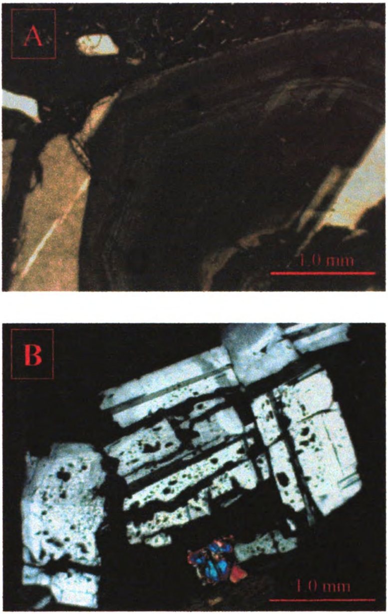

Figure 5. (A) Typical oscillatory zoning in plagioclase crystal (Apoyo unit, 020617-2c). (B) Typical sieve/resorved texture in plagioclase suggesting chemical dissolution (Las Sierras unit; 020620-6b).

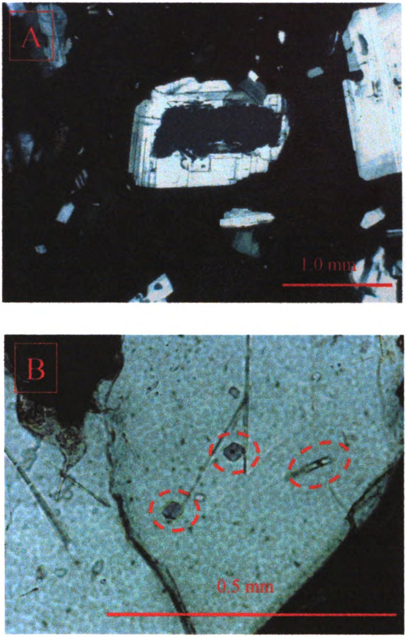

Figure 6. (A) Corroded plagioclase cores observed in Las Maderas unit (020622-5). (B) Melt inclusions found in plagioclase phenocryst San Rafael unit (020619-1f).

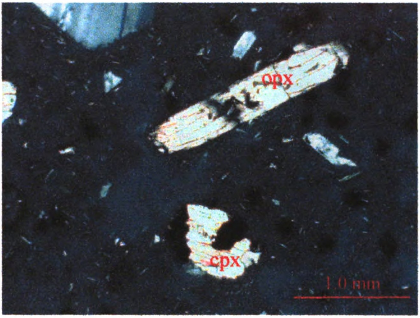

Figure 7. Phenocrysts of clinopyroxene and orthopyroxene (Apoyo unit, 020617-2c). Distinction between these 2 pyroxenes is difficult from petrography alone.


cpx
opx

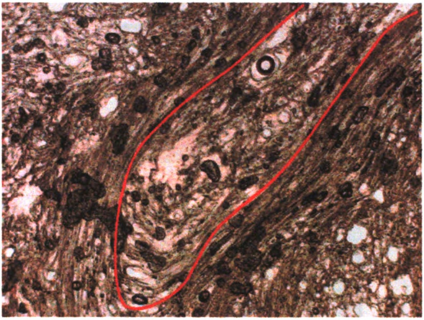

Figure 8. Banded pumice fragment observed under the microscope (Apoyo unit, 020618-5a).

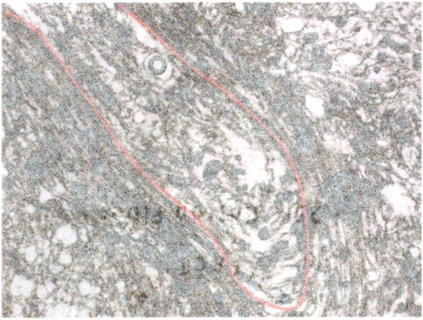

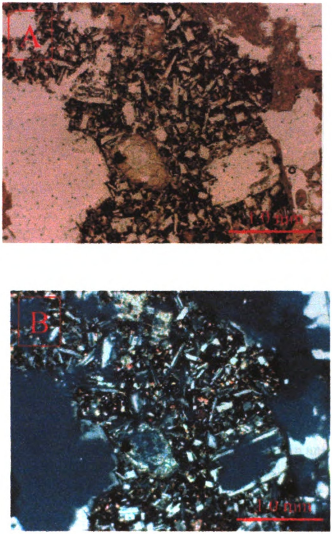

Figure 9. Mafic enclave within a silicic pumice fragment (Las Maderas 020622-5). (A) under plane polarized light and (B) under crossed polars. The phenocrysts content of the enclave are the same as the host pumice but are smaller in size.

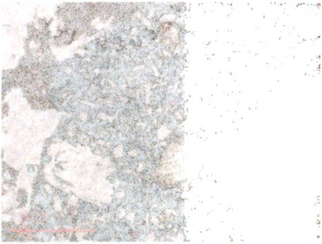

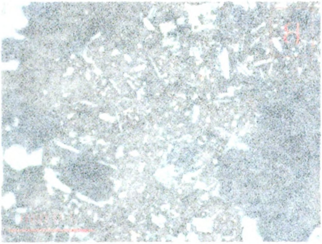
H

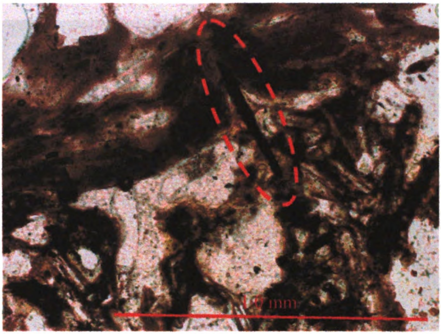

Figure 10. Intrusive-like feature of Fe-Ti oxide within an enclave into the silicic glass host (Ostocal unit, 0206 24-2c).

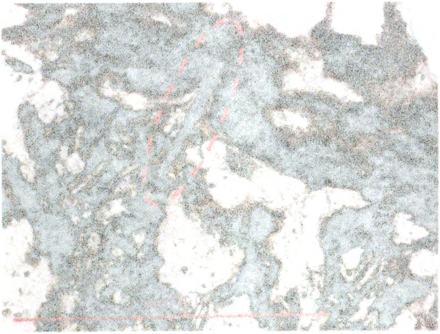

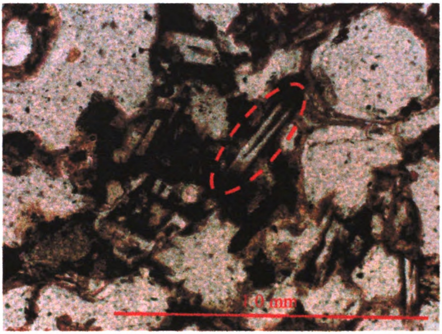

Figure 11. Dove-tail texture observed in plagioclase crystals within the enclave indicating quenched crystallization (Ostocal unit, 020624-2c).

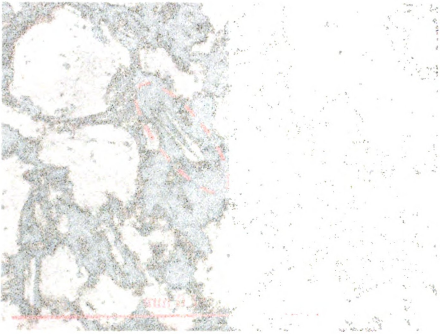

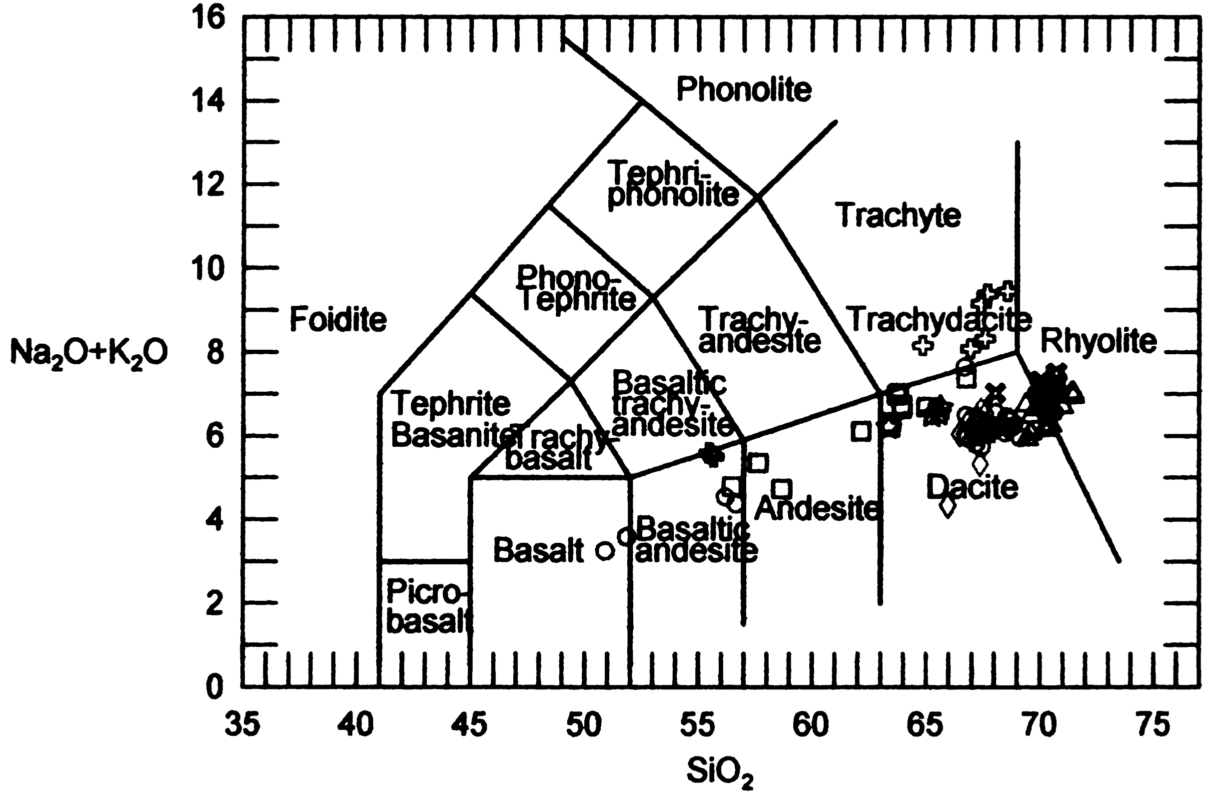

Figure 12. TAS classification diagram of LeBas et al. (19866) of pumice fragment from the seven recognized ash-flow sheets in southern Nicaragua: Apoyo ○, Monte Galan ✖, Las Sierras △, San Rafael ☆, Ostocal ◇, Coyol ✚, Las Maderas ☐. All samples plotted have been normalized to 100% volatile free.

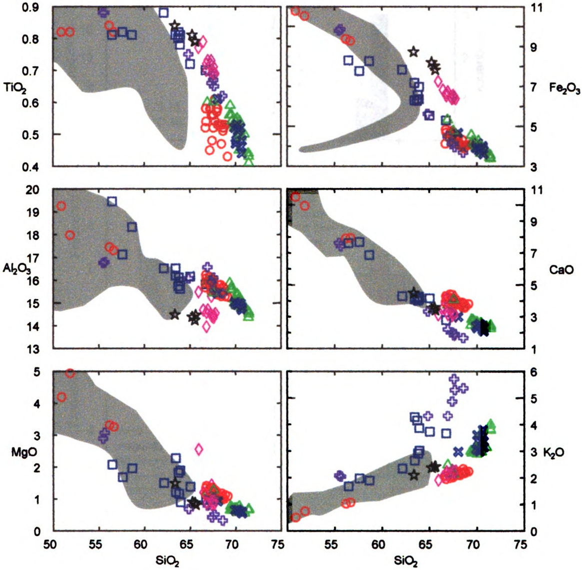

Figure 13. Major element variation against SiO_2 (wt. %) among ash-flow units in Nicaragua. Apoyo ○, Monte Galan ✖, Las Sierras △, San Rafael ☆, Ostocal ◇, Coyol ✣, Las Maderas □. Filled area represents trend for low TiO_2 Quaternary Nicaraguan lavas.

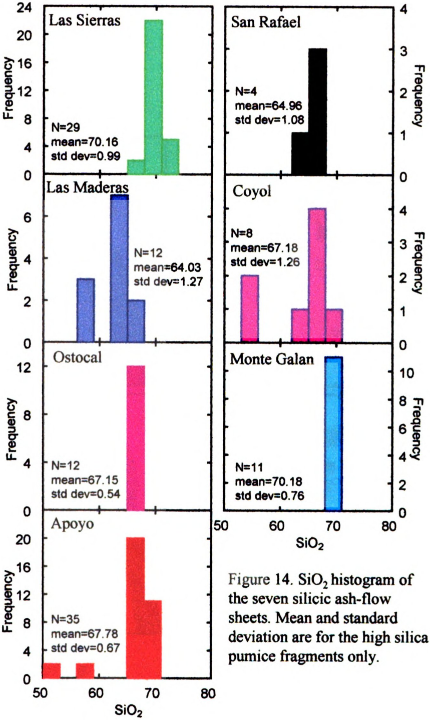

Figure 14. SiO_2 histogram of the seven silicic ash-flow sheets. Mean and standard deviation are for the high silica pumice fragments only.

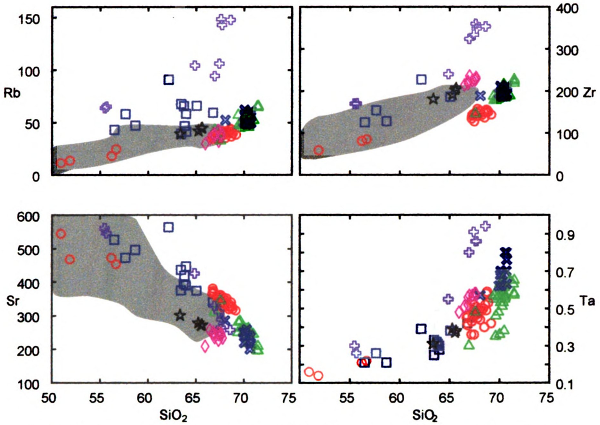

Figure 15. Trace element concentration of the silicic ash-flow sheets versus SiO$_2$ content. Apoyo ○, Monte Galan ✖, Las Sierras △, San Rafael ☆, Ostocal ◇, Coyol ✚, Las Maderas □. Filled area same as Figure 13. No Ta data for Nicaraguan lavas.

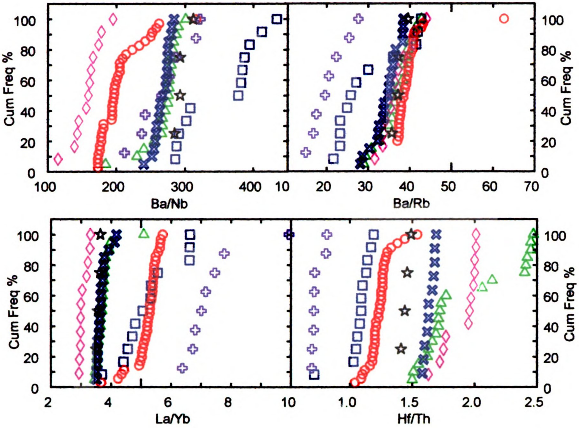

Figure 16 . Cumulative frequency curves (CFC) of trace element ratios of the seven ash-flow units. CFC's of most of the ash-flow sheets show little variation in the trace element ratio, but are distinct from each other. Others show distinct breaks, e.g. Ostocal, Las Sierraas (Hf/Th). Apoyo ○, Monte Galan ✖, Las Sierras △, San Rafael ☆, Ostocal ◇, Coyol ✚, Las Maderas □.

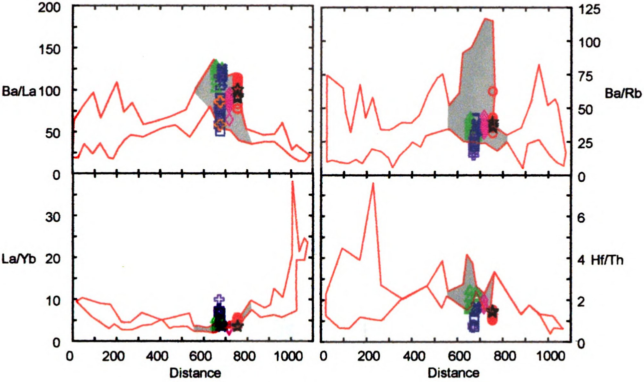

Figure 17. Trace element ratios plotted against distance along the Central American Volcanic Arc (CAVA) (starts in Mexico-Guatemala border, 0km and ends in central Costa Rica, ~1100 km). Red line represent all CAVA lavas and filled area represent Nicaraguan lavas. Apoyo ○, Monte Galan ✖ , Las Sierras △, San Rafael ☆ , Ostocal ◊ , Coyol ✚, Las Maderas □.

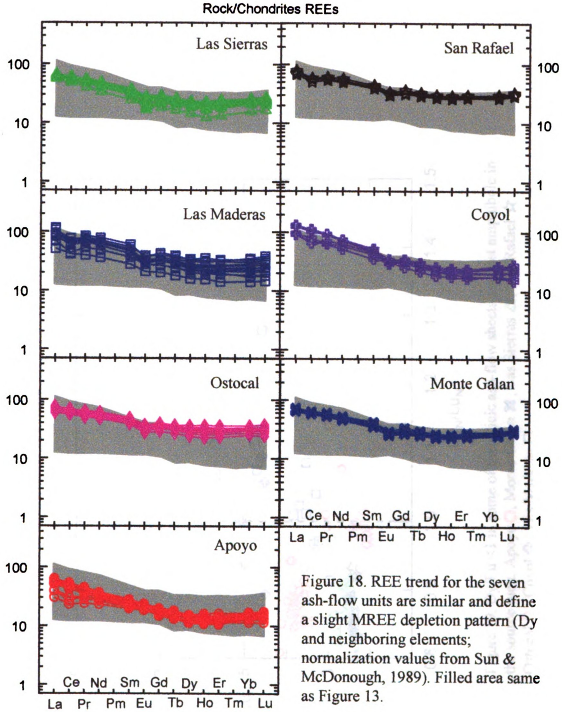

Figure 18. REE trend for the seven ash-flow units are similar and define a slight MREE depletion pattern (Dy and neighboring elements; normalization values from Sun & McDonough, 1989). Filled area same as Figure 13.

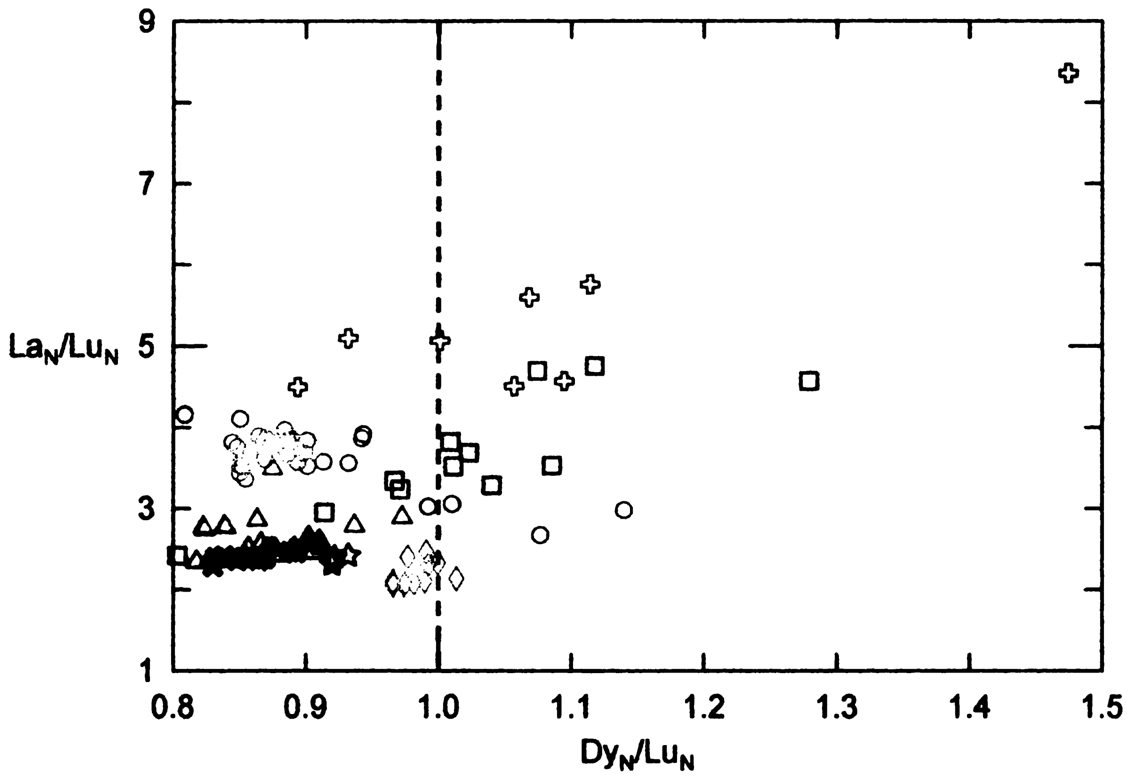

Figure 19. Dy/Lu <1 in some of the silicic ash-flow sheets suggest amphibole in the source melt. Apoyo ○, Monte Galan ✖, Las Sierras △, San Rafael ☆, Ostocal ◊, Coyol ✣, Las Maderas □.

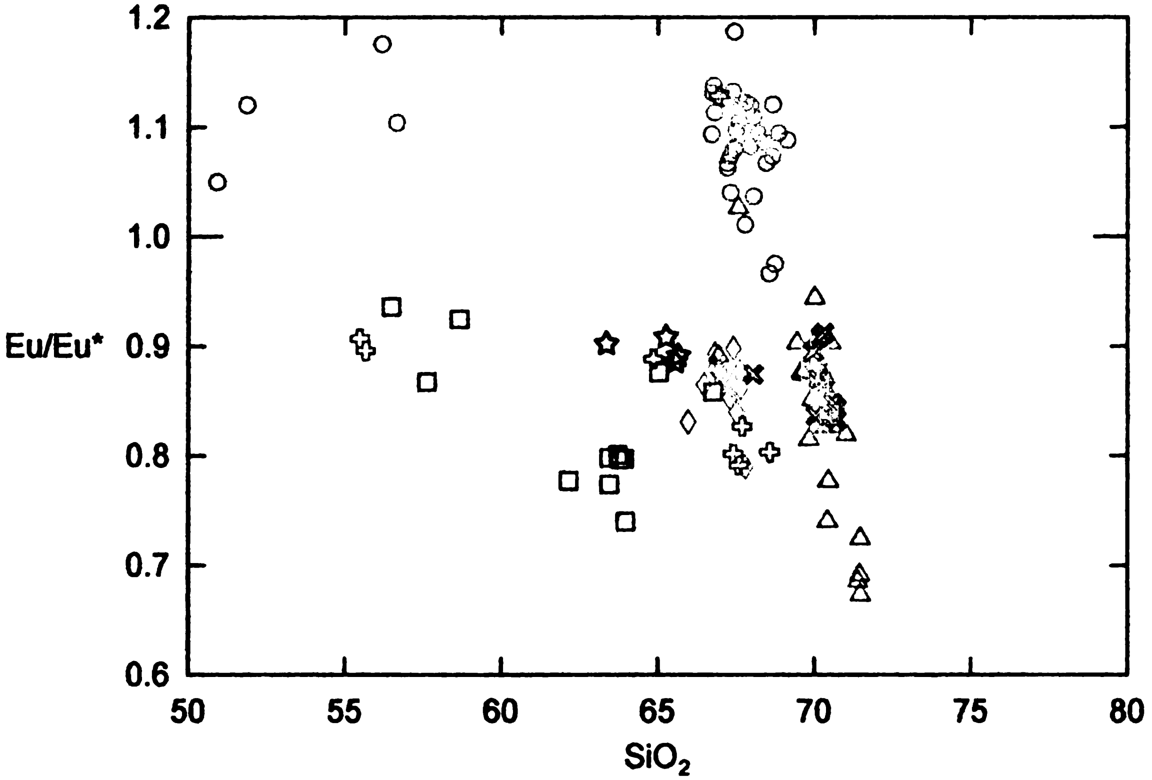

Figure 20. Calculated Eu anomaly for the seven silicic ash-flow sheets versus SiO_2 contents. Apoyo ○, Monte Galan ✖, Las Sierras △, San Rafael ✰, Ostocal ◇, Coyol ✙, Las Maderas □.

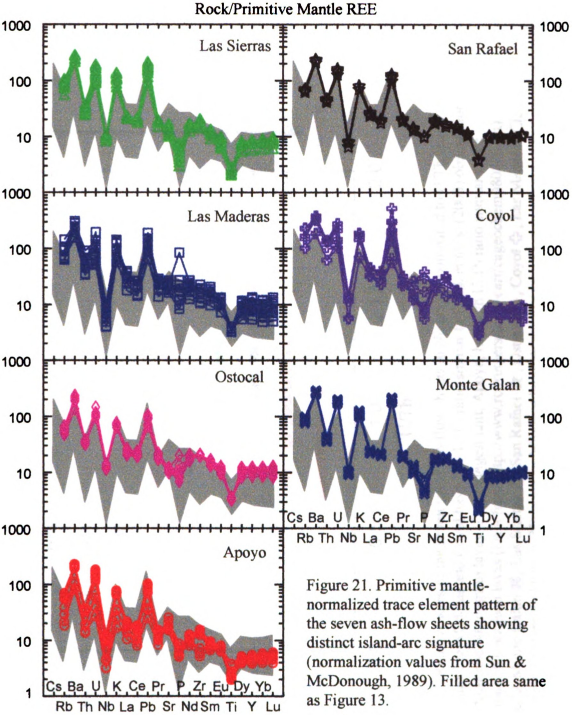

Figure 21. Primitive mantle-normalized trace element pattern of the seven ash-flow sheets showing distinct island-arc signature (normalization values from Sun & McDonough, 1989). Filled area same as Figure 13.

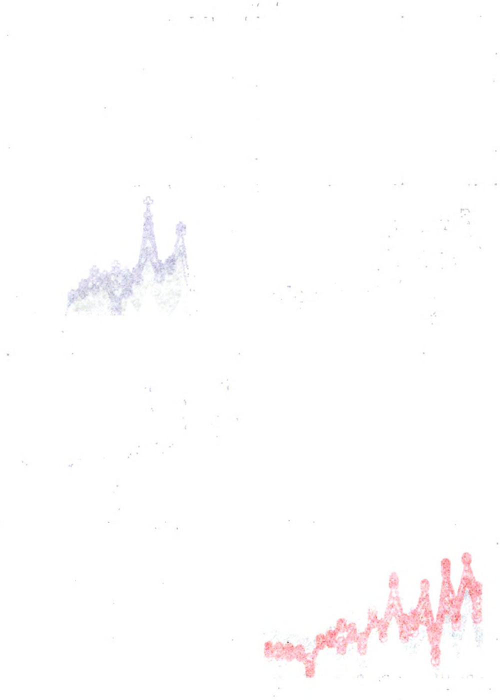

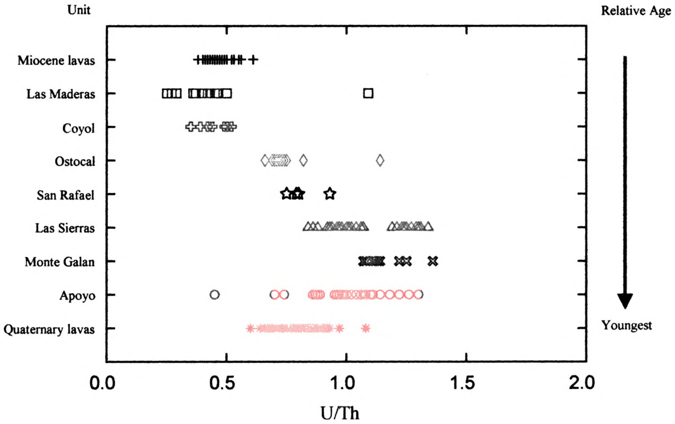

Figure 22. Relative ages of the seven silcic ash-flow sheets in Nicaragua compared to U/Th ratio. Older units Las Maderas and Coyol have low U/Th ratio similar to Plank et al.'s (2003) observation in the Miocene Nicaraguan lavas. The youngest unit, Apoyo, has high U/Th ratio similar to the Quaternary Nicaraguan lavas (Data from http://www.rci.rutgers.edu/~carr/cageochem080800.txt). Apoyo ○, Monte Galan ✖, Las Sierras △, San Rafael ☆, Ostocal ◇, Coyol ✚, Las Maderas □, Nicaraguan Quaternary lavas ✱, Nicaraguan Miocene lavas +.

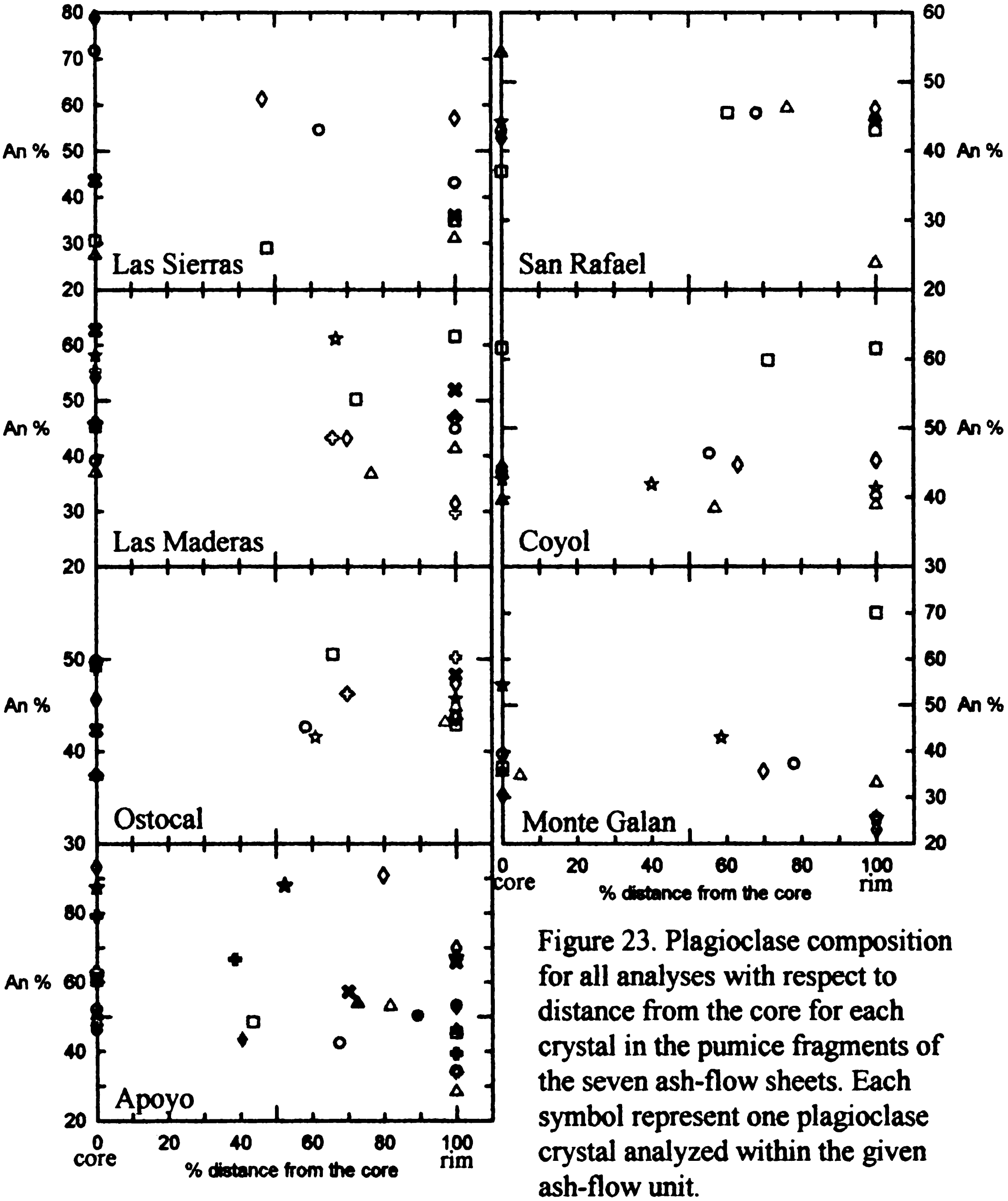

Figure 23. Plagioclase composition for all analyses with respect to distance from the core for each crystal in the pumice fragments of the seven ash-flow sheets. Each symbol represent one plagioclase crystal analyzed within the given ash-flow unit.

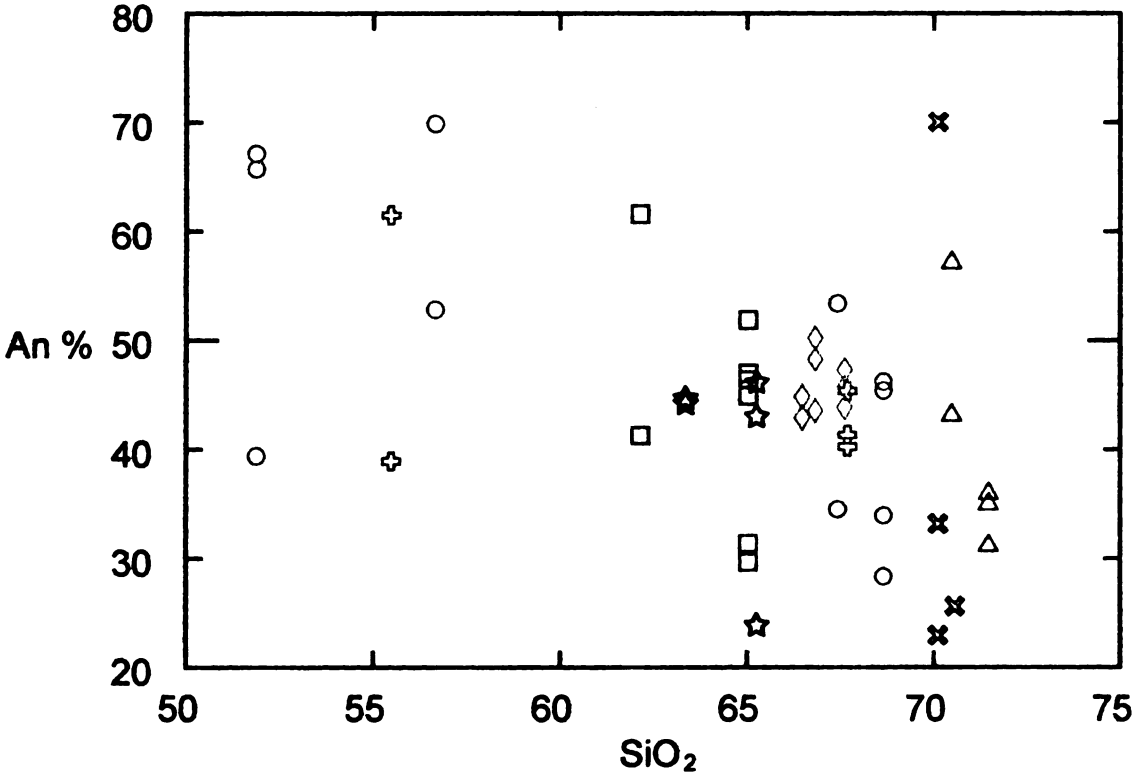

Figure 24. Anorthite content of plagioclase rims versus SiO_2 content of whole pumice fragment. Apoyo ○, Monte Galan ✖, Las Sierras △, San Rafael ✩, Ostocal ◇, Coyol ✙, Las Maderas □.

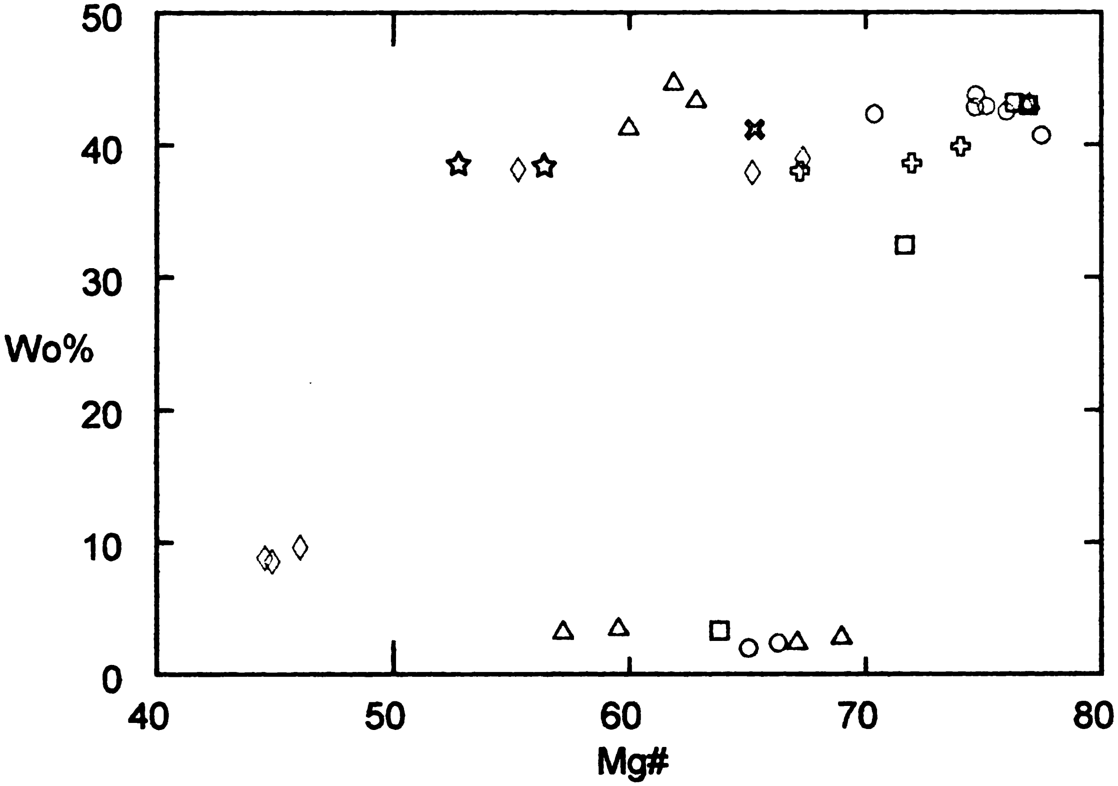

Figure 25. Analyzed pyroxenes of the silicic ash-flow sheets have a wide range of Mg#. Apoyo ○, Monte Galan ✖, Las Sierras △, San Rafael ☆, Ostocal ◇, Coyol ✚, Las Maderas □.

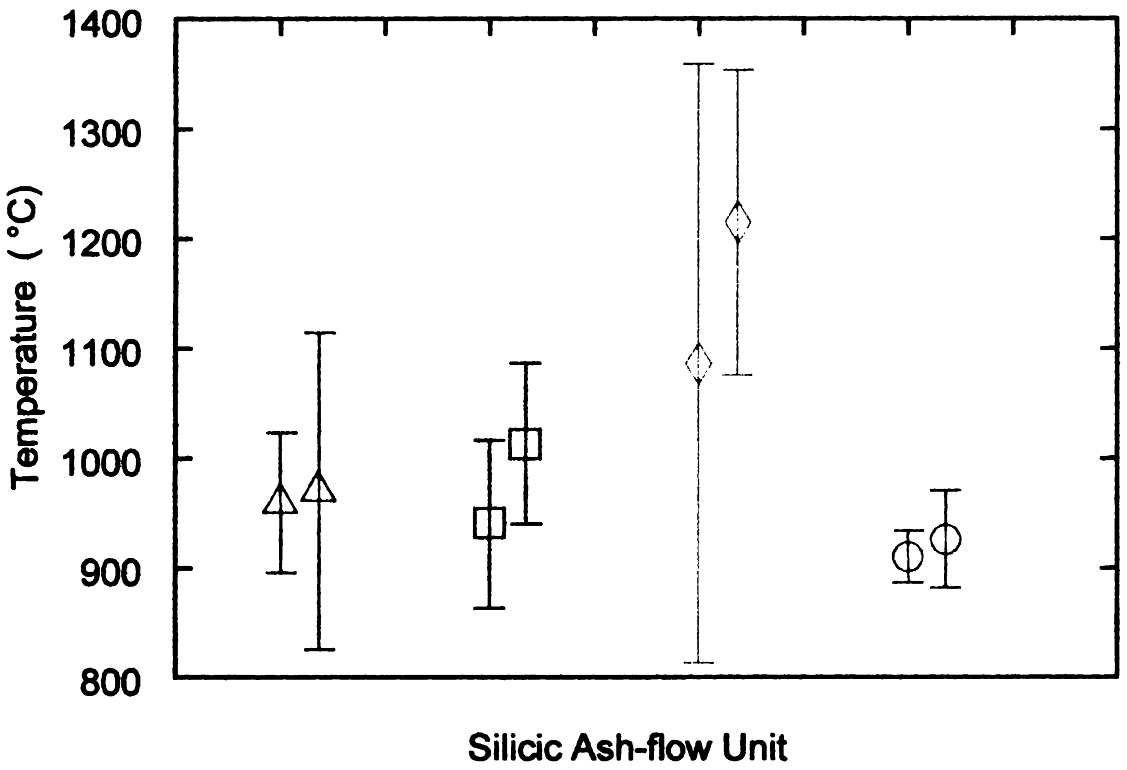

Figure 26. Calculated temperatures of Las Sierras, Las Maderas, Ostocal and Apoyo units using the 2-pyroxene program QUILF version 6 (Andersen et al., 1993). Other units do not have opx or were not analyzed. Apoyo ○, Las Sierras △, Ostocal ◇, Las Maderas □.

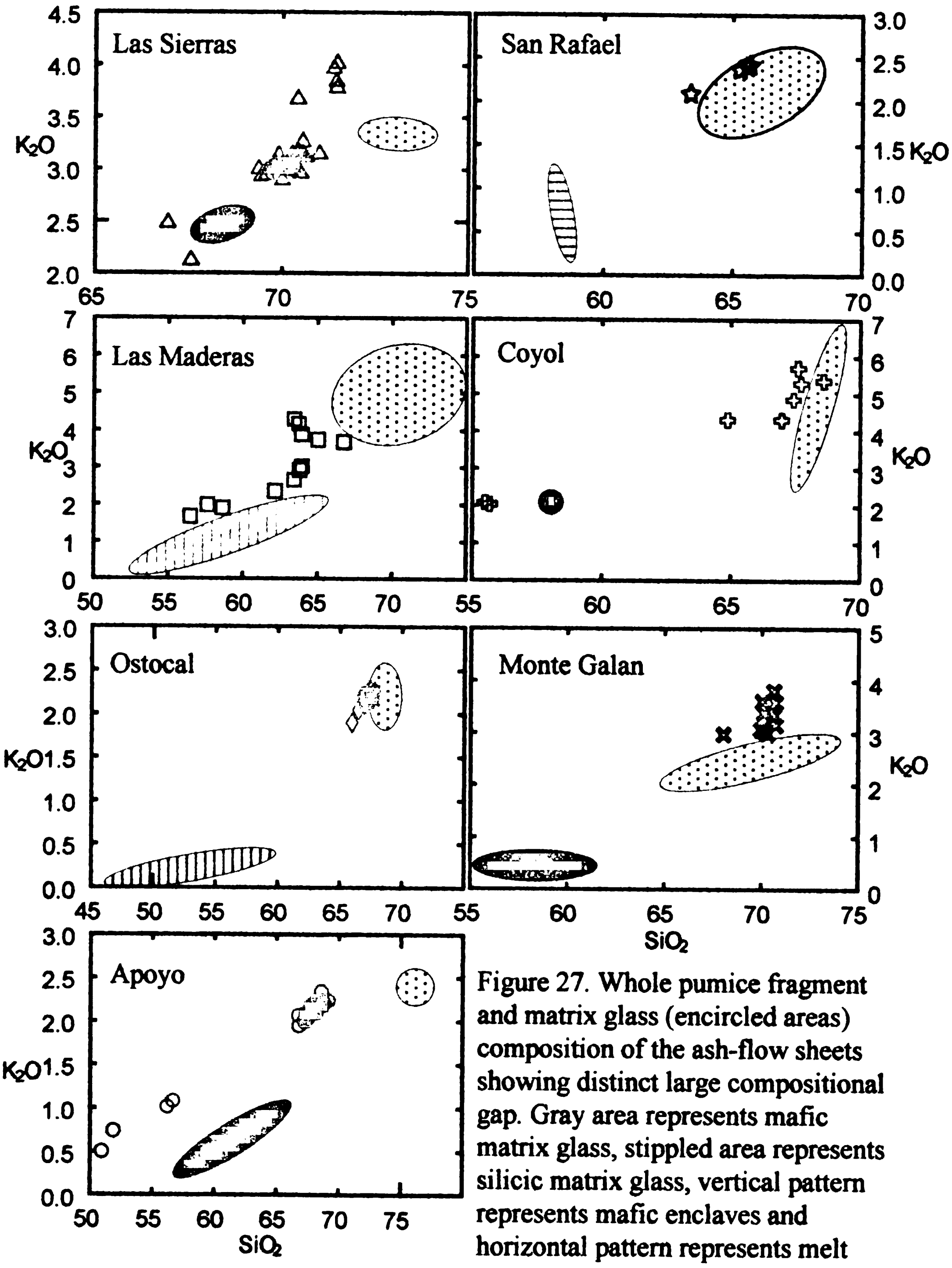

Figure 27. Whole pumice fragment and matrix glass (encircled areas) composition of the ash-flow sheets showing distinct large compositional gap. Gray area represents mafic matrix glass, stippled area represents silicic matrix glass, vertical pattern represents mafic enclaves and horizontal pattern represents melt inclusion in plagioclase.

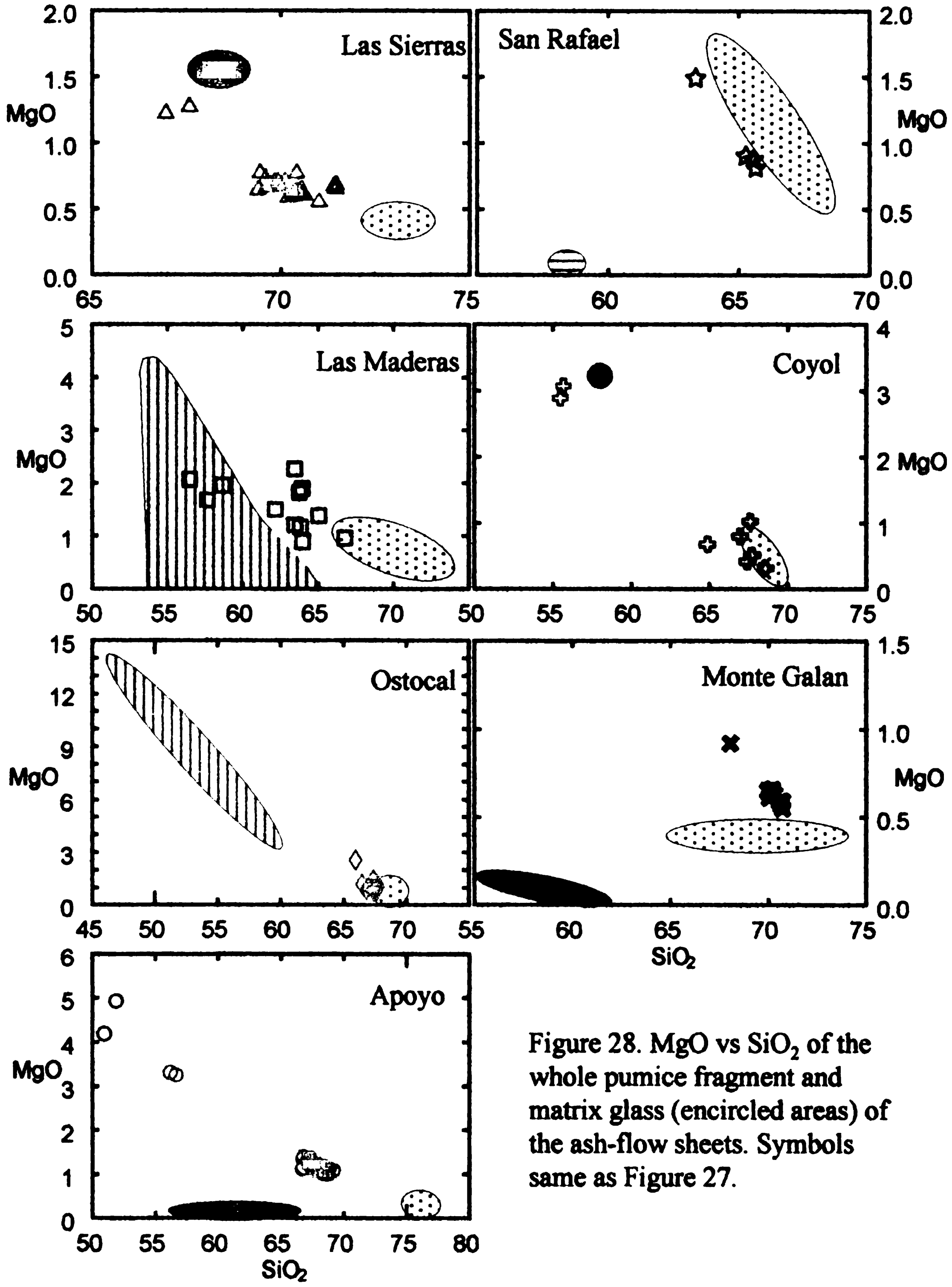

Figure 28. MgO vs SiO_2 of the whole pumice fragment and matrix glass (encircled areas) of the ash-flow sheets. Symbols same as Figure 27.

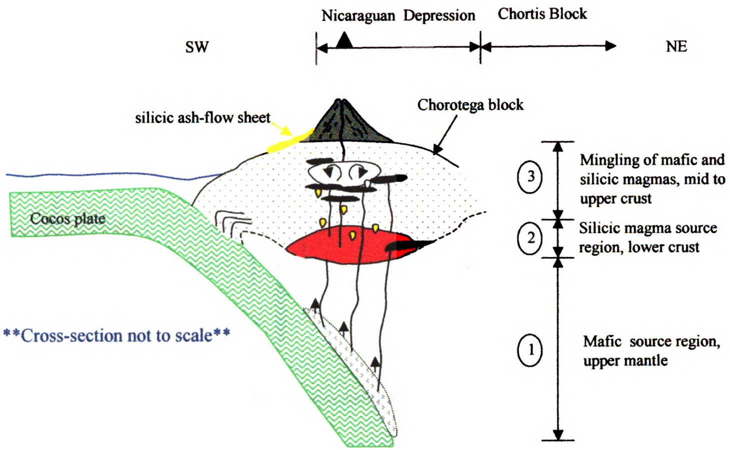

Figure 29. Model for the genesis of the silicic ash-flow sheets in Nicaragua. Cross-section is not to scale. See text for explanation.

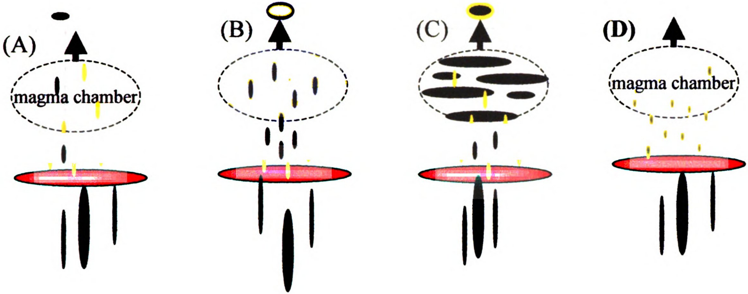

Figure 30. Cartoon depicting 4 possible scenarios during stage 3 in Figure 27. See text for explanation.

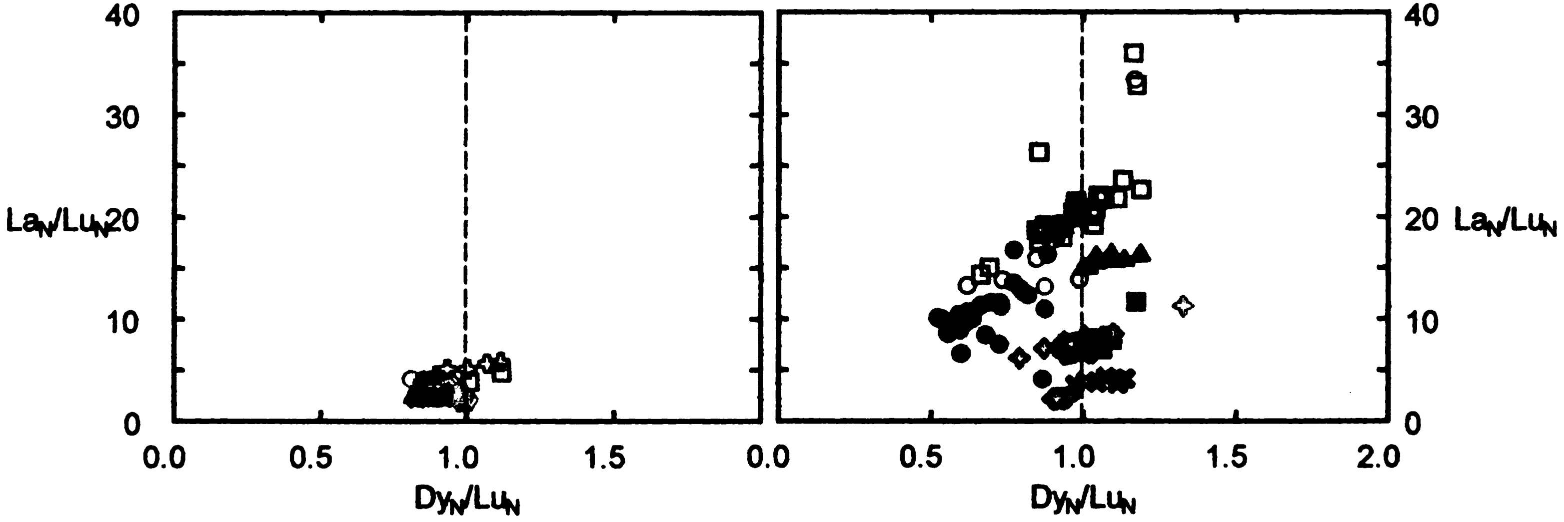

Figure 31. Dy_N/Lu_N vs La_N/Lu_N for Nicaraguan ash-flow sheets in comparison with some Costa Rican ash-flow sheets (SiO_2 >65 wt%). Costa Rican data from Hannah et al. (2000) and Szymanski et al. (2002).

REFERENCES

References

Alvarado, G.E., and Carr, M.J., 1993. The Platanar-Aquas Zarcas volcanic centers, Costa Rica: spatial-temporal association of Quaternary calc-alkaline and alkaline volcanism. Bull. Volcanol. 55: 443-453.

Anderson, A.T. Jr., 1984. Probable relations between plagiocalse zoning and magma dynamics, Fuego volcavo, Guatemala. Am. Mineral. 69: 660-676.

Andersen, D.J., Lindsley, D.H. and Davidson, P.M., 1993. QUILF: A pascal program to assess equilibria among Fe-Mg-Mn-Ti oxides, pyroxenes, olivine, and quartz. Computers and Geosci. 19: 1333-1350.

Annen, C. and Sparks, R.S.J., 2002. Effects of repetitive emplacement of basaltic intrusions on thermal evolution and melt generation in the crust. Earth Planet. Sci. Lett. 203: 937-955.

Bacon, C.R. and Druitt, T.H., 1988. Compositional evolution of the zoned calc-alkaline magma chamber of Mt. Mazama, Crater Lake, Oregon. Contrib. Mineral. Petrol. 98: 224-256.

Baker, B.H., and McBirney, A.R., 1985. Liquid fractionation Part III: geochemistry of zoned magmas and the compositional effects of liquid fractionation. J. Volcanol. Geotherm. Res. 24: 55-81.

Beard, J.S., and Lofgren, G.E., 1991. Dehydratioin melting and water-saturated melting of basaltic and andesitic greenstones and amphibolites at 1,3,and 6.9 kPa. J. Petrol. 32: 365-401.

Bergantz, G.W., 1989. Underplating and partial melting: implications for melt generation and extraction. Science 245: 1093-1095.

Bourgois, J., Azema, J., Baumgartner, P.O., Tournon, J., Desmet, A., Aubouin, J., 1984. The geologic history of the Caribbean-Cocos plate boundary with special reference to the Nicoya complex (Costa Rica) and DSDP results (Legs 67 and 84 off Guatemala): a synthesis. Tectonophys. 108: 1-32.

Brophy, J.G., Whittington, C.S., and Young-Rok, P., 1999. Sector-zoned augite megacrysts in Aleutian high alumina basalts: implications for the conditions of basalt crystallization and generation of calc-alkaline series magmas. Contrib. Min. Petrol. 135: 277-290.

Burbach, G.V., Frohlich, C., Pennington, W.D., Matumoto, T., 1984. Seismicity and tectonics of the subducted Cocos plate. J. Geophys. Res. 89: 7719-7735.

Carr, M.J., Feigebson, M.D., Benett, E.A., 1990. Incompatible element and isotopic evidences for tectonic control of source mixing and melt extraction along the Central American arc. Contrib. Mineral. Petrol. 105 (4): 369-380.

Cigolini, C., and Chaves, R., 1986. Geological, petrological and metallogenic characteristics of the Costa Rican gold belt: contribution to new explorations. Geol. Rundsch. 75: 737-754.

Criss, J.W., 1980. Fundamental parameters calculations on a laboratory microcomputer, advances in X-ray analysis. 22223:93-97.

DeMets, G., Gordon, R.G., Argus, D.f., Stein, S., 1990. Current plate motions. Geophys. J. Int. 101: 425-478.

Dengo, G., 1969. Problems of tectonic relations between Central America and the Caribbean. Trans. Gulf Coast Assoc Geol. Soc., 29: 311-320.

Di Marco, G., Baumgartner, P.O., Channel, J.E.T., 1995. Late Cretaceous-Early Tertiary paleomagnetic data and a revised tectono-stratigraphic subdivision of Costa Rica and western Panama. Geol. Soc. Am. Spec. Publ. 295: 1-27.

de Silva, S.L., and Wolff, J.A.., 1995. Zoned magma chambers: the influence of magma chamber geometry on sidewall convective fractionation. J. Volcanol. Geotherm. Res. 65:111-118.

Ehrenborg, J., 1996. A New stratigraphy of the Tertiary volcanic rocks of the Nicaraguan Highland, GSA Bull. 108 (7): 830-842.

Eichelberger, J.C., 1978. Andesitic volcanism and crustal evolution. Nature, 275; p. 21-27.

Eichelberger, J.C., Chertkoff, D.G., Dreher, S.T., Nye, C.J., 2000. Magma collision: rethinking chemical zonation in silicic magmas. Geology 28: 603-606.

Eichelberger , J.C. and Izbekov, P.E., 2000. Eruption of andeisite triggered by dike injection: contrasting cases at Karymsky volcano, Kamchatka and Mount Katmai, Alaska. Philos Trans Roy Soc 358 (1770): 1465-1485.

Elming, S.A., Layer, P., Ubieta, K., 2001 . A paleomagnetic study and age determination of Tertiary rocks in Nicaragua, Central America. Geophys. J. Int. 147: 294-309.

Escalante, G., 1990. The geology of southern Central America and western Colombia, in Dengo, G., and Case, J.E., eds., The Caribbean region: Boulder, Colorado, Geological Society of America, The Geology of North America, v. H, 201-230.

Feely, T.C. and Davidson, M.A., 1994. Petrology of calc-alkaline lavas at Volcan Ollague and the origin of compositional diversity at central Andean stratovolcanoes. J. Petrol. 35: 1295-1340.

Ginibre, C., Worner, G., Kronz, A., 2002. Minor- and trace-element zoning in plagioclase: implications for magma chamber processes at Parinacota volcano, northern Chile. Contrib. Mineral. Petrol. 143 (3): 300-315

Grove, T.L., Donnelly-Nolan, J.M., Housh, T., 1997. Magmatic processes that generated the rhyolite of Glass Mountain, Medicine Lake volcano, N. California. Contrib. Mineral. Petrol. 127: 205- 223.

Halama, R., Waight, T., Markl, G., 2002. Geochemical and isotopic zoning patterns of plagioclase megacrysts in gabbroic dykes from the Gardar Province, South Greenland: implications for crystallisation processes in anorthositic magmas. Contrib. Mineral. Petrol.144(1): 109-127.

Hannah, R.S., 2002. Origin of the chemical variation in the Valle Central tuff,Costa Rica. M.Sc. Thesis, Michigan State University, East Lansing, MI.

Hauff, F., Hoernle, K., Schmincke, H.U., Werner, R., 1997. A mid-Cretaceous origin for the Galapagos hotspot: volcanological, petrological, and geochemical evidence from Costa Rican oceanic crustal segments. Geol. Rundsch. 84: 141-155.

Hauff, F., Hoernle, K., van den Bogaard, P., Alvarado, G., Garbe-Schonberg, D., 2000. Age and geochemistry of basaltic complexes in western Costa Rica: contributions to the geotectonic evolution of Central America. Geochem. Geophys. Geosys. 1, paper number 1999GC000020.

Hildreth, W., and Fierstein, J., 2000. Katmai volcanic cluster and the great eruption of 1912. Geol. Soc. Am. Bull. 112 (10): 1594-1620.

Kerr, A.C., Tarney, J., Marriner, G.F., Nivia, A., Saunders, A.D., 1997. The Caribbean-Colombia Cretaceous Igneous Province: the internal anatomy of an oceanic plateau. In Mahoney, J.J., and Millard, C.F., eds. Large Igneous Provinces: Continental, Oceanic, and Planetary Flood Volcanism. Geophysical Monograph 100, 123-144.

Kuritani, T., 1998. Boundary layer crystallization in a basaltic magma chamber: evidence from Rishiri volcano, northern Japan. J. Petrol. 39: 1619-1640.

Kuritani, T., 2001. Replenishment of a mafic magma in a zoned felsic magma chamber beneath Rishiri volcano, Japan. Bull. Volc. 62: 533-548.

Lyle, M., Dadey, K.A., Farell, J.W., 1995. The Late Miocene (11-8Ma) eastern Pacific carbonate crash: evidence for reorganization of deep-water circulation by the closure of the Panama gateway. In Pisias, N.G., Mayer, L.A.: Proceedings of the Ocean Drilling Program, Scientific results, Vol. 138: College Station, Texas, Ocean Drilling Program, p. 821-838.

Marsh, B.D., 1984. Mechanics and energetics of magma formation and ascent. In Boyd. F.R. (ed.) Studies in geophysics, explosive volcanism: inception, evolution and hazards. National Academy Press, Washington D.C., pp. 67-83.

McBirney, A.R. and Williams, H., 1965. Volcanic history of Nicaragua. Univ. California Publ. Geol. Sci. 55:1-65.

McBirney, A.R., 1980. Mixing and unmixing in magmas. K. Volcanol. Geotherm. Res. 7: 357-371.

McBirney, A.R., and Nielson,R.H., 1986. Reply to "Liquid collection in sidewall crystallization of magma: a comment on 'liquid fractionation' by Morse, S.A. J. Volcanol. Geotherm. Res. 30: 163-168.

McBirney, A.R., Taylor, H.P., Armstrong, R.L., 1987. Paricutin re-examined: a classic example of crustal assimilation in calc-alkaline magma. Contrib. Mineral. Petrol. 95: 4-20.

Meschede, M., and Frisch, W., 1998. A plate-tectonic model for the Mesozoic and Early Cenozoic history of the Caribbean Plate. Tectonics 296: 269-291.

Mittlefehltd, D., and Miller, C.F., 1983. Geochemistry of the Sweetwater Wash pltuton, California: implications for "anomalous" trace element behavior during differentiation of felsic magmas. Geochem. Cosmochim. Acta 47: 109-124.

Morris, J.D., Leeman, W.P., Tera, F., 1990. The subducted component in island arc lavas: constraints from Be isotopes and B-Be systematics. Nature 344: 31-36.

Nakagawa, M., Wada, K., Thordarson, T., 1999. Petrologic investigations of the 1995 and 1996 eruptions of Ruapehu volcano, New Zealand: formation of discrete and small magma pockets and their intermittent discharge. Bull. Volcanol. 61 (1-2): 15-31.

Nakajima, K. and Arima, M., 1998. Melting experiments on hydrous low-K tholeiite: Implications for the genesis of tonalitic crust in the Izu-Bonin-Mariana arc. Island Arc 7 (3): 359-373.

Nystrom, J.O., Levi, B., Skiold, T., Fallick, A.E., Darce, M., 1993. Cenozoic volcanism within the Nicaraguan geotraverse. Rev. Geol. Amer. Central 16: 107-111.

Pallister, J.S., Hoblitt, R.P., Meeker, G.P., Knight, R.J., and Siems, D.F., 1992. Magma mixing at Mount Pinatubo: petrographic and chemical evidence from the 1991 deposits. In Newhall, C.G., and Punongbayan, R.S., eds. Fire and Mud: Eruptions and lahars of Mount Pinatubo, Philippines. Seattle: Univ. of Washington Press, 687-731.

Patino, L.C., Carr, M.J., Feigenson, M.D., 2000. Local and regional variations in Central American arc lavas controlled by variations in subducted sediment input. Contrib. Mineral. Petrol. 138: 265-283.

Petford, N. and Gallagher, K., 2001. Partial melting of mafic (amphibolitic) lower crust by periodic influx of basaltic magma. Earth Planet. Sci. Lett. 193: 483-499.

Pindell, J.L. and Barrett, S.F., 1990. Geological evolution of the Caribbean region: a plate-tectonic perspective, in Dengo, G., and Case, J.E., eds., The Caribbean region: Boulder, Colorado, Geological Society of America, The Geology of North America, v. H, 405-432.

Plank, T., Balzer, V., Carr, M., 2002. Nicaraguan volcanoes record paleoceanographic changes accompanying closure of the Panaman gateway. Geology 30 (12): 1087-1090.

Rapp, R.P. Watson, E.B., Miller, C.F., 1991. Partial melting of amphibolite/eclogite and the origin of Archaean trondhjemites and tonalities. Precambrian Res. 51: 1-25.

Rapp, R.P. and Watson, E.B., 1995. Dehydration melting of metabasalt at 8-32 kbar: implications for continental growth and crust-mantle recycling. J. Petrol. 36: 891-931.

Roberts, M.P., and Clemens, J.D., 1993. Origin of high-potassium calc-alkaline, I-type granitoids. Geology 21: 825-828.

Rogers, R.D., Karason, H. van der Hilst. R.D., 2002. Epeirogenic uplift above a detached slab in northern Central America. Geol. 30: 1031-1034.

Sawyer, E.W.,1994. Melt segregation in the continental crust. Geology 22:1019-1022.

Sen, C. and Dunn, T., 1994. Dehydration melting of a basaltic composition amphibolite at 1.5 and 2.0 GPa: implications for the origin of adakites. Contrib. Mineral. Petrol. 117: 394-409.

Sigurdsson, H., Kelly, S., Leckie, R.M., Carey, S. N., Browning, J.M., Rogers, R.D., 2000. History of Circum-Caribbean explosive volcanism: Ar/Ar dating of tephra layers. In Leckie, R.M., Sigurdsson, H., Acton, G.D., Draper, G., eds., Proceeding of the Ocean Drilling Program, Scientific Results, v. 165: 299-314.

Sinton, C.W., Duncan, R.A. Denyer, P., 1997. Nicoya Peninsula, Costa Rica: a single suite of Caribbean oceanic plateau magmas. J. Geophys. Res. 102 (B7): 15,507-15,520.

Sisson, T.W., and Grove, T.L. 1993. Experimental investigations of the role of H_2O in calc-alkaline differentiation and subduction zone magmatism. Contrib. Mineral. Petrol. 34: 143-166.

Smith, I.E.M., Stewart, R.B., Price, R.C., 2003. The petrology of a large intra-oceanic silicic eruption: the Sandy Bay Tephra, Kermadec Arc, Southwest Pacific. J. Volc. Geotherm. Res. 124: 173-194.

Sparks, R.S.J., Sigurdsson, H., and Wilson, L., 1977. Magma mixing; a mechanism for triggering acid explosive eruptions. Nature, 267; p. 315-318.

Stimac, J.A., Pearce, T.H., Donnnelly-Nolan, J.M., and Hearn, B.C., 1990. The origin and implication of undercooled andesitic inclusions in rhyolites, Clear Lake, California. J. Geophy. Res., 95; p. 17,729-17,746.

Sun, S. and McDonough, W.F., 1989. Chemical and isotopic systematics of oceanic basalts: implications for mantle composition and processes. In Saunders, A.D., Norry, M.J. (eds.) Magmatism in the ocean basins. Geol. Soc. Spec. Publ. 42: 313-345.s

Sussman, D., 1985. Apoyo caldera, Nicaragua: a major Quaternary silicic eruptive center. J. Volc. Geotherm. Res. 24: 249-282.

Snyder, D. and Tait, S., 1998. The imprint of basalt on the geochemistry of silicic magmas. Earth Planet. Sci. Lett. 160: 433-445.

Szymanski, D.W., Patino, L.C., Vogel, T.A., Alvarado, G.E., 2002. Generation of Continental Crust in Central America: New Field and Geochemical Observations on Silicic Magmatism in Costa Rica. *Eos Trans. AGU, 83*(47), Fall Meet. Suppl., Abstract V12C-09.

Tamura, Y. and Tatsumi, Y., 2002. Remelting of an andesitic crust as a possible origin for rhyolite magma in oceanic arcs: an example from the Izu-Bonin arc. J. Petrol. 43: 1029-1047.

Tatsumi, Y., 1986. Formation of the volcanic front in subduction zones. Geophys. Res. Lett. 13 (8): 717-720.

Turner, J.S., and Gustafson, L.B., 1981. Fluid motions and compositional gradients produced by crystallization or melting at vertical boundaries. J. Volcanol. Geotherm. Res.11: 93-125.

Van Wyk de Vries, B., 1993. tectonics and magma evolution of Nicaraguan volcanic systems. Unpublished Ph.D. thesis, Department of Earth Sciences, The Open University, U.K., 328 pp.

Walther, C., Flueh, E.,Ranero, C, von Huene, R., Strauch, W., 2000. Crustal structure across the PAcific margin of Nicaragua: evidence for ophiolitic basement and a shallow mantle sliver. Geophysic Journal International 141: 759-777

Weinberg, R.F., 1992. Neotectonic development of western Nicaragua. Tectonics 11: 1010-1017.

Wilson, D.S., 1996. Fastest known spreading on the Miocene Cocos-Pacific plate boundary. Geophys. Res. Lett. 23: 3003-3006.

Wolf, M.B. and Wyllie, P.J., 1994. Dehydration melting of amphibolite at 10 kbar: the effects of temperature and time. Contrib. Mineral. Petrol. 115: 360-383.